Constraining the Jet Properties of the New Transient X-ray Binary, Swift J1745–26, With the Submillimeter Array and James Clerk Maxwell Telescope

by

Alexandra Jean Tetarenko

A thesis submitted in partial fulfillment of the requirements for the degree of

Master of Science

Department of Physics
University of Alberta

Abstract

Accreting astrophysical sources are an important end-result of intricate stellar dynamics. A particularly puzzling aspect of this accretion process is the production and evolution of plasma outflows (known as jets). Although astrophysical jets have been studied for decades in accreting sources, the underlying physics that governs jet behaviour is still poorly understood. Since black hole X-ray binary (BHXRB) systems evolve on short timescales, the steady, compact relativistic plasma jet that is present at the onset of a BHXRB outburst serves as an important probe of jet physics and analogue for the universal process of jet production in other astrophysical systems. The detailed properties of BHXRB jets are encoded in the broadband spectral energy distribution (SED). However, we could only recently begin to fill in a large void in our broadband coverage, the mm/sub-mm regime.

In this thesis, I discuss the results obtained from our observing campaign of the 2012 outburst of the new transient BHXRB, Swift J1745–26. These observations represent the first ever simultaneous radio and multiple-band mm/sub-mm observations of a BHXRB. The instruments used to obtain the data were the Karl G. Jansky Very Large Array (VLA), the Submillimeter Array (SMA) and the Submillimetre Common User Bolometer Array 2 detector on the James

Clerk Maxwell Telescope (SCUBA-2 on the JCMT). With the combination of radio and mm/sub-mm data, I am able to directly measure the spectral indices in and between the radio and mm/sub-mm regimes as well as probe a relatively untested part of the jet spectrum (mm/sub-mm regime).

I present these spectral measurements to determine whether the jet emission in the mm/sub-mm regime is consistent with typical jet models, where a single power-law can accurately describe the radio through sub-mm SED, as well as to constrain the origin of high mm/sub-mm fluxes that have been observed in the few BHXRBs in outburst. The spectral fitting process revealed that both the mm (230 GHz) and sub-mm (350 GHz) measurements are consistent with extrapolations from contemporaneous radio data (1–30 GHz) of a slightly inverted spectra (i.e., I measure higher flux density at higher frequencies). This indicates that even at higher mm/sub-mm frequencies a power-law can sufficiently describe the spectrum. Moreover, this suggests that the mechanism driving spectral inversion could be the same mechanism driving high mm/sub-mm fluxes in outbursting BHXRBs, rather then anomalous excess emission. Finally, I consider the effects of complex spectral features and flux variability at radio frequencies on our interpretation of the jet spectrum.

Our analysis solidifies the importance of the mm/sub-mm regime in bridging the crucial gap between radio and IR frequencies in the jet spectrum, demonstrates the capacity of current mm/sub-mm instruments to address questions in this regime, and justifies the need to explore this regime in multiple sources.

Preface

This thesis is original work by Alexandra Tetarenko. The author was not involved in the acquisition of the data analyzed in this thesis. While the radio frequency data obtained from the Karl G. Jansky Very Large Array (VLA) was reduced by James Miller-Jones and Peter Curran, the author reduced the mm/sub-mm data obtained from the Submillimeter Array (SMA) and James Clerk Maxwell Telescope (JCMT). Some of the radio frequency data obtained with the VLA that is analyzed in this thesis has been published in P.A. Curran et al., "The Evolving Polarized Jet of Black Hole Candidate Swift J1745–26", *MNRAS*, 437:3265-3273, 2014.

"The worthwhile problems are the ones you can really solve or help solve, the ones you can really contribute something to. ... No problem is too small or too trivial if we can really do something about it."

Richard P. Feynman

Acknowledgements

I would like to express a sincere thank you to my supervisor, Greg Sivakoff, for introducing me to this field, answering my many questions, giving me the opportunity to lead several proposals and subsequently trusting me with them, and most of all putting up with my very frequent visits to his office. Additionally, I would like to thank James Miller-Jones and Peter Curran for helping me reduce the complicated data analyzed in this thesis. Special thanks goes out to Thomas Russell, with which several discussions led me to a much deeper understanding of the reduction process for radio and mm/sub-mm data. I would also like to thank my family for supporting me in everything I do. In particular, my Mom who has edited everything I have written since middle school and continues to be my first line of defence against the horribly difficult rules of proper grammar and spelling; my Dad, whose many questions about astronomy often lead me to think about my research problems in a new light; and my Sister, who is my walking, talking Python dictionary. Finally, I would like to thank Ben and Sofie, for never failing to remind me that I am not a robot and do need to take a break from working ever so often.

Contents

List of Tables

List of Figures

List of Abbreviations

ADAF	Advection Dominated Accretion Flow
ADIOS	Advection Dominated Inflow Outflow Solution
AGN	Active Galactic Nuclei
ALMA	Atacama Large Millimetre Array
BAT	Burst Alert Telescope
BH	Black Hole
BHXRB	Black Hole X-ray Binary
GRB	Gamma Ray Burst
CARMA	Combined Array for Research in Millimetre Astronomy
CASA	Common Astronomy Software Application
CDAF	Convection Dominated Accretion Flow
DIMM	Dynamic Iterative Map Maker
FCF	Flux Conversion Factor
GHz	GigaHertz
HID	Hardness Intensity Diagram
HS	Hard (Comptonized) State
IF	Intermediate Frequency
ISM	InterStellar Medium
ISCO	Innermost Stable Circular Orbit
JCMT	James Clerk Maxwell Telescope
JDAF	Jet Dominated Accretion Flow
LHAF	Luminous Hot Accretion Flow
LO	Local Oscillator
MDAF	Magnetically Dominated Accretion Flow

MERLIN	Multi-Element Radio Linked Interferometer Network
MHD	MagnetoHydroDynamics
mJy	milli-Jansky
MRI	Magneto-Rotational Instability
PdBI	Plateau de Bure Interferometer
PWV	Precipitable Water Vapor
RF	Radio Frequency
RIAF	Radiatively Inefficient Accretion Flow
SCUBA-2	Submillimetre Common User Bolometer Array 2
SED	Spectral Energy Distribution
SMA	SubMillimeter Array
SPL	Steep Power-Law
SQUID	Superconducting QuantUm Interference Device
SS	Soft (Disc Dominated) State
TES	Transition Edge Sensor
VLA	(Karl G. Jansky) Very Large Array
VLBA	Very Long Baseline Array
VLBI	Very Long Baseline Interferometry
WVM	Water Vapor Monitor
XRB	X-ray Binary

Chapter 1

Relativistic Outflows in Accreting Astrophysical Systems

1.1 Introduction to Relativistic Jets

Relativistic jets are powerful, collimated, plasma outflows of energy, angular momentum and matter (Fender and Belloni, 2004). While these jets have been studied for decades in accreting sources, the underlying physics that governs jet behaviour is still poorly understood. Despite the many unknowns in jet physics, it is clear that these jets play a crucial role in the accretion process as there is ample observational evidence linking inflow and outflow in accreting systems (Fender et al., 2004; Merloni et al., 2003; Falcke et al., 2004; Corbel et al., 2013), as well as evidence suggesting that jets can transport a considerable portion of accretion power and angular momentum, resulting in the deposit of large amounts of energy and matter into the surrounding medium (Fender, 2006; Gallo et al., 2005). Relativistic jets have been identified in many different astrophysical systems spanning a wide range of size and mass scales, including Active Galactic Nuclei (AGN), Gamma-Ray Bursts (GRBs), and Black Hole X-Ray Binaries (BHXRBs) in our own Galaxy (Mirabel and Rodriguez, 1999). Among these sources, BHXRB systems are ideal probes for jet phenomenon

because they vary on short timescales (days to months), as opposed to AGN where entire outbursts evolve on million year timescales. Therefore, BHXRBs are very accessible to observers as many different phases of jet behaviour (jet onset, fading, and quenching) can be studied through observations of a single system.

1.1.1 Black Hole X-ray Binaries (BHXRBs)

BHXRBs are binary systems that contain an accreting stellar mass black hole (BH) paired with a companion star (see Figure 1.1). In these systems, material is pulled off the companion star towards the BH forming a differentially rotating disc (called an accretion disc). Additionally, a portion of this material can be transported back outwards in the form of a relativistic plasma jet (Remillard and McClintock, 2006).

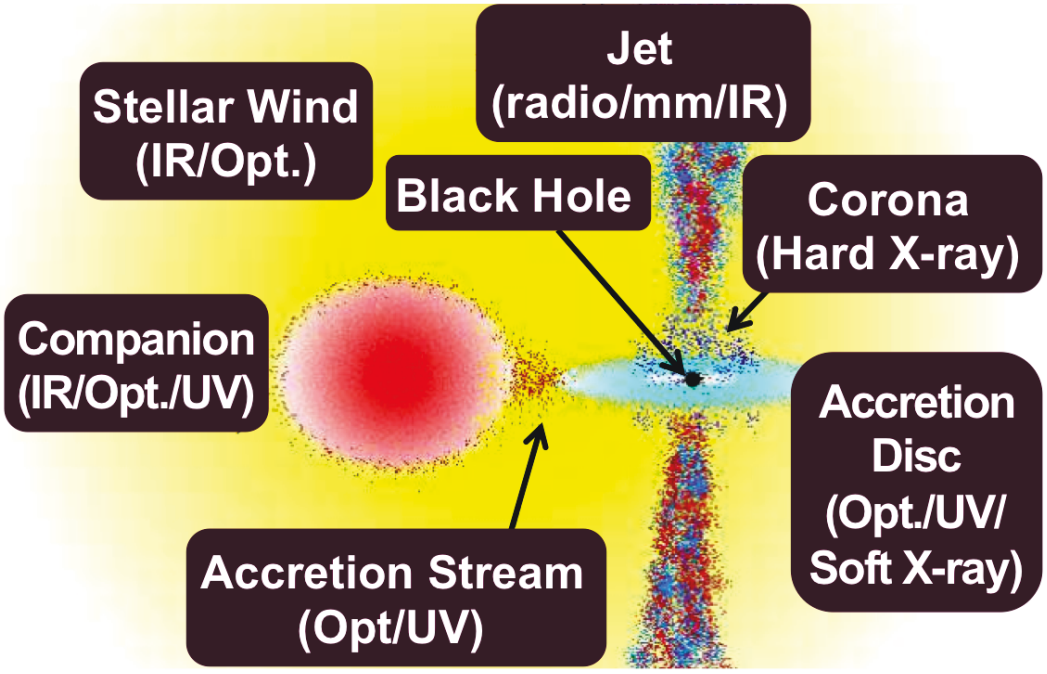

Figure 1.1: A schematic of the emission regions in a BHXRB. Many different sources of emission from across the electromagnetic spectrum are present. In particular, the jets emit at radio through IR frequencies. Figure is adapted from Fender (1999).

Typically BHXRB systems are present in one of two basic states:

- Quiescence: a period of relative inactivity (i.e., a low rate of mass accretion) lasting months to decades with X-ray luminosities of $10^{30} - 10^{33}\,\mathrm{erg\,s^{-1}}$ (McClintock and Remillard, 2006);

- Outburst: a period characterized by rapid increases in X-ray luminosity (where some sources can reach as high as the Eddington limit[1], $\sim 10^{39}\,\mathrm{erg\,s^{-1}}$; Tanaka and Lewin 1995), and the launching of a compact, steady, relativistic jet (Fender, 2003; Fender et al., 2004, 2009). The latter is signalled by the detection of a radio counterpart.

To probe the jet properties accurately, we sample these systems in the outburst phase as the contrast between emission from the jets and other system components (accretion disc and companion) is greatest during this phase for frequencies below those of X-rays (Fender and Belloni, 2012). In addition, during the outburst phase the jet emission becomes brighter than the detection limits of our current radio and mm/sub-mm instrumentation.

Two types of relativistic jets are observed during BHXRB outbursts (Fender et al., 2009, 2004):

- Steady Jet[2] – persistent, collimated, continuously replenished outflow of optically thick plasma (e.g., see Figure 1.2 and Figure 1.3);

- Transient Jet – discrete, highly relativistic ejections of optically thin plasma (e.g., see Figure 1.4).

The radio through IR emission from these jets produces a non-thermal spectrum thought to be the result of synchrotron radiation, due to the presence

[1]The Eddington limit is the luminosity, assuming pure hydrogen accretion and spherical symmetry, where the outwards radiation force (on the electrons) balances the inwards gravitational force (on the protons). The Eddington luminosity scales linearly with mass, $L_E = \frac{4\pi G M m_p c}{\sigma_T} \cong 1.3 \times 10^{38} \frac{M}{M_\odot}\,\mathrm{erg\,s^{-1}}$ (Frank et al., 2002).

[2]In this thesis I will only be focusing on these steady type jets.

of highly relativistic electrons[3] and magnetic fields in these systems (Fender, 2006). Detailed properties of these BHXRB jets are encoded within this spectrum, also known as a spectral energy distribution (SED). Therefore, analyzing the SED in BHXRBs can reveal insights into important jet properties such as jet power, plasma dynamics, particle content, energy conversion and efficiency, geometry, magnetic field strength, and radiation processes in the jet (Heinz and Sunyaev, 2003; Markoff et al., 2005; Pe'er and Casella, 2009; Casella and Pe'er, 2009; Heinz and Grimm, 2005; Markoff et al., 2003). Additionally, studying the jets in BHXRBs can probe the universal process of jet formation and could ultimately help constrain the physics of these ubiquitous objects in other astrophysical systems, most notably in AGN, where jet feedback is thought to play a key role in galaxy formation and evolution (Fabian, 2012).

[3]The full composition of these plasma jets is still highly uncertain. While it is clear the jets contain electrons, it is unclear whether they are paired with positrons or protons, or whether the jet content evolves over time. Although, there has been recent evidence of relativistically doppler shifted X-ray emission lines that suggest baryonic content in the jets of the BHXRB source, 4U 1630–47 (Diaz Trigo et al., 2013).

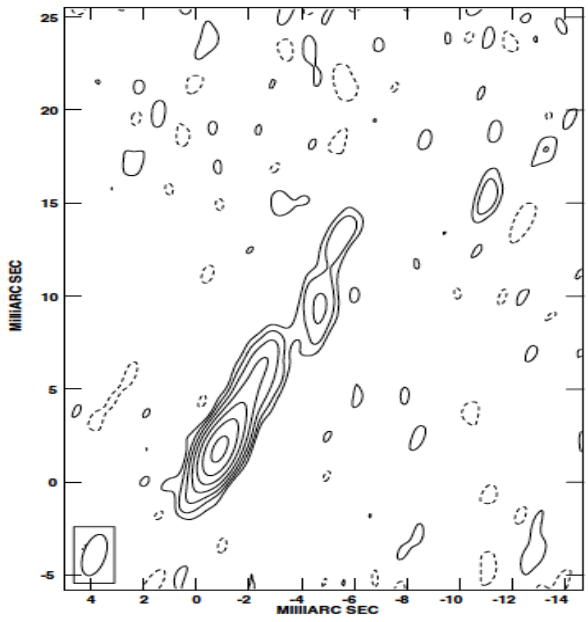

Figure 1.2: Radio emission of a one sided relativistic jet in Cyg X–1 observed with the Very Long Baseline Array (VLBA). This image displays AU-scale jets and is a typical example of steady jets in a Galactic BHXRB source (Stirling et al., 2001). Note that one-sided jets are due to Doppler boosting (and de-boosting) of the side of the relativistic jet pointing towards (away) from the Earth (see Section 1.2.2 for more details).

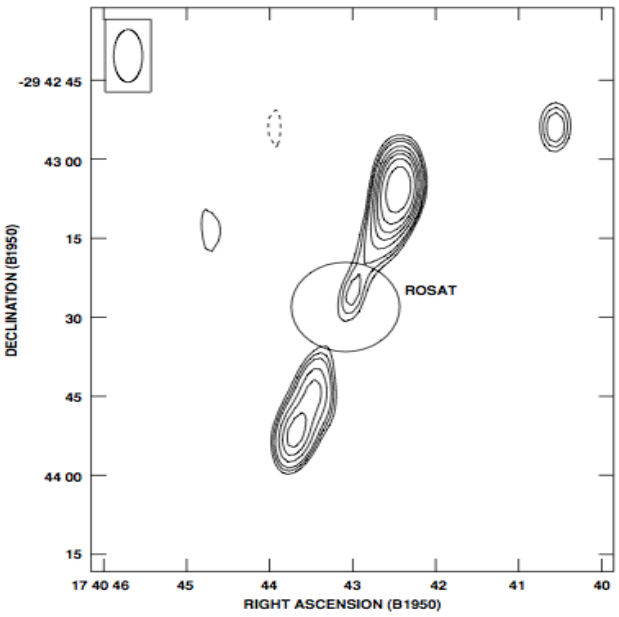

Figure 1.3: Radio emission from 1E 1740.7–2942 observed with the Karl G. Jansky Very Large Array (VLA). This image displays arcminute-scale jets, where the clear radio lobes are interpreted as the result of the interaction of steady jets with the surrounding ISM over long timescales (Mirabel et al., 1992).

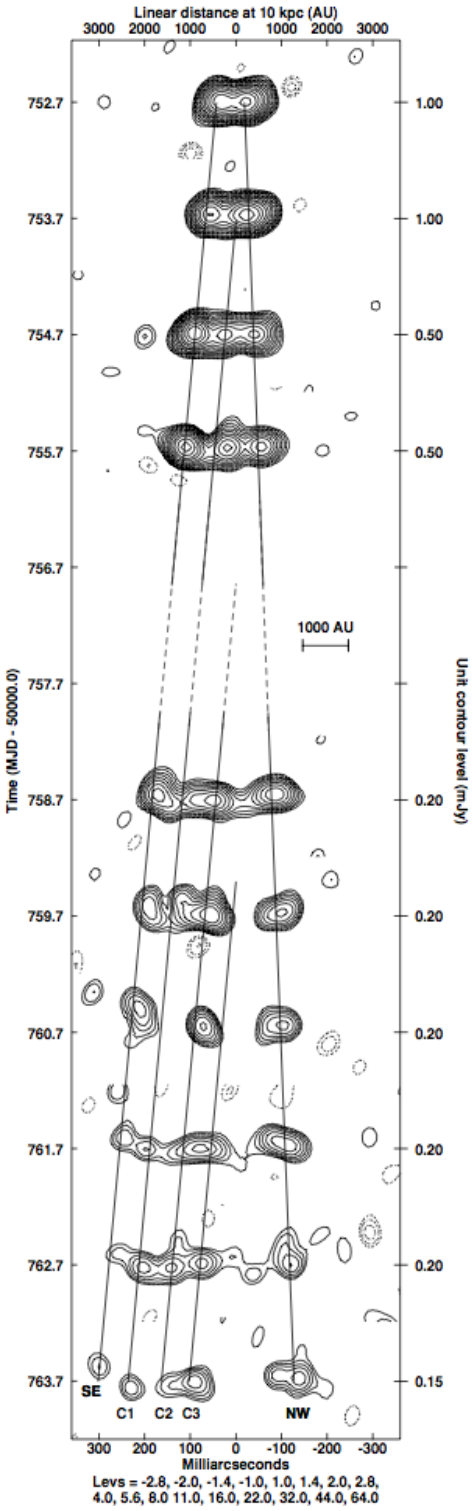

Figure 1.4: Radio emission of relativistic jets in GRS 1915+105 observed with Multi-Element Radio Linked Interferometer Network (MERLIN). This image displays superluminal relativistic ejections and is a typical example of transient jets in a Galactic BHXRB source (Fender et al., 1999).

1.2 Observational Picture

1.2.1 BHXRB Accretion States

In recent years significant advances in astronomical instrumentation, most notably in the radio and X-ray regimes, has enabled multi-wavelength monitoring of Galactic BHXRB systems. Such observing campaigns have allowed astronomers to probe BHXRB outburst behaviour like never before. These studies revealed an overall canonical outburst pattern that seems to be universally followed across many systems, as well as a clear correlation between the X-ray and radio regimes, linking inflow (accretion) and outflow (jets). In this outburst pattern, BHXRBs undergo hysteresis moving through several different accretion states as they evolve from quiescence into outburst and back again. These states are typically characterized by various spectral and variability properties (Done et al., 2007). Below I will outline this canonical model, describing each of the accretion states by first presenting the physical picture (morphology of jet and nature of accretion flow) of the system, and then describing the accompanying spectrum and its individual components. The terminology for the accretion states in an outbursting BHXRB can vary quite significantly in the literature, but I will adhere to the nomenclature in Table 1.1

Table 1.1: Nomenclature for BHXRB Accretion States

State	**Abbreviation**
Hard (Comptonized) State	HS
Soft (Disc Dominated) State	SS
Steep Power-Law State	SPL

The evolution of an BHXRB through these accretion states can be summarized on a hardness-intensity diagram (HID, Figure 1.5) which plots X-ray intensity (luminosity) vs. X-ray hardness (ratio of high energy to low energy X-ray emission) (McClintock and Remillard, 2006).

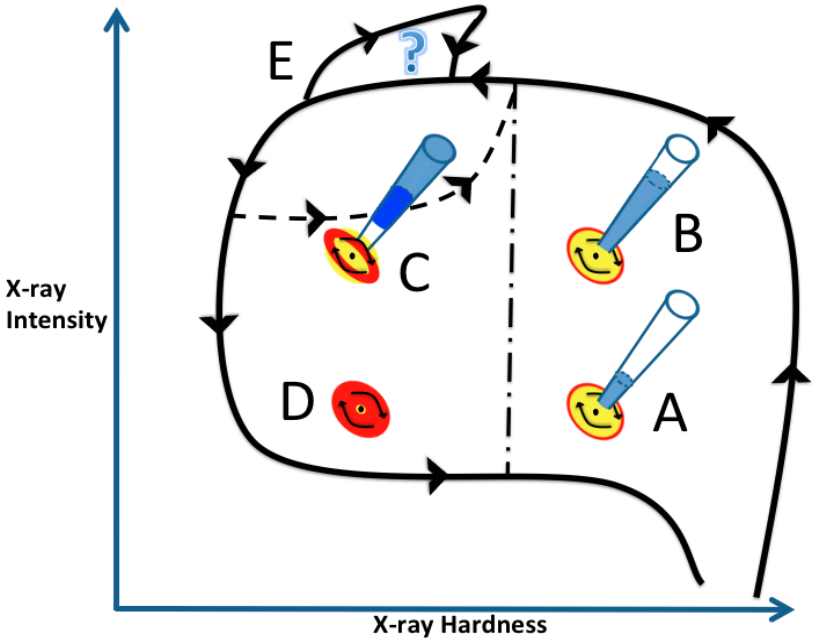

Figure 1.5: HID for an ideal BHXRB system. The arrows indicate the typical direction of evolution. The dot-dashed line represents the Jet Line with the HS (A and B) to the right and the SS (C and D) to the left. The SPL state is located at the top (labelled E), in which system morphology is highly uncertain. Letters represent stages with different jet morphology. Yellow indicates the Comptonizing corona, red indicates the accretion disc, and blue indicates the jet. Please see the text for a full description of each state and their transitions. Figure adapted from Fender et al. (2004).

Hard (Comptonized) State: The HS is associated with the early & very late stages of an outburst and can be seen to the right of the dot dashed line (A and B) on the HID in Figure 1.5. This state typically occurs at a lower X-ray intensity, corresponding to lower mass accretion rates and lower fractions of Eddington. The physical picture in this state consists of a truncated cool, geometrically thin, optically thick accretion disc situated far from the BH ($\sim 10 - 100R_s$)[4], a geometrically thick, optically thin, hot inner flow (i.e., a corona[5]), and a compact, steady, relativistic plasma jet. The bottom panel in Figure 1.6 displays the complete morphology of the system in this state, and an example of a broadband HS spectrum from the BHXRB source MAXI J1836–194 can be seen in Figure 1.7.

The jet emits primarily at radio through IR frequencies, with the emission being the result of synchrotron radiation from a power-law distribution of electrons. The jet spectrum consists of a flat to slightly inverted optically thick piece ($\alpha \geq 0$; where flux density, $f_\nu \propto \nu^\alpha$) extending from radio through sub-mm frequencies (possibly even up to IR frequencies). Nearer to infrared frequencies, the jet emission produces a steep optically thin spectrum ($\alpha < 0$, depending on the electron energy distribution), leading to a rapidly declining flux density with increasing frequency. This suggests that somewhere in between these optically thick and thin regions, a spectral break must occur; its location is predicted (and also has been observed both directly and indirectly[6]) to be in the sub-mm to mid-infrared regime (Russell et al., 2012; Fender and Belloni, 2004; Fender et al., 2004; Fender, 2003, 2006; Fender et al., 2009).

The corona and accretion disc primarily emit at X-ray frequencies. The

[4] R_s indicates the Schwarzschild radii, $R_s \sim \frac{2GM}{c^2}$; G is the gravitational constant, M is BH mass and c the speed of light.

[5] The structure of this flow is still an open question. However, there are models that consider this flow as an extension of the accretion disc flow that has become optically thin. See Sections 1.3.1 and 1.3.3 for more details.

[6] Observing the spectral break indirectly refers to estimating the spectral break location through interpolation as opposed to directly observing the spectral break within the data.

X-ray spectrum is dominated by a hard, non-thermal power-law tail ($\Gamma \sim 1.5-1.7$; where energy flux, $f_\epsilon \propto \epsilon^{-(\Gamma-1)}$)[7] with a high-energy cutoff at $\sim 100\,\mathrm{keV}$, which is typically thought to be produced by thermal Comptonization of soft seed photons from the disc[8]. A weak, cool, thermal disc component peaking at $\sim 0.1\,\mathrm{keV}$ is also present from blackbody emission (Homan and Belloni, 2005; McClintock and Remillard, 2006; Belloni, 2009; Zdziarski and Gierlinski, 2004; Done et al., 2007).

In this state, the BHXRB system exhibits a well known correlation between radio and X-ray luminosities (i.e., between jet power and accretion power) according to $L_R \propto L_X^{0.7}$ (Gallo et al., 2003; Corbel et al., 2003). This state probably extends down to quiescence (very low X-ray luminosities)[9].

Soft (Disc Dominated) State: The SS can be seen to the left of the dot dashed line (C and D) on the HID in Figure 1.5. This state typically occurs at a higher X-ray intensity, corresponding to higher mass accretion rates and higher fractions of Eddington. The physical picture in this state consists of a hot, geometrically thin, optically thick accretion disc extending up to the innermost stable circular orbit (ISCO; $r = 3R_s$ for a Schwarzschild BH) and a very optically thin inner flow that could be located over the disc or in localized

[7] Γ and ϵ represent the photon index and energy band respectively. The power law spectra can be written in terms of the differential photon number density (photons per second per square cm per energy band), $N(\epsilon) \propto \epsilon^{-\Gamma}$ or energy flux, $f_\epsilon = \epsilon N(\epsilon) \propto \epsilon^{-(\Gamma-1)}$.

[8] Note that there are a few alternative theories that predict the hard power-law originates at the base of the jet. The hard power-law could be an extension of the optically thin power-law from the synchrotron emission of non-thermal electrons at the base of the jet (Markoff et al., 2001). On the other hand it could also be the result of thermal Comptonization by electrons at the base of the jet, while the radio emission still originates from non-thermal electrons accelerated up the jet (Markoff et al., 2005). Further, Russell et al. (2010) found evidence for jet synchrotron emission dominating the X-ray flux in the BHXRB XTE J1550–564.

[9] There is both observational and theoretical evidence to support that the HS extends into quiescence. The L_R/L_X relation has been observed to extend unbroken into quiescence in three sources, V404 Cyg (Gallo et al., 2003), GX 339–4 (Corbel et al., 2013), and XTE J118+480(Gallo et al., 2014). Further, please see section 1.3.1 for a detailed explanation of the disc instability model (Lasota, 2001; Done et al., 2007), which describes the transition from quiescence to outburst and back again in terms of thermal and viscous instabilities in a BHXRB accretion disc.

regions. The top panel in Figure 1.6 displays the complete morphology of the system in this state.

There is strong evidence for the absence of a jet in this state (lack of radio emission seen in 4U 1630–47, H 1743–322, XTE J1720–318; Fender et al. 2009), but fading optically thin emission has also been observed (seen in GX 339–4 and XTE J1550–564; Gallo et al. 2004, Corbel et al. 2002). It has been postulated that either there is still radio emission present but the emission is too faint to observe (at least an order of magnitude weaker then seen in the HS), or the core radio emission is suppressed and the radio emission observed occurs only as a result of re-brightenings as the jet propagates away from the source and interacts with the ISM (external shocks propagating through the surrounding medium). Recently, Ponti et al. (2012) demonstrated that accretion disc winds (revealed in X-ray spectra) can be observed in edge on (i.e., inclination of 90 deg) BHXRBs in the SS. Therefore, in contrast to the HS, outflows in the SS may take the form of strong accretion disc winds and weak or completely quenched core jet emission[10] (Fender and Gallo, 2014).

The accretion disc and inner flow primarily emit at X-ray frequencies. The X-ray spectrum is dominated by a hot, thermal disc component peaking at $\sim 1\,\mathrm{keV}$ from blackbody emission. A weak, non-thermal power-law ($\Gamma \sim 2$) tail with no high energy cutoff, from non-thermal comptonization of soft seed photons from the disc is also present (Homan and Belloni, 2005; McClintock and Remillard, 2006; Belloni, 2009; Zdziarski and Gierlinski, 2004; Done et al., 2007).

Steep Power-Law State: The SPL state can be seen at the top of the HID (indicated by letter E) in Figure 1.5. This state typically occurs at a very high X-ray intensity, corresponding to very large fractions of Eddington.

[10]It is postulated that during the transition between the HS and SS, there is not simply a rebalancing of total outflow power between the disc winds and steady jets, rather the winds may carry less kinetic power and more mass then steady jets.

The physical picture in this state consists of a truncated accretion disc (but to a lesser extent than the HS) and either one optically thick hybrid inner flow region (thermal/non-thermal distribution of electrons[11]) or two separate optically thick inner flow regions (one non-thermal region[12] and one thermal region[13]). The middle panel in Figure 1.6 displays the complete morphology of the system in this state.

The structure of the jet in this state is very uncertain. Theories suggest a very large outburst (McClintock and Remillard, 2006; Corbel et al., 2004), discrete multiple ejections (as seen in GRS 1915+105; Fender 2001), or a quenched jet similar to the SS (as seen in XTE J1550–564; Corbel et al. 2001).

The accretion disc and inner flow primarily emit at X-ray frequencies. The X-ray spectrum contains a strong thermal disc component from blackbody emission which merges smoothly into a very steep power-law ($\Gamma > 2$) tail. This tail can extend up to $\sim 1\,\mathrm{MeV}$ with no high energy cutoff, from a combination of thermal and non-thermal Comptonization (Homan and Belloni, 2005; McClintock and Remillard, 2006; Belloni, 2009; Zdziarski and Gierlinski, 2004; Done et al., 2007).

Transitions between states (often referred to as intermediate states): As the system leaves quiescence it starts in a lower-luminosity HS where we have a truncated accretion disc, hot inner flow (corona) and steady jet (displayed in A in Figure 1.5). The jet is thought to have a low bulk Lorentz factor. As the X-ray luminosity rises the disc begins moving inwards and the steady jet continues to build up (displayed in B) with jet emission strongly correlating with the X-ray emission. The X-ray spectrum begins to soften as the disc

[11]This region is hypothesized to have started out as a non-thermal distribution of electrons. Scattering would cause a hybrid distribution as low energy electrons cool through Coulomb collisions (electrons scattering off electrons) and high energy electrons cool through Comptonization.

[12]This could be a magnetic reconnection region above the disc or non-thermal electrons from the jet.

[13]This could be a remnant of the corona from the HS.

moves further inward and the jet velocity is thought to increase as the source approaches the jet line (dot-dashed line). The jet line can be viewed as an idealized (steady) jet-producing / (steady) jet-free boundary. As the source crosses this line, the faster moving jet catches up with the slower moving jet causing the propagation of internal shocks down the jet and possibly a major ejection event (displayed in C). In this phase an optically thick steady jet is no longer present and is replaced by optically thin discrete ejections. After these flaring events the optically thin emission will fade and the system enters the SS, where core jet emission is (most likely) suppressed as the accretion disc reaches the ISCO (displayed in D). Some sources have been observed to make repeated excursions back across the jet line where the jet switches back on again (dashed line). In addition, some sources have been known to enter the very high luminosity SPL state (displayed in E)[14]. As X-ray luminosity drops, the disc will recede and the jet is reactivated as the system crosses the jet line again. However, this time there will be no internal shocks (no slower moving jet to catch up to) as the system transitions back to the HS at a lower luminosity and moves back into quiescence (Russell et al., 2012; Fender and Belloni, 2004; Fender et al., 2004; Fender, 2003, 2006; Fender et al., 2009).

[14]See Done et al. (2007) for detailed explanations of how the system could smoothly transition from both the HS to the SPL and the SS to the SPL.

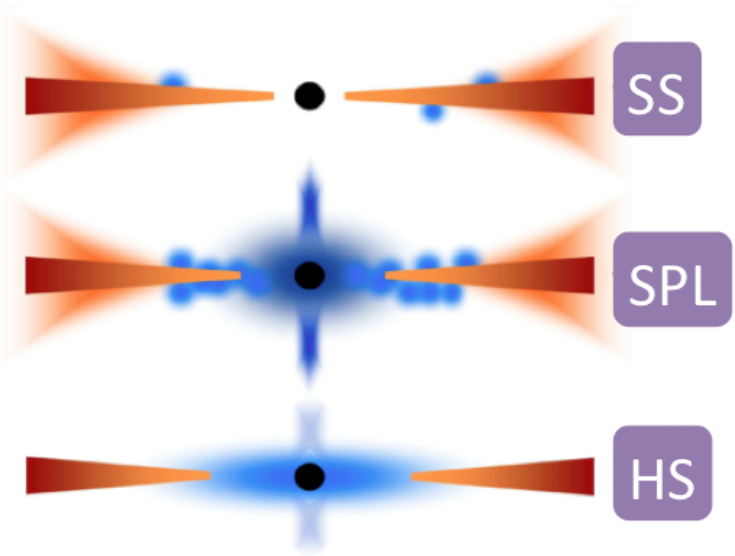

Figure 1.6: Morphology of BHXRB accretion flow in different accretion states. The bottom diagram represents the hard state with a truncated accretion disc, hot inner flow (corona) and steady jet. The top diagram represents the soft state with the accretion disc extending down to the ISCO, an inner flow located in localized regions over the disc and no jet. The middle diagram represents the SPL state with a truncated accretion disc, a hybrid inner flow and unknown structure of the jet. Figure adapted from Done et al. (2007).

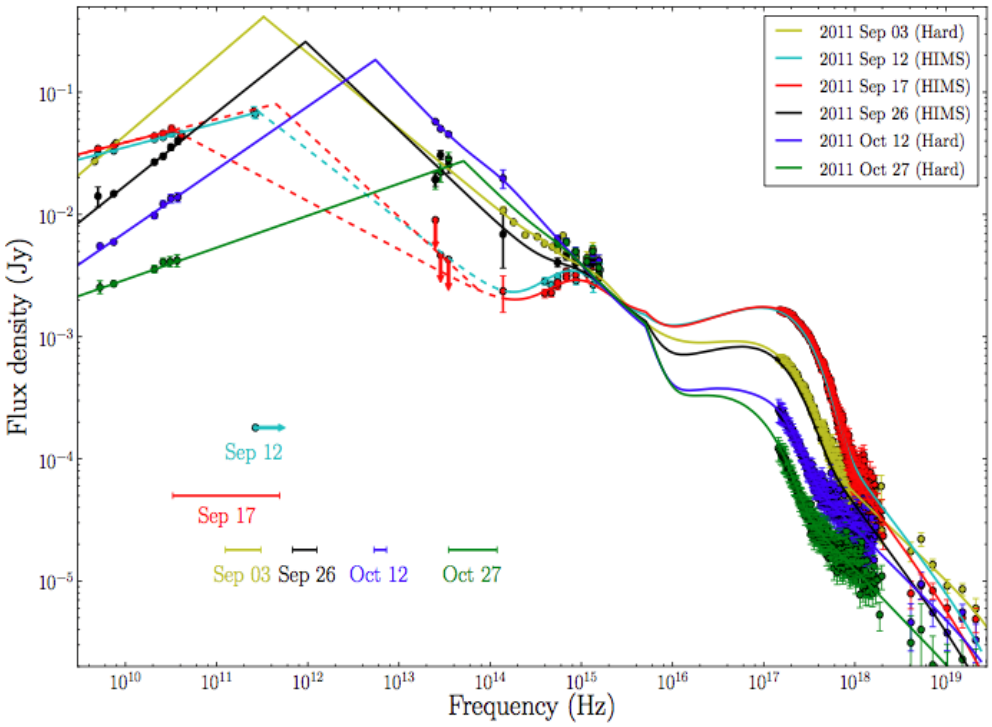

Figure 1.7: Broadband SED of BHXRB source MAXI J1836–194 in the hard accretion state (HS) during its 2011 outburst. Different colours represent data taken in different epochs. The solid/dashed lines indicates model fits to the data and horizontal lines indicates the prediction of the location of the jet spectral break. The radio through IR frequencies are fit by a broken power-law from jet synchrotron emission; the X-ray regime is fit with weak blackbody emission from the accretion disc and a dominant high energy power-law due to comptonization of seed photons from the accretion disc in the hot inner flow of the corona. Irradiation and reprocessing of X-ray photons in the outer accretion disc account for the bump in optical/UV regime (Russell et al., 2014). Note that this source underwent a "failed" outburst and therefore never fully reached the soft state before fading back into quiescence.

1.2.2 Relativistic Effects in the Jet

Relativistic Beaming: Relativistic beaming is an effect in which radiation from a relativistically moving source appears concentrated in the direction of its velocity according to a stationary observer. This effect is a direct consequence of light aberration in the case where the emitting source material is moving relativistically. Light aberration describes the apparent shift in the direction of radiation emitted by a moving source as seen by a stationary observer, and is described as follows (Bradt, 2008),

$$\cos\,\theta = \frac{\cos\,\theta' + \beta}{1 + \beta\cos\theta'} \tag{1.1}$$

where ' denotes variables in the rest frame of the source, $\beta = \frac{v}{c}$, and θ represents the angle between the direction of motion and the line of sight. It is clear that for relativistic velocities approaching the speed of light, c ($\beta \rightarrow 1$), pointing towards the observer ($\cos\,\theta \rightarrow 1$) leads to $\theta \rightarrow 0$. Therefore regardless of the direction of emission in the source frame (θ') the stationary observer will see emission concentrated in the forward direction into a narrow beam[15].

If the source of radiation is relativistically moving electrons, such as those in jets, then in the source frame the electrons radiate in a dipole (double lobe) pattern. While in the observer frame where the radiation is beamed in the forward direction, the resulting radiation pattern is one large elongated front lobe and a small compressed back lobe (Rosswog and Bruggen, 2007).

Doppler Boosting: Doppler boosting is an effect that enhances/diminishes (boosts/de-boosts) the intensity of the received radiation from a relativistically moving source. This effect originates from a combination of the relativistic

[15]The beaming angle (θ_b) is defined as half the opening angle of the cone of radiation seen by the observer, which corresponds to a cone including half of the rays in the source rest frame ($\theta' = 90°$). It can be shown that in the highly relativistic case, $\gamma = \left(1 - \beta^2\right)^{-\frac{1}{2}} >> 1$, $\theta_b \sim \frac{1}{\gamma}$. Therefore, the more relativistic the source (larger γ), the more concentrated the beam of photons becomes.

Doppler effect and relativistic beaming. Consider the following Lorentz invariant quantity (Rybicki and Lightman, 1979),

$$\frac{I_\nu(\nu)}{(\nu)^3} = \frac{I'_\nu(\nu')}{(\nu')^3}. \tag{1.2}$$

The relativistic Doppler shift states,

$$\nu = D\nu' \tag{1.3}$$

where the relativistic Doppler factor is given by, $D = \frac{\sqrt{1-\beta^2}}{1-\beta cos\,\theta}$ and θ is the angle with the line of sight (see left panel below in Figure 1.8).

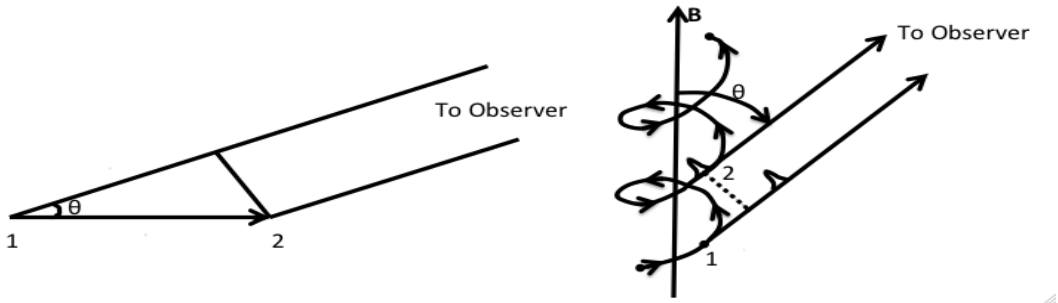

Figure 1.8: Schematic for the Doppler shift of a source moving toward the observer (left) and synchrotron radiation emitted by a particle moving toward the observer (right). The left panel displays a rapidly moving, periodically emitting source traveling from 1 to 2 in one period. The time interval between light pulses emitted at 1 and 2 in the source frame is different from the time interval between the received light pulses by the observer. The right panel displays the same effect with a particle emitting synchrotron radiation (Rybicki and Lightman, 1979).

Therefore, $I_\nu(\nu) = D^3 I'_\nu(\nu')$, where the intensity observed can vary greatly depending on the observer's location and the speed of the source (see Figure 1.9).

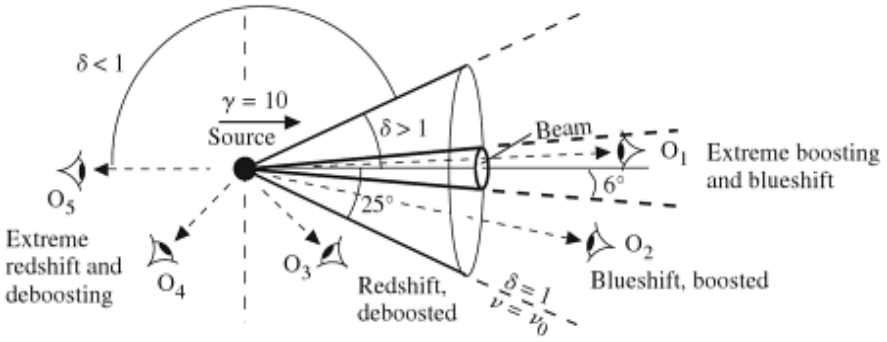

Figure 1.9: Schematic describing relativistic beaming and Doppler boosting. The source is emitting radiation isotropically in its rest frame and moving relativistically with respect to five different observers in a stationary frame. The beam corresponds to the half-cone beaming angle of $\frac{1}{\gamma}$ described above, and δ corresponds to the Doppler factor D where $\theta \to 0$ (Bradt, 2008).

Now considering a source of relativistically moving electrons following a power-law in the form[16] $I'_\nu(\nu') \propto \nu'^{\alpha}$, such as those in a jet emitting synchrotron radiation (see right panel in Figure 1.8) . The observed intensity at the same frequency transforms as $I_\nu(\nu) = D^{3-\alpha} I'_\nu(\nu)$ [17]. Therefore, the spectrum in the source frame is a power-law and remains so in the observer frame with the slope unchanged. The difference being that in the observer frame every frequency is shifted by the Doppler factor, D.

Superluminal Motion: Superluminal motion is an apparent motion that appears to be faster than the speed of light. Consider a discrete blob of emission (see Figure 1.10) ejected at a speed, v, and at an angle θ with respect to the line of sight, then the transverse distance travelled across the sky in some interval

[16]Flux density, S_ν follows this same dependence as intensity, I_ν.

[17]This doppler factor dependence is only true for discrete emission. For a continuous, isotropic jet the intensity is reduced by one doppler factor, $I_\nu(\nu) = D^{2-\alpha} I'_\nu(\nu)$, as the observed emitting volume is decreased by one power of the Doppler factor due to Lorentz contraction.

of time, Δt, becomes (Mirabel and Rodriguez, 1999; Rosswog and Bruggen, 2007),

$$v_{\rm trans} = \frac{d_{\rm trans}}{\Delta t} = v \sin\,\theta \tag{1.4}$$

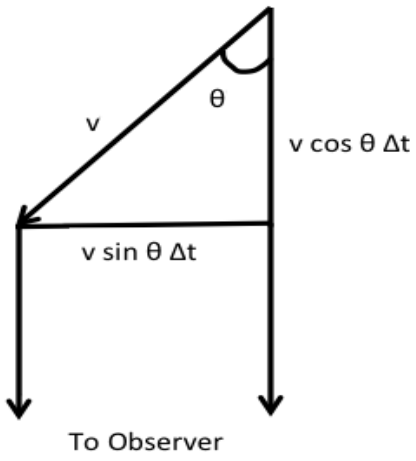

Figure 1.10: Schematic of the geometry of superluminal motion. The true motion of the source is represented by the vector, v, and θ represents the angle between the source and the line of sight with the observer (Mirabel and Rodriguez, 1999).

However, this is not the true transverse velocity across the sky. Due to the classical Doppler effect the interval between the reception of two photons by the observer is smaller than the interval between their emission. Therefore, we must replace Δt above by $\Delta t_{\rm obs} = \Delta t - \frac{v\cos\theta\Delta t}{c} = \Delta t(1-\beta\cos\theta)$, yielding the correct motion of the blob across the sky as seen by the observer,

$$\frac{v_{\rm trans}}{c} = \frac{\beta\sin\theta\Delta t}{\Delta t_{\rm obs}} = \frac{\beta\sin\theta}{(1-\beta\cos\theta)} \tag{1.5}$$

For certain values of θ and β, $v_{\rm trans} > c$. At highly relativistic velocities like those present in a jet ($\beta \rightarrow 1$), angles of $\sim 5^\circ - 10^\circ$ will produce apparent transverse velocities across the sky that exceed the speed of light.

1.3 Theoretical Framework

In the previous section we have outlined an observational picture with two main accretion inflows (accretion disc and an inner flow) and an outflow or jet. In this section I will take a more detailed look at the structure and emission mechanisms in these flows.

1.3.1 Structure & Emission Mechanisms in the Accretion Flow

Accretion Disc: In BHXRB systems the accretion disc is confined close to the orbital plane, and thus the thin disc model first developed by Shakura & Sunayev (Shakura and Sunyaev, 1973) has been successful in describing observations. This thin disc can be characterized by a surface density, $\Sigma(R,t)$ (mass per unit surface area). Considering an annulus of the disc material between R and $R+\Delta R$, conservation of mass and angular momentum yield the following relation (Done, 2014; Spruit, 2014; Done et al., 2007; Frank et al., 2002),

$$\frac{\partial \Sigma}{\partial t} = \frac{3}{R}\frac{\partial}{\partial R}\left(R^{\frac{1}{2}}\frac{\partial}{\partial R}\left(\nu\Sigma R^{\frac{1}{2}}\right)\right) \tag{1.6}$$

where ν represents viscosity[18]. This relation governs the time evolution of the surface density and is known as the thin disc diffusion equation (Frank et al., 2002; Spruit, 2014).

For many systems the mass transfer rate onto the disc changes on timescales longer than the viscous timescale (timescale for which matter diffuses through the disc under the effect of viscous stresses and torques), and thus the disc can be assumed to be in a steady-state ($\frac{\partial}{\partial t} = 0$). The mass flux ($\dot{M}$) is constant

[18]Shakura & Sunayev parametrized viscosity with the α prescription, $\nu = \alpha c_s H$, where c_s is speed of sound and H is disc thickness ($\frac{H}{R} < 0.01$ in BHXRBs) (Frank et al., 2002). Viscous stresses in the disc are now known to be the result of the magneto-rotational instability (MRI), please see below for more details.

throughout the steady-state disc and equivalent to the accretion rate onto the BH. Therefore, the surface density distribution becomes,

$$\nu\Sigma = \frac{\dot{M}}{3\pi}\left(1 - \left(\frac{R_{\rm in}}{R}\right)^{\frac{1}{2}}\right) \tag{1.7}$$

where $R_{\rm in}$ represents the innermost annulus at the ISCO (Frank et al., 2002; Spruit, 2014).

As the disc is optically thick, the photons will scatter off the electrons many times, resulting in the particles sharing kinetic energy and approaching thermal equilibrium. Thus we expect the flux emitted from an annulus to be that of a blackbody (Rybicki and Lightman, 1979),

$$F_{BB} = \sigma_{SB} T(R)^4 \tag{1.8}$$

where σ_{SB} is the Stephan-Boltzman constant and T is the blackbody temperature.

If an annulus of the disc is in local thermodynamic equilibrium, the flux radiated locally from that annulus[19] must be equal to the rate at which energy is deposited onto the annulus. Energy is deposited on the disc by viscous stresses that convert the gravitational potential energy of the in-falling matter into heat. Thus equating the viscous dissipation rate to the blackbody flux leads to the following temperature profile of an optically thick, geometrically thin accretion disc (Frank et al., 2002; Spruit, 2014),

$$\sigma_{\rm SB} T^4(R) = \frac{9}{8}\nu\Sigma\Omega = \frac{3GM\dot{M}}{8\pi R^3}\left[1 - \left(\frac{R_{\rm in}}{R}\right)^{\frac{1}{2}}\right] \tag{1.9}$$

The spectrum of the entire disc is simply the sum of blackbody components from different annuli in the disc. Larger luminosity (from stronger gravity)

[19] Assuming no advection, winds or jets.

and increasing temperature (from the disc emitting this luminosity from a smaller area) occur in components at smaller radii, with peak temperature and luminosity occurring at the ISCO, represented by $R_{\rm in}$.

The Shakura-Sunayev thin disc solution assumes that the accretion rate is constant with radius when in fact this is not entirely true, thus these discs are subject to instabilities. The accretion flow can be *thermally unstable* if small perturbations in temperature grow. Similarly, the flow can be *viscously unstable* if a small increase in mass accretion rate grows, resulting in the disc being eaten away at a particular radius (Done et al., 2007; Done, 2014). There are two main instabilities that occur in the Shakura-Sunayev disc, the hydrogen ionization instability and the radiation pressure instability.

Hydrogen Ionization Instability: This instability controls long term outburst behaviour and occurs at low luminosities and mass accretion rates. At low mass accretion rates the temperature is low enough that most of the material is neutral and the opacity is very low. However, when temperatures reach those correlated with H ionization ($10^4 - 10^5$ K), the opacity can rise very steeply with only small increases in temperature. Due to the higher opacity, photons are absorbed by the disc, keeping their energy within the disc, which leads to a further increase in temperature, and in turn allows more and more photons to ionize H. This thermal runaway only stops when H is completely ionized (Done et al., 2007).

This thermal instability will trigger a viscous instability since the disc is now ionized, the hot plasma particles are tied to the field lines, and thus (inversely) the magnetic field lines are frozen into the accretion flow. The viscous instability is governed by the Magneto-rotational Instability (MRI) mechanism, described in Figure 1.11 below, where weak magnetic fields cause inward mass flow and outward angular momentum transport in a differentially rotating disc (Balbus, 2003; Balbus and Hawley, 1991). As a result, the mass transfer rate through the annulus will be larger than the input mass transfer rate, causing

the material in the annulus to be eaten away. In turn, pressure will decrease, heating will decrease, and the temperature will decrease until H is able to recombine and trigger the thermal instability again, except in reverse. The annulus will cool and subsequently the mass transfer rate decreases. Eventually the material becomes completely neutral below $\sim 10^4$ K, and the cycle begins again as the disc begins to build up (Done et al., 2007).

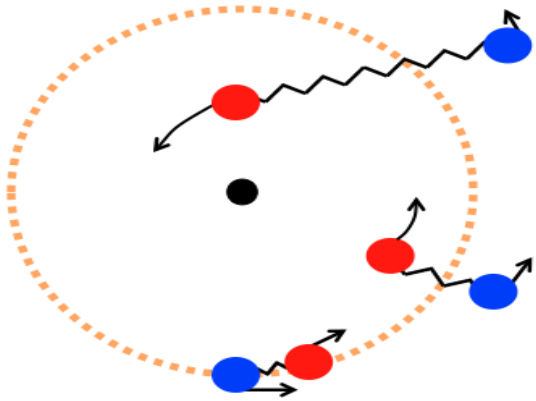

Figure 1.11: This schematic displays the mechanical process of the MRI by drawing an analogy between magnetic tension forces and spring tension forces. We begin with two neighbouring fluid elements in an annulus of a differentially rotating disc, connected by a spring (spring force analogous to magnetic tension force). The inner element rotates faster than the outer element causing the spring to stretch. This in turn forces the inner element to slow down, decreasing its angular momentum and moving it to a lower orbit. Similarly, the outer element is forced to speed up, increasing its angular momentum and moving it to higher orbit. As the elements move further apart the tension in the spring increases. This cycle will then continue, only with the two elements initially further apart (Done et al., 2007; Balbus, 2003; Balbus and Hawley, 1991).

Even though the above instabilities are purely local instabilities, the discontinuous jumps in temperature and mass transfer rate have the ability to affect the next annulus in the disc. Therefore, the whole disc cycles between a disc which is being eaten away (larger mass transfer rate onto the BH than input mass transfer rate from the companion) to a quiescent disc where H is mostly neutral everywhere. This cycle can be described by the disc instability

model, which, for instance, summarizes the process in terms of an outburst in a BHXRB accretion disc. A quiescent disc is built up due to steady mass transfer from the companion. Eventually the disc temperature will rise high enough to trigger the H ionization instability at a certain radius. The increased temperature and increased mass transfer rate effects the next disc annuli resulting in a heating wave that propagates inwards through the disc. Initially, irradiation from the inner disc is strong enough to keep the outer parts of the disc hot, despite the high mass accretion rate eating away at the disc. But eventually, the temperature and mass accretion rate through the disc are decreased enough to weaken the X-ray irradiation and allow the outer disc to drop below the H ionization temperature. This in turn triggers a cooling wave that propagates through the disc bringing it back to quiescence (Lasota, 2001; Done et al., 2007).

Radiation Pressure Instability: This instability is predicted to occur at higher luminosities and mass accretion rates such as in the SPL state[20]. Currently there is little observational evidence for this instability occurring, however, the unique variability seen in the BHXRB source, GRS 1915+105, which spends a large amount of time at high luminosities close to Eddington, could be evidence for such an instability occurring (Done et al., 2007).

Hot Inner Flow (Corona): In contrast to the geometrically thin Shakura-Sunayev accretion disc, the accretion flow in the corona (in the HS) is geometrically thick and thus pressure forces become important in addition to centrifugal forces to balance gravity. If these pressure forces are due to gas pressure, the accretion flow must be hot with protons that are close to the virial temperature of $10^{12}\,\mathrm{K}$. While at the same time, in order to produce the high energy tail (cut off at $\sim 100\,\mathrm{keV}$) in the spectrum through Comptonization, the electrons must be at $\sim 10^{9}\,\mathrm{K}$. To satisfy these two different temperature requirements

[20]Please see Done et al. (2007) for more details.

we need a two temperature plasma where the ion temperature is hotter than the electron temperature. This type of plasma is possible when the density and optical depth are both very low. The electrons will radiate more efficiently than the protons, thus the protons will always be at a higher temperature as long as they do not interact enough to come into equilibrium (i.e., the flow must be optically thin to proton-electron collisions) (Done et al., 2007; Shapiro et al., 1976).

Accretion flows which satisfy the above conditions are known as Radiatively Inefficient Accretion Flows or RIAFs. Most of the gravitational energy is transferred to the ions at a fast rate, the energy transfer between ions and electrons is slow and electron energy losses are fast (via Comptonization). Therefore, RIAFs are very radiatively inefficient because the ions, which receive most of the gravitational energy, do not get to transfer their energy to the elections before falling into the BH (Spruit, 2014). Ichimaru and Rees (Ichimaru, 1977; Rees et al., 1982) recognized that advection of gravitational energy by protons becomes very important in a two temperature plasma, which lead to a series of RIAF models that take advection into account, the Advection Dominated Accretion Flows or ADAFs. The classic ADAF models, created by Narayan & Yi (Narayan and Yi, 1995; Yi, 1999), consider a steady, axisymmetric, rotating accretion flow where the equations for conservation of mass, radial momentum, angular momentum and energy are as follows,

$$\rho R H v_R = \text{const.} \tag{1.10}$$

$$v_R \frac{\partial v_R}{\partial R} - (\Omega^2 - \Omega_K^2) R = -\frac{1}{\rho} \frac{\partial}{\partial R} \left(\rho {c_s}^2 \right) \tag{1.11}$$

$$\rho R H v_R \frac{\partial (\Omega R^2)}{\partial R} = \frac{\partial}{\partial R} \left(\nu \rho R^3 H \frac{\partial \Omega}{\partial R} \right) \tag{1.12}$$

$$q_{adv} = q^+ - q^- \equiv f q^+ \tag{1.13}$$

With R representing the radius from the BH, ρ is the gas density, H is

the thickness/vertical scale height [21], v_R is the radial velocity, Ω is the angular velocity, $\Omega_K = \left(\frac{GM}{R^3}\right)^{\frac{1}{2}}$ is the Keplarian angular velocity, c_s is the sound speed, ν is the viscosity coefficient, T is the local mid-plane temperature and s is the entropy of the gas.

The energy terms are defined as follows, the viscous dissipation rate is $q^+ = \nu\rho R^2 \left(\frac{d\Omega}{dR}\right)^2$, the radiative cooling rate is q^-, the radial advection rate is $q_{adv} = \rho v_R T \frac{ds}{dR} = \frac{\dot{M}}{2\pi R^2} c_s^2 \xi$ and f is the advection fraction. Assuming that the advected energy fraction, f, is constant, the four conservation equations along with $\nu = \frac{\alpha {c_s}^2}{\Omega_K}$ completely describe the accretion flow in terms of four variables $v_R,\ \Sigma = 2H\rho,\ c_s^2$, and Ω (Frank et al., 2002).

Different radiative cooling processes will contribute to the q^- energy term above and will give rise to different spectral components. Comptonization is believed to be responsible for the high energy power-law tail seen in the spectra in all accretion states to some degree. This scattering process involves an energy exchange between photons and electrons. For an incoming photon of energy, $\epsilon_{\rm in}$, hitting an electron, the scattered photon energy is given by (Done, 2014),

$$\epsilon_{\rm out} = \frac{\epsilon_{\rm in}(1 - \beta cos\theta_{\rm ei})}{1 - \beta cos\theta_{\rm eo} + \left(\frac{\epsilon_{\rm in}}{\gamma}\right)(1 - cos\theta_{\rm io})} \tag{1.14}$$

where, $\theta_{\rm ei}$ is the angle between the direction of propagation of the electron and input photon, $\theta_{\rm eo}$ is the angle between the the direction of propagation of the electron and output photon, $\theta_{\rm io}$ is the angle between the direction of propagation of the input and output photons, and $\gamma = (1-\beta^2)^{-\frac{1}{2}}$ is the electron Lorentz factor. This equation simply indicates that the electron and input photon share energy between them. For the simplest case of a photon hitting a stationary electron, momentum conservation causes the electron to recoil from the collision and the photon in turn loses energy in what is known as Compton scattering or down-scattering. A situation involving moving electrons, where

[21] Alternatively, in terms of surface density Σ described above, $\Sigma = 2H\rho$.

in a collision the more energetic electrons will give energy to the photons, is known as Inverse Compton scattering or up-scattering.

In the HS a thermal distribution of electrons is present, where the electron temperature[22] is defined as $\Theta = \frac{kT_e}{m_e c^2}$. For isotropic distributions of photons and electrons (with $\Theta << 1$), averaging over all angles yields,

$$\epsilon_{\rm out} = (1 + 4\Theta + 16\Theta^2 + \dots)\epsilon_{\rm in} \approx (1 + 4\Theta)\epsilon_{\rm in} \tag{1.15}$$

Thus the change in energy from a single scattering becomes,

$$\epsilon_{\rm out} - \epsilon_{\rm in} = \Delta\epsilon = 4\Theta\epsilon_{\rm in} \tag{1.16}$$

It is clear photons are up-scattered, but since the photons cannot gain more energy than the electrons started with, this relation only holds for $\epsilon_{\rm out} \lesssim 3\Theta$.

To determine how the spectrum in this state is produced, consider that in order for a collision to occur, there must be an electron in the volume swept out by a photon. This volume can be defined by path length, R, and cross-sectional area, σ_T (Thompson cross-section). Optical depth is then simply defined as the number of electrons within this volume (n is electron number density),

$$\tau = nR\sigma_T \tag{1.17}$$

In turn, the scattering probability is given by $e^{-\tau} \approx 1 - \tau$ for $\tau << 1$.

Therefore, we start with some seed photons at energy, $\epsilon_{\rm in}$, where some fraction, τ, are scattered in optically thin material to energy, $\epsilon_{\rm out,1} = (1+4\Theta)\epsilon_{\rm in}$. The scattered photons can be scattered again to $\epsilon_{\rm out,2} = (1 + 4\Theta)\epsilon_{\rm out,1} = (1 + 4\Theta)^2\epsilon_{\rm in}$ and so on until they reach the limit of electron energy after N scatterings with $\epsilon_{{\rm out},N} = (1 + 4\Theta)^N\epsilon_{\rm in} \sim 3\Theta$. As the fraction of photons scattered (τ) and their energy boost $(1 + 4\Theta)$ stays constant these series of

[22]The electron temperature sets the typical random velocity, $v^2 \sim \frac{3kT_e}{m_e}$ and thus $\beta^2 = 3\Theta$.

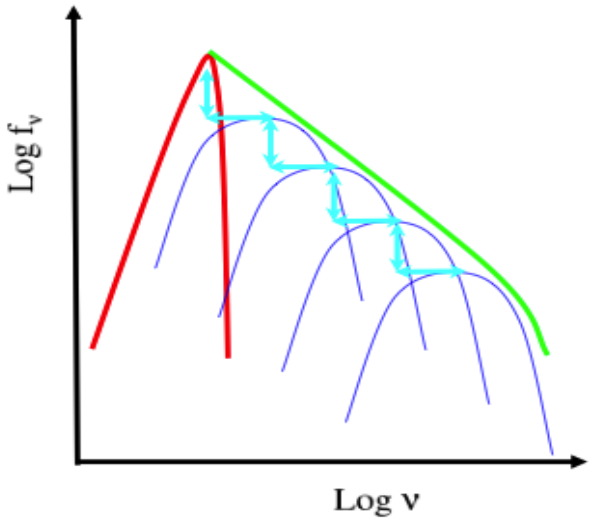

Figure 1.12: This schematic displays the spectrum that is built up from repeated thermal Compton up-scatterings in optically thin material. A fraction of seed photons (red) are boosted in energy by a constant factor $1 + 4\Theta$ and thus form the seed photons of the next scattering (dark blue). Each scattering order is shifted down and to the right by the same factor (cyan) to form the power-law spectrum (green) (Done, 2014).

.

scatterings result in a power-law spectrum extending from the seed photon energy, $\epsilon_{\rm in}$ to 3Θ. The power-law is $\propto \epsilon^{-\Gamma}$ with spectral index, $\Gamma = \frac{\ln \tau}{\ln(1+4\Theta)}$ depending on the electron temperature and optical depth. This spectrum is what we generally see in the HS (see Figure 1.12).

In the SS, the high energy power-law tail is produced by non-thermal Compton up-scattering. The electrons have a power-law distribution, $n(\gamma) \propto \gamma^{-p}$ extending from $\gamma = 1$ to γ_{max}, rather than the Maxwellian thermal distribution seen in the HS. For isotropic distributions of photons and electrons, averaging over all angles yields,

$$\epsilon_{out} = \left(\frac{4}{3}\gamma^2 - 1\right)\epsilon_{in} \approx \gamma^2 \epsilon_{in} \tag{1.18}$$

Therefore, we start with some seed photons at energy, $\epsilon_{\rm in}$, where a fraction,

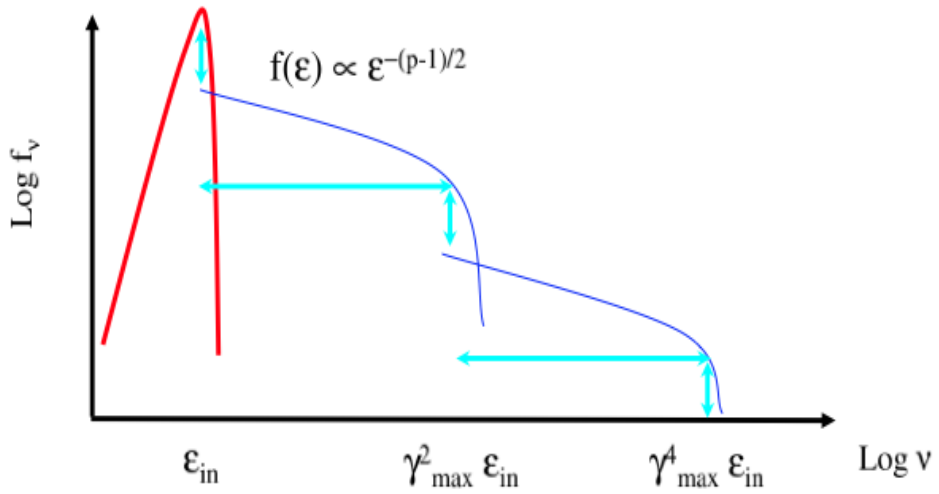

Figure 1.13: This schematic displays the spectrum that is produced by non-thermal compton up-scattering. The seed photons (red) produce a power-law (dark blue) through a single scattering due to the initial power-law electron distribution (Done, 2014).

τ, are scattered in optically thin material to energy, $\gamma^2_{\rm max}\epsilon_{\rm in}$. These scattered photons can be scattered again to $\gamma^2_{\rm max}(\gamma^2\epsilon_{\rm in}) = \gamma^4\epsilon_{\rm in}$, however, this large energy boost will cause them to reach the electron energy limit, $\epsilon_{\rm out} = \gamma_{\rm max}$ quickly. This produces a power-law spectrum extending from $\epsilon_{\rm in}$ to $\gamma^2_{\rm max}\epsilon_{\rm in}$ from a single scattering. The power-law is $\propto \gamma^{-(p-1)} \propto \epsilon^{-\frac{(p-1)}{2}}$, where the spectral index, $\Gamma = \frac{(p-1)}{2}$ (see Figure 1.13).

While the classic ADAFs described above only considered advection as a cooling process, Yuan (2001) expanded the classic ADAF and showed that advection could also be a heating process ($f < 0$, at higher mass accretion rates). These more general models became known as Luminous Hot Accretion Flows or LHAFs and are potential candidates to describe the hybrid inner flow in the SPL state. Additionally, in both ADAFs and the more general LHAFs, it is energetically possible for a fraction of the accreting material to escape in the form of winds, outflows, or jets carrying away mass, angular momentum

and energy. This leads to a solution that extends the classic ADAF, known as Adiabatic Inflow-Outflow Solutions (ADIOS; Blandford and Begelman 1999). It is clear that the structure of this ADAF type accretion flow is very complex and depends highly on the assumed conditions in the flow. As such a family of different models, which consider various combinations of these conditions, exists. For instance, CDAFs take into account convection (Abramowicz and Igumenshchev, 2001), MDAFs take into account magnetic fields (Meier, 2005) and JDAFs take into account outflows/jets (see Section 1.3.3 for more details; Falcke et al. 2004). Ultimately ADAFs still cannot completely describe this complex accretion flow, and many believe that magnetohydrodynamic (MHD) simulations in full general relativity, including radiative cooling, are probably needed to fully explore their complex properties (Done, 2014).

Further, to connect the two types of accretion inflows outlined above (cool, geometrically thin, optically thick disc at far distances from the BH and the ADAFs close to the BH), a mechanism known as the evaporation instability is invoked. If the cool disc is in thermal contact with the hot inner flow then there is heat conduction between the flows. Therefore, either the disc will evaporate into the hot flow, or the hot flow will condense into the disc. At low accretion rates, evaporation dominates, producing the geometry of the truncated disc and inner flow in the HS (Done, 2014).

1.3.2 Emission Mechanisms in the Jet

In relativistic jets the most important emission mechanism is synchrotron radiation (Fender, 2014). This type of emission occurs as the result of relativistic electrons spiralling around magnetic field lines. The magnetic force accelerates the charged particles (electrons and positrons) according to the relativistic equation of motion ($m\gamma\frac{dv}{dt} = \frac{q}{c}v \times B$), which are then able to emit photons and lose some of their kinetic energy[23] ($\frac{dE}{dt} \propto \gamma^2 B^2$). As discussed above, for a relativistically moving source, emission is beamed (according to the stationary observer) in the direction of motion within the angles $-\frac{1}{\gamma} < \phi < \frac{1}{\gamma} = 0$. As this beam sweeps past the observers line of sight, a pulse of radiation is observed, whose Fourier transform leads to the observed spectrum. Thus the observed frequency of the beamed radiation becomes, $\nu_{\text{sync}} = \frac{1}{2\pi mc}\gamma^2 eB\sin\psi$, with ψ representing the pitch angle between the velocity and magnetic field (Longair, 2011; Rybicki and Lightman, 1979; Bradt, 2008; Rosswog and Bruggen, 2007).

In astrophysical systems, we must consider particles that are not all at the same energy but have a distribution of energies. Consider a power-law distribution of electrons radiating isotropically, like those assumed to be present in relativistic jets,

$$N(\gamma)d\gamma = K\gamma^{-p}d\gamma \tag{1.19}$$

where $N(\gamma)d\gamma$ is the number density of electrons in the interval $\gamma + d\gamma$. If we assume all radiation is emitted isotropically from each volume element (a valid assumption when dealing with tangled magnetic fields in which magnetic fields along the line of sight have many random directions or are chaotic), the emission coefficient becomes (Longair, 2011),

[23]This emitted radiation power is calculated from the relativistic Larmor formula, $\frac{dE}{dt} = \frac{2q^2}{3c^3}\gamma^4(a_\perp^2 + \gamma^2 a_\parallel^2)$ for an isotropic distribution of velocities. Considering only **B** fields, the acceleration perpendicular and parallel to the electron velocity are $a_\perp = \frac{qB}{\gamma m_e c}v_\perp$ and $a_\parallel = 0$, respectively, leading to the $\gamma^2 B^2$ dependence of radiated power (Rybicki and Lightman, 1979).

$$j_\nu(\nu) = \frac{\sqrt{3}e^3BK}{4\pi\epsilon_0 c m_e}\left(\frac{3eB}{2\pi\nu m_e^3c^4}\right)^{\frac{(p-1)}{2}} A(p) \tag{1.20}$$

where the constant $A(p) = \frac{\sqrt{\pi}}{2}\frac{\Gamma\left(\frac{p}{4}+\frac{19}{12}\right)\Gamma\left(\frac{p}{4}-\frac{1}{12}\right)\Gamma\left(\frac{p}{4}+\frac{5}{4}\right)}{(p+1)\Gamma\left(\frac{p}{4}+\frac{7}{4}\right)}$. The key dependencies are $j_\nu(\nu) \propto KB^{\frac{(p+1)}{2}}\nu^{\frac{-(p-1)}{2}} = KB^{\alpha+1}\nu^{-\alpha}$.

With each emission process there is typically an accompanying absorption process. In the case of synchrotron radiation this process is known as synchrotron self-absorption. Self-absorption effects become important when the brightness temperature[24] ($T_b = \frac{I_\nu c^2}{2\nu^2 k}$) becomes equal to or greater than the thermal temperature of the radiating electrons ($T_k = \frac{2\gamma mc^2}{2k}$), which can occur at lower frequencies in typical radio sources. The absorption coefficient can be found to be (Longair, 2011),

$$\kappa_\nu(\nu) = \frac{\sqrt{3}e^3c}{8\pi^2\epsilon_0 m_e}KB^{\frac{(p+2)}{2}}\left(\frac{3e}{2\pi m_e^3c^4}\right)^{\frac{p}{2}} B(p)\nu^{-\frac{(p+4)}{2}} \tag{1.21}$$

where the constant $B(p) = \frac{\sqrt{\pi}}{8}\frac{\Gamma\left(\frac{3p+22}{12}\right)\Gamma\left(\frac{3p+2}{12}\right)\Gamma\left(\frac{p+6}{4}\right)}{\Gamma\left(\frac{p+8}{4}\right)}$. The key dependencies are $\kappa_\nu(\nu) \propto KB^{\frac{(p+2)}{2}}\nu^{-\frac{(p+4)}{2}} = KB^{\alpha+\frac{3}{2}}\nu^{-(\alpha+\frac{5}{2})}$.

Now applying the equation of radiative transfer[25] (Rybicki and Lightman, 1979),

$$\frac{dI_\nu}{ds} = -\kappa_\nu I_\nu + \frac{j_\nu}{4\pi} \tag{1.22}$$

and considering a region of thickness l, the solution becomes (Longair, 2011),

$$I_\nu = \frac{j_\nu}{4\pi\kappa_\nu}[1 - e^{-\kappa_\nu l}]. \tag{1.23}$$

[24]Brightness temperature is defined as the temperature of a blackbody having the same brightness as the source at that particular frequency. This term is often used in radio astronomy when the Rayleigh-Jeans law is applicable (Rybicki and Lightman, 1979).

[25]Note that these emission and absorption coefficients are only applicable in the fluid frame. To transform to the pattern frame (co-moving with bulk motion of jet) and the observer frame, the Lorentz invariants $\frac{j_\nu}{\nu^2}$ and $\nu\kappa_\nu$ as well as the relativistic Doppler equation can be used following a similar procedure as in Section 1.2.2. (Lind and Blandford, 1985).

If the source is optically thin ($\tau \sim \kappa_\nu l << 1$)[26],

$$I_\nu = \frac{j_\nu l}{4\pi}. \tag{1.24}$$

When considering the full functional forms of the emission and absorption coefficients we can see that $I_\nu \propto \nu^{-\alpha}$ where $\alpha = \frac{(p-1)}{2}$. If the source is optically thick ($\tau \sim \kappa_\nu l >> 1$),

$$I_\nu = \frac{j_\nu}{4\pi\kappa_\nu}. \tag{1.25}$$

When considering the full functional forms of the emission and absorption coefficients we can see that $I_\nu \propto \nu^{\frac{5}{2}}$. Therefore, the synchrotron emission spectra for a power-law distribution of relativistic electrons has an optically thick region at low frequencies, followed by a cutoff at higher frequencies where the spectrum breaks to an optically thin region (see Figure 1.14)[27] .

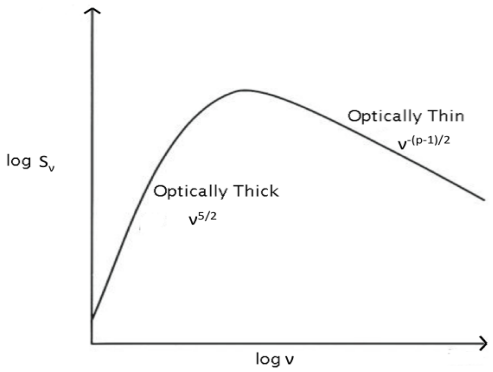

Figure 1.14: This schematic displays the synchrotron spectrum produced from a power-law distribution of electrons. The emission is assumed to be isotropic in a tangled magnetic field. An optically thick region is present at lower frequencies due to synchrotron self-absorption, where the spectral shape is independent of the electron energy distribution. The spectrum breaks to optically thin emission, where the spectral shape is dependent on the electron energy distribution ($N(\gamma)d\gamma = K\gamma^{-p}d\gamma$), and self-absorption effects are no longer present (Longair, 2011).

[26]Defining optical depth as $\tau = \int \kappa_\nu ds$.

[27]The specific intensity (I_ν) and spectral flux density ($S_\nu = \int I_\nu d\Omega$) have the same frequency dependence as the conversion only involves geometric factors (Rosswog and Bruggen, 2007; Bradt, 2008).

1.3.3 Modelling the Jet

Blandford and Konigl (1979) were the first to model relativistic jet emission successfully, where the flat/inverted radio spectrum is produced by the superposition of different overlapping synchrotron components (individual components seen in Figure 1.14) from many different regions of the jet. As the jet expands it becomes optically thick at lower frequencies and as plasma conditions change along the jet (decay of magnetic field and decrease in particle number density), conservation of particle number density and magnetic flux results in different synchrotron components peaking at unique frequencies. Since we are observing with a spatial resolution that is insufficient to resolve the individual components, we see a flat spectrum (see Figure 1.15).

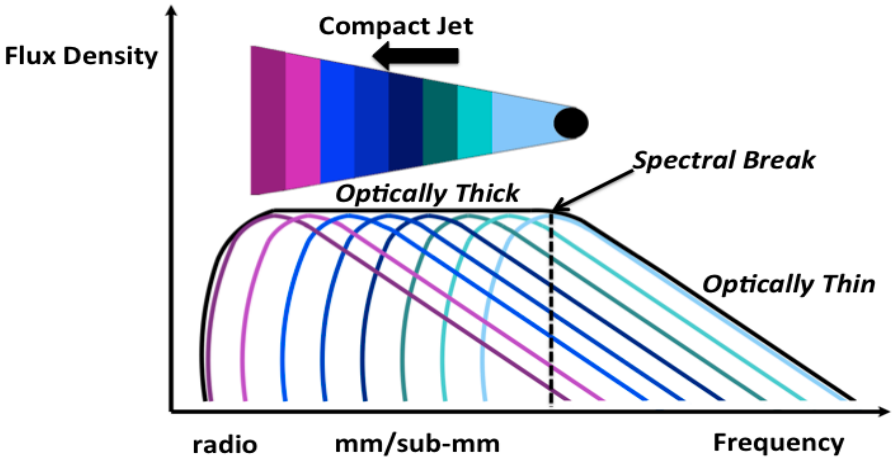

Figure 1.15: This schematic displays Blandford and Königl's theory where the superposition of overlapping synchrotron components from many different regions along the jet can produce the flat to slightly inverted broadband jet spectra that breaks to a steep power-law, and is observed in many BHXRB sources in the Galaxy.

This model has since become the canonical model of emission from (most) relativistic jets and is often still used today to interpret observations, although it is far from being able to completely describe jet behaviour. The model is limited by its simplifying assumptions: conical jets (which expand sideways at

a constant rate); jet material that moves at a constant bulk velocity along the jet axis; a magnetic field that is assumed to be perpendicular to the jet axis and frozen into the plasma; and both adiabatic (from expansion) and radiative (from synchrotron cooling) energy losses that are assumed to be replenished by an unknown continuous acceleration process. Since then, many variations on this model, both analytical and numerical, have been proposed that address and build upon some of these assumptions.

Considering electron energy losses will change the underlying electron energy distribution. Radiative synchrotron cooling losses can be quantified by their momentum losses (Longair, 2011),

$$\frac{d\gamma\beta}{dt}|_{\text{sync}} = -\frac{4\sigma_T}{3m_e c}\frac{B^2}{8\pi}(\gamma\beta)^2 \tag{1.26}$$

where the magnetic field decays along the jet according to $B(x) = B_0\left(\frac{x}{x_0}\right)^{-a_{jet}}$, $x = \gamma\beta ct$, x_0 defines the base of the jet, and a_{jet} defines jet geometry according to $r(x) = r_0\left(\frac{x}{x_0}\right)^{a_{jet}}$. Similarly, adiabatic losses from sideways expansion can be quantified as (Longair, 2011),

$$\frac{d\gamma\beta}{dt}|_{\text{ad}} = -\frac{2a_{jet}}{3t}\gamma\beta \tag{1.27}$$

Hjellming and Johnson (1988) developed a jet emission model focusing on adiabatic electron energy losses, but neglected radiative synchrotron losses. Georganopoulos and Marscher (1998) considered energy losses of relativistic electrons, but only considered the optically thin regime and angles close to the line of sight. Reynolds (1982) performs the most comprehensive study of jet emission in terms of including energy losses, but does not consider how self-absorption affects the electron energy spectrum. Approaching the problem from the other direction, instead of focussing on computing energy losses, there has been recent work exploring the use of internal shocks within the jet as a

continuous re-acceleration mechanism to replenish these energy losses (Jamil et al., 2010; Malzac, 2013).

Further, Kaiser (2006) took an entirely different approach, only considering a single acceleration episode, as well as the effects of decaying magnetic fields, both conical and confined geometry, and including both adiabatic and radiative energy losses as well as energy gains due to the effects of self-absorption. Contrary to Blandford and Königl's suggestion that energy losses need to be replenished to reproduce the observed flat spectrum, Kaiser finds that the effects of self-absorbtion allow flat spectra to be produced naturally without such a replenishment. Pe'er and Casella (2009) build on Kaiser's model but look at variations in the electron energy distribution. While Kaiser's and most previous jet emission models assume a power-law distribution of electrons in the entire energy range, models of particle acceleration in shock waves predict that this power-law distribution only exists at higher energies. In these circumstances, a significant fraction of electrons can maintain a low-energy thermal Maxwellian distribution, which under different conditions can produce a variety of complex spectra that differ from those found by Kaiser and his predecessors.

There also exists a family of models that work to connect the outflowing jet to the inner accretion flow. In these JDAF models (Markoff et al., 2001, 2005; Falcke and Biermann, 1995; Falcke and Markoff, 2000; Yuan et al., 2002), at the inner edge of the hot accretion flow, plasma is ejected out from a symmetric nozzle where it becomes supersonic. The jet particles then accelerate along the axes up to bulk Lorentz factors. The hot inner coronal flow is a good candidate for the base of the jet (Heinz and Sunyaev, 2003), where the hard power-law could either be an extension of the optically thin power-law from the synchrotron emission of non-thermal electrons at the base of the jet (Markoff et al., 2001) or from thermal Comptonization by electrons at the base of the jet, while the radio emission is from non-thermal electrons accelerated up the jet (Markoff et al., 2005). A jet can also be produced in MDAF models (Meier,

2005). Generally, to produce a jet there are two requirements, a strong, ordered magnetic field and some mechanism to get mass into this field, both of which are satisfied by a large scale-height accretion flow. Thus, in MDAFs, the MRI mechanism operating in a geometrically thick, hot accretion flow is sufficient to produce a jet.

Recently a group (Polko et al., 2010, 2013, 2014) has developed a new framework of relativistic magnetohydrodynamic (MHD) flow solutions that are self-similar, axisymmetric and for the first time include a full gravity (kinetic, electromagnetic and thermal inertia) term. This framework has the ability to link the inner (near BH where jets are launched) and outer (radio through IR synchrotron emission) jets like no other model. To do this, flow solutions which pass through three critical points (modified slow point, Alfven Point, modified fast point) need to be derived. The modified slow point (MSP) physically could represent the launch point and indicates the point where jet conditions are linked to the inner accretion flow. The modified fast point (MFP) physically could represent the acceleration point where re-collimation shocks occur and indicates where bulk flow velocity exceeds that of the magneto-sonic speed. Thus, by setting the conditions in the inner accretion flow, a unique jet model including geometry, velocity/pressure profiles and the location of particle acceleration (jet spectral break) can be found. The main advantage of this work is that it minimizes the free parameters, which is particularly useful as the model could potentially be applied to many different sources with a range of mass and power scales (other then just BHXRBs).

It is quite clear that there have been many attempts at modelling relativistic jets. Although many models are able to successfully produce the flat to slightly inverted jet spectra, typically seen observationally, they are still incomplete and far from being able to describe these jets fully. Some of the many challenges in modelling these objects are the inherent uncertainties that exist in describing main properties and processes within the jet.

Most notably uncertainties exist in:

- Acceleration & Launching process[28]: leads to uncertainties in energy distribution of electrons;
- Geometry & Structure: conical or confined jets, methods of confinement (e.g., external gas pressure, magnetic fields, or both);
- Microphysical processes in jet plasma: affects magnetic field evolution and in turn particle acceleration; and
- Energy in the magnetic field: equipartition or Poynting flux dominated jets.

Common practice for observers is to gloss over these difficulties by fitting the simplest power-law models (e.g., Blandford and Königl's model) to their data[29], which in itself represents another major obstacle to fully understanding relativistic jets.

1.3.4 Jet Launching Mechanisms

Several mechanisms of jet production and collimation have been suggested, however, the magnetically driven theory is currently favoured as magnetic acceleration mechanisms simultaneously produce the required relativistic velocities and collimation properties of these jets (Mirabel and Rodriguez, 1999; Meier et al., 2001). For this mechanism to accelerate and collimate outflows it needs a gravitating body to collect material (the BH), a polodial magnetic field threading the plasma, and differential rotation in the accretion flow. The differential rotation causes the magnetic field to form a helix type structure about the rotational axis. Magneto-centrifugal forces in this rotating helical field (known as Torsional Alfven Wave Train or TAWT) drive plasma trapped

[28]Briefly explored in the next section below.
[29]In this thesis I will largely adhere to this practice as well.

in it outward along the field lines. When magnetic fields are coiled in such a helical spiral, the fields will tend to shrink around its rotational axis to eliminate all but their straight axial component. This causes a pinching effect in which magnetic tension collimates the outflow into a jet. Depending on the specific conditions in the system, most notably the magnetic field, plasma density, and rotation, a variety of outflows can be produced, such as a broad uncollimated wind, a slowly collimating bipolar outflow, and a highly collimated jet (see Figure 1.16).

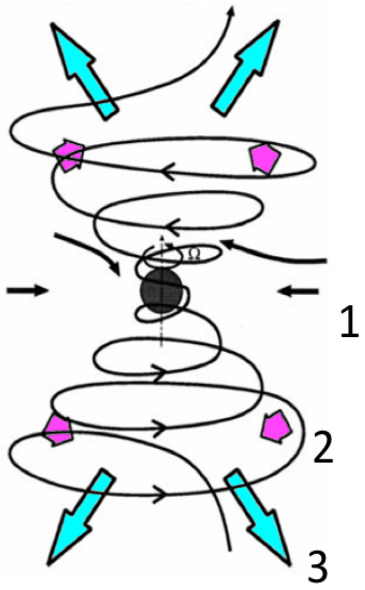

Figure 1.16: This schematic displays MHD acceleration and collimation processes. The magnetized, differentially rotating inflow towards the compact object (black arrows; 1) winds the magnetic field lines into a rotating helical coil. Magneto-centrifugal forces expel material along the field lines and magnetic tension or pinching forces (magenta arrows; 2) lift and collimate the outflow into jet (cyan arrows; 3). Figure adapted from Meier et al. (2001).

This MHD mechanism was first postulated by Blandford (Blandford, 1976) and since been applied to magnetized accretion discs and rotating BHs. These models can be mainly grouped into two separate streams of thinking:

- Blandford-Payne Mechanism (Blandford and Payne, 1982): *Extracting rotational energy and angular momentum from the accretion disc through magnetic fields anchored to the disc*: Since the Lorentz force only acts perpendicular to field lines, ionized gas tied to the magnetic field lines that protrude from the disc can only move freely along the lines like beads on a wire. Assuming a Keplerian disc, the centrifugal force balances gravity initially, but as you get farther from the BH, the centrifugal force can exceed the gravitational force and the gas tied to the field line is accelerated outward. At a certain height above the disc, the field lines do not co-rotate with the disc any longer as the gas inertia forces magnetic field lines to twist and wrap around the rotation axis forming a spiral structure that looks like a twisted rope. The loops in the spiral form a torodial field whose magnetic tension forces collimate the gas.

- Blandford-Znajek Mechanism (Blandford and Znajek, 1977): *Extracting spin energy of the BH through magnetic field lines*: Since magnetic field lines are threaded through the hot plasma of the accretion disc, matter being accreted onto the BH carries field lines with it, resulting in the field lines coming closer together as they get closer to the BH. Further, if the BH is rotating, frame dragging effects will cause the field lines to become twisted and coiled like a rope. The whole system can be envisioned to act like an electric circuit, the BH represents the battery, the magnetic field lines represent the wires, and the hot plasma represents the electric load. As current flows along the magnetic field lines, a quadrupole like electric field is generated, making it appear as if the BH horizon was a rotating conducting sphere. Unipolar induction (conductor rotating in magnetic field) produces an electric potential difference that can drive very powerful jets.

It is entirely possible that more than one launching mechanism could be operating in accreting BH systems under different conditions or at different scales. For instance, the Blandford-Znajek mechanism has been associated with transient type jets in Galactic accreting BH sources (Fender et al., 2010; Narayan and McClintock, 2012; Russell et al., 2013a; Steiner et al., 2013; Middleton et al., 2014). This theory has been indirectly tested observationally by measuring and comparing jet power and angular momentum of the BH (parametrized by the dimensionless spin parameter, $a_\star = \frac{cJ}{GM^2}$, where J represents the angular momentum of BH and M represents the mass of the BH), as jet power is proportional to the square of the spin in the Blandford-Znajek mechanism. However, different studies have led to conflicting results. While progress continues to be made, the nature of the jet launching mechanism still remains an open question in the field today, and is beyond the scope of this thesis.

1.4 The mm/sub-mm Regime

In the HS of a BHXRB outburst, jet emission is predicted to dominate over other system components (accretion disc and companion star) at frequencies below near-IR (Russell et al., 2006). As such, we have noticed a startling gap in our broadband coverage of these sources, the mm/sub-mm regime. Currently only a handful of detections of outbursting BHXRBs exist in the mm/sub-mm regime (Van der Horst et al., 2013; Russell et al., 2013a; Fender et al., 2001). The reason for the lack of detections is twofold:

- Until recently our instruments have not been sensitive enough to detect sources with flux densities[30] on the order of a mJy[31];

[30]Flux density is essentially a specific intensity (or brightness) integrated over the solid angle subtended by the source (Rohlfs and Wilson, 2000).

[31]Flux density is measured in units of $\mathrm{erg\,s^{-1}cm^{-2}Hz^{-1}}$. However, since flux densities in radio/mm/sub-mm sources are typically very small, astronomers usually express them in units of Janskys (Jy), where $1\,\mathrm{Jy} = 10^{-23}\mathrm{erg\,s^{-1}cm^{-2}Hz^{-1}}$ (Rohlfs and Wilson, 2000). BHXRB jets have been observed with flux densities on the order of a mJy (10^{-3}Jy).

- Our current understanding of jets has been largely shaped by radio measurements alone and thus we have not been looking in this regime.

Recent upgrades to such instruments as the Submillimeter Array (SMA) and the Submillimetre Common User Bolometer Array 2 on the James Clerk Maxwell Telescope (SCUBA-2 on the JCMT), as well as the introduction of new instruments such as the Atacama Large Millimetre Array (ALMA) are beginning to rectify the former, while we hope to continue to rectify the latter with this and future work.

With mm/sub-mm data we are able to fill in a gap of ~ 2 orders of magnitude in frequency in our broadband coverage. This is especially important when attempting to constrain the location of the spectral break. The flux and frequency of this spectral break are vital pieces of information as they can reveal insights into universal jet properties. For instance, the radiative power output of the jet is dominated by higher frequencies[32]. Thus in order to estimate the total radiative power of the jet, the break frequency (where peak flux density occurs), along with the luminosity at the break, and the radiative efficiency (fraction of kinetic energy radiated away) must be known. Further, an estimate of the total jet power (radiative + kinetic)[33], can lead to an estimate of the fraction of accretion energy channelled into the jets. Knowing the power contained in the jets at different luminosities can lead to insights into jet launching mechanisms and energy input into the surrounding ISM (Russell et al., 2012). Further, it is postulated that the jet spectral break marks the location where particle acceleration begins in the jet (Polko et al., 2010) and several jet models predict relations between the break frequency and key sys-

[32]Typically when observers create an SED, flux density, f_ν is plotted as a function of frequency, ν. However, to visualize where most of the power is located we need to plot νf_ν as a function of frequency. Adopting the power-law form of flux density, $f_\nu \propto \nu^\alpha$, and considering typical values of $\alpha_{\rm thick} = 0$, $\alpha_{\rm thin} = -0.5$, it is clear that higher frequencies hold the majority of the jet power (area under the curve).

[33]Assuming a canonical radiative to kinetic energy ratio of $\sim 5\%$ (Blandford, 1976; Fender et al., 2001).

tem parameters such as, accretion rate, BH mass, radius of the inner disc and magnetic field strength (Heinz and Sunyaev, 2003; Markoff et al., 2005; Pe'er and Casella, 2009; Casella and Pe'er, 2009; Heinz and Grimm, 2005; Markoff et al., 2003; Pe'er and Markoff, 2012; Chaty et al., 2011).

However, despite its importance, to date constraints on the location of this spectral break have been minimal in the literature. The break has been directly detected in only one source, GX 339–4 (Gandhi et al., 2011; Corbel and Fender, 2002), and indirectly constrained with extrapolation from radio frequencies through to the break frequency (through the unknown mm/sub-mm regime) in a few other BH sources, most recently in Cyg X−1 (Rahoui et al., 2011), MAXI J1659−152 (Van der Horst et al., 2013) and MAXI J1836−194 (Russell et al., 2013b). This extrapolation process introduces significant uncertainties in the derived location of the break (up to an order of magnitude in MAXI J1836-194). Data in the mm/sub-mm part of the spectrum will allow us to make direct spectral measurements intermediate between radio frequencies and the spectral break, mitigating the uncertainties that come with interpolation.

Further, recent results from observing campaigns of BHXRB sources, MAXI J1836–194 and MAXI J1659–152, show an evolving SED, suggesting an evolving jet break. The break frequency appears to tend toward lower radio frequencies as the compact jet begins to switch off and the system reaches softer accretion states (Russell et al., 2013a; Van der Horst et al., 2013). With mm/sub-mm data we could directly track the evolution of the break through mm/sub-mm frequencies and down to the radio band. Tracking the break could allow us to correlate the changing break frequency with accretion properties, such as X-ray hardness[34], which is essential in understanding what physical processes (possibly in the accretion flow) are driving changes within the compact jet.

[34]Russell et al. (2014) found tenuous evidence that the break frequency may correlate with X-ray hardness in the BHXRB source, MAXI J1836–194.

Moreover, with high quality, well-sampled broadband SEDs (including the mm/sub-mm regime) we can uncover physical conditions in the jet such as, base jet radius, velocity, opening angle, FAZ (first acceleration zone; region where synchrotron power-law begins), and cross section & total energy of the electron population (Russell et al., 2012, 2013a). Understanding these jet properties is crucial in building a single model that accurately constrains the physics of jet production and evolution, as these properties are highly sought after observables that act as input parameters for such models.

The few mm/sub-mm detections to date in the literature have measured considerably higher fluxes than at radio frequencies ($\sim 40 - 70\,\mathrm{mJy}$). This result is surprising given that observers have traditionally found near flat radio spectra in jetted sources. Markoff et al. (2001) has suggested that these high mm/sub-mm fluxes could be "anomalous", in which the excess emission at mm/sub-mm frequencies was produced by a yet unknown process not included in standard jet models. Confirming that mm/sub-mm fluxes are not anomalous would help to vindicate the use of spectral breaks to probe jet properties. On the other hand, anomalous mm/sub-mm fluxes would require (constrain, and motivate) a detailed explanation of the physics at the base of the jet where the mm/sub-mm regime probes.

As the mm/sub-mm regime probes near the base of the jet, variability detected in this region could reveal insight into particle acceleration in the jet. Additionally, probing a region so close to the BH could constrain the geometry of the system and structure of magnetic fields near BHs (Pe'er and Casella, 2009).

The mm/sub-mm regime opens up a new window with which to study relativistic jets in BHXRBs, providing a new perspective on these objects and allowing observers to probe part of the jet that cannot be studied with the traditionally used radio and X-ray frequencies.

1.4.1 Swift J1745–26

Swift J174510.8-262411 (also known as Swift J1745–26) is a new transient black hole candidate (Vovk et al., 2012) source discovered in the Galactic centre region ($l = 2.11°, b = 1.40°$)[35] by NASA's Swift Burst Alert Telescope (BAT) on 2012 Sep 16 (Cummings et al., 2012a). An X-ray counterpart was discovered in the hard X-rays ($15 - 50\,\mathrm{keV}$) by the X-ray telescope (XRT) on the Swift satellite on 2012 Sep 17 (Sharufatti et al., 2012; Cummings et al., 2012b). X-ray spectral and timing observations from Swift and the International Gamma-Ray Astrophysics Laboratory (INTEGRAL) were used to classify this source as a Low Mass X-ray Binary (LMXB; where the low-mass is a description of the companion in relation to the BH, namely the companion has $M \lesssim 2M_{\odot}$) black hole candidate system. In addition, this outburst was classified as "failed" (similar to MAXI J1836–194), as the source only remained in the hard accretion state (HS), never reaching the soft state (SS). A radio detection was made on 2012 Sep 17-18 with the Karl G. Jansky Very Large Array (VLA) in the 5.0 and 7.45 GHz bands of $6.8 \pm 0.1\,\mathrm{mJy}$ and $6.2 \pm 0.1\,\mathrm{mJy}$, respectively (Miller-Jones et al., 2012). Based on spectral and timing analysis from XRT on 2012 Sep 18 Swift J1745–26 was deemed to be in the hard state (HS) at this time (Tomsick et al., 2012). In addition, follow-up radio observations with the Australia Telescope Compact Array (ATCA) found evidence for a partially self-absorbed compact jet (near flat spectral index, $\alpha_{5.5-9\,\mathrm{GHz}} = 0.05 \pm 0.04$; Corbel et al. 2012). During the beginning of this outburst of Swift J1745–26 we obtained the first simultaneous radio and multiple band mm/sub-mm observations of a BHXRB, combining data from the Karl G. Jansky Very Large Array (VLA), Submillimeter Array (SMA) and James Clerk Maxwell Telescope (JCMT, SCUBA-2) between 2012 Sep 20 and 2012 Sep 26.

[35] l and b represent Galactic coordinates. Galactic longitude (l) measures angular distance counterclockwise from the direction of the centre of the Galaxy, within the Galactic plane. Galactic latitude (b) measures angular distance perpendicular from the Galactic plane, where positive is upwards (Karttunen et al., 2003).

1.5 Goals of this Thesis

The main objective of this thesis is to begin exploring the relatively untested mm/sub-mm regime in Galactic BHXRBs. As such, I am only working with continuum data, focusing on first-order spectral properties. During the 2012 outburst of the BHXRB, Swift J1745–26 we obtained simultaneous broadband measurements across radio and multiple mm/sub-mm frequencies. This unique set of data gives me the opportunity to compare spectral behaviour by directly measuring the spectral indices in and between the radio and mm/sub-mm regimes. Additionally, we are able to probe an untested part of the jet spectrum (mm/sub-mm regime). In this thesis I present these measurements to determine whether the mm/sub-mm jet emission is consistent with typical jet models, where a simple power-law can accurately describe the radio through sub-mm jet spectrum. In addition, our measurements help constrain the origin of high mm/sub-mm fluxes that have been seen in a few other mm/sub-mm detected BHXRBs in outburst.

Chapter 2

Observations and Data Analysis

2.1 Fundamentals of (radio and) mm/sub-mm Instrumentation

To use data from a telescope for research an astronomer must understand how that instrument operates thoroughly enough to correctly reduce the data and identify the difference between instrumental errors and scientifically meaningful results. Thus analyzing data accurately from mm/sub-mm telescopes, both interferometric arrays and single dish telescopes, involves understanding how they collect data (both the physical principles and assumptions), the hardware used to collect the data (antennas and electronics) and the algorithms/software used to convert the measured data into scientifically meaningful units (data reduction). In the following sections I will present an overview of the fundamentals of interferometers and single dish bolometers, briefly describe some specific issues that need to be taken into account when observing at mm/sub-mm frequencies and outline the procedure used and problems encountered while reducing the data in this thesis.

2.1.1 Synthesis Arrays (Interferometers)

The angular resolution of a (radio and) mm/sub-mm telescope can be calculated from diffraction theory to obey the following relation,

$$\theta = 200 \frac{\lambda}{1\,\mathrm{mm}} \frac{1\,\mathrm{m}}{D} \mathrm{arcsec} \tag{2.1}$$

where θ is the angular resolution that can be achieved in units of arcsec, λ is wavelength at which you are observing in units of mm and D is diameter of the antenna in units of meters. Therefore, to obtain a resolution of 1 arcsec at 7 mm wavelength, an antenna of diameter 1400 m would be needed. Currently we do not have the materials or engineering capability to build such an instrument, with the largest single, fully steerable antenna being the 100 m antenna at Green Bank (Taylor et al., 1998). Interferometry can solve this problem, where we essentially synthesize a large aperture (needed to obtain high resolutions and sensitivity) through the summation of many pairs of separated antennas.

Consider an astrophysical phenomenon occurring at some location, $\mathbf{R}$, causing a time variable electric field, $\mathbf{E}(\mathbf{R}, t)$, which propagates away from the source and arrives at the location of the observer, $\mathbf{r}$. To simplify the calculations we will consider only a finite time interval of the varying electric field ($dt \sim \frac{1}{d\nu}$, i.e, quasi-monocromatic), where the field will be sinusoidal (represented by Fourier series). The properties of these "quasi-monocramatic" electric field components, $\mathbf{E}_\nu(\mathbf{r})$, can provide information on the nature of the object being observed. For instance, the correlation of this field at two different locations, $\mathbf{r}_1$ and $\mathbf{r}_2$ is represented by (Taylor et al., 1998),

$$V_\nu(\mathbf{r}_1, \mathbf{r}_2) = \langle \mathbf{E}_\nu(\mathbf{r}_1) \mathbf{E}^*_\nu(\mathbf{r}_2) \rangle \tag{2.2}$$

where * indicates the complex conjugate. This function is known as the spatial coherence function of the field and is what an interferometer measures.

To extract meaningful insights relating to the astronomical source being observed, a relation between this spatial coherence function and the distribution of brightness from the source (intensity) must be derived.

A Simple Interferometer: An interferometric array is essentially an ensemble of several two-element interferometers (pair of antennas) and thus its inner workings can be analyzed by considering a two-element interferometer seen in Figure 2.1. For simplicity I will initially adhere to the following idealistic assumptions then introduce corrections that describe a more realistic situation,

- Antennas fixed in space, no motion or rotation;
- Quasi-monochromatic (sinusoidal) signals;
- No frequency down-conversions (RF or radio frequency interferometer);
- Single polarization;
- No atmosphere distorting the wave; and
- Ideal linear electronics (no added noise).

This simple interferometer consists of two identical antennas, separated by a baseline[1] vector ($\mathbf{b}$), which are receiving signals from a source located in the vector direction, $\mathbf{s}$, at a frequency, ν. Assuming a plane wave, the electromagnetic wavefront from the source will reach one antenna at a time, $\tau_g = \frac{\mathbf{b}\cdot\mathbf{s}}{c}$ later than the other (geometric delay). After these electromagnetic signals pass through each antenna they are combined in the correlator (a voltage multiplying and time averaging circuit). The inputs into the correlator are the waveforms,

[1]The baseline length sets the resolution of the array.

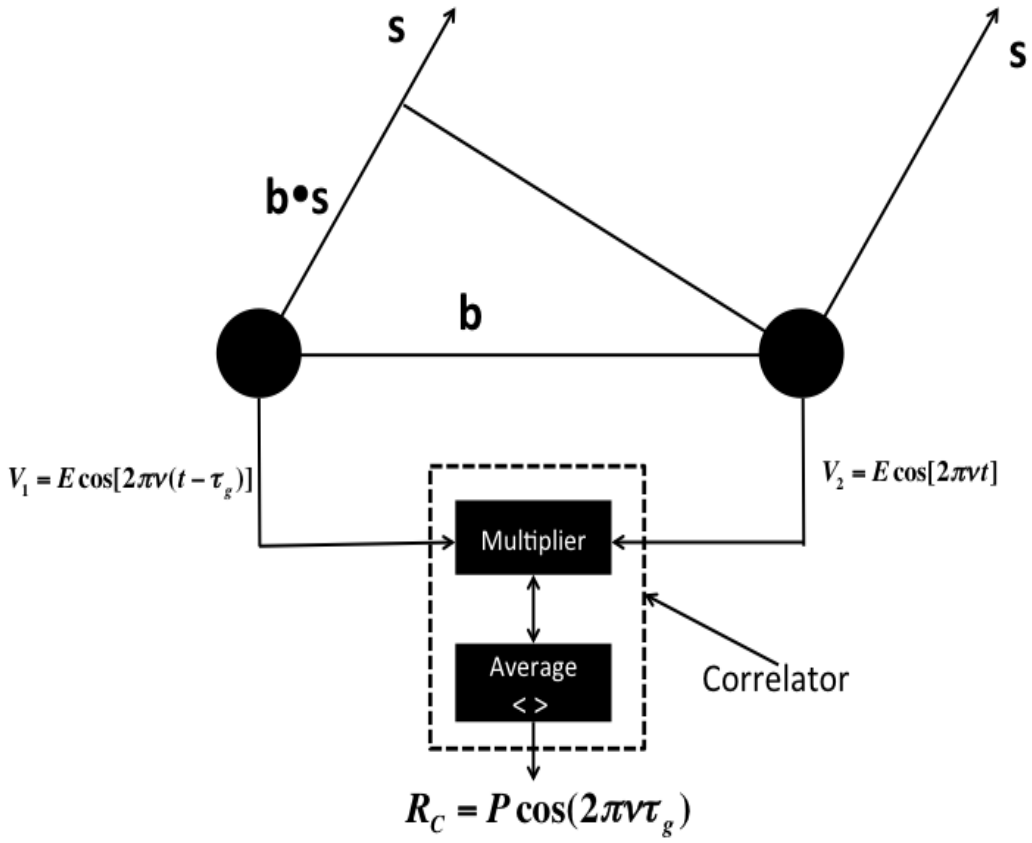

Figure 2.1: This schematic displays a simple two element RF interferometer that is stationary and receives quasi-monochromatic signals (Taylor et al., 1998).

$$\begin{aligned} V_1 &= E cos[2\pi\nu(t-\tau_g)] \\ V_2 &= E cos[2\pi\nu t] \end{aligned} \tag{2.3}$$

and the output is proportional to the time average of the voltages. This averaged product, known as the response, is dependent on the received power from the source ($P \propto E^2$) and can be written in the form,

$$R_C = P cos(2\pi\nu\tau_g) \tag{2.4}$$

To link the response measured with the interferometer to the source brightness on the sky, $I_\nu(\mathbf{s})$, the received power can be expanded to consider the power received from the source element, $d\Omega$,

$$R_C = \int\int I_\nu(\mathbf{s}) cos(2\pi\nu \frac{\mathbf{b}\cdot\mathbf{s}}{c}) d\Omega \tag{2.5}$$

The correlator can be thought of as casting a co-sinusodal fringe pattern onto the sky, which it will multiply by the source brightness and integrate (sum) the result over the entire sky. However, having one correlator is not enough as the cosine fringe pattern is an even function and thus the response to the odd part of the brightness distribution is zero. To completely recover the source brightness (including the odd piece) an odd fringe pattern (i.e. sine fringe pattern) is needed. To do this a 90 degree phase shift is placed[2] in one signal path, resulting in a second correlator response, $R_S = Psin(2\pi\nu\tau_g)$ (Taylor et al., 1998).

The Complex Visibility: The complex visibility, V, can be defined from the two independent correlator outputs, R_C and R_S (Taylor et al., 1998),

$$V = R_C - iR_S = Ae^{-i\phi} \tag{2.6}$$

where amplitude, $A = \sqrt{R_C^2 + R_S^2}$ and phase, $\phi = tan^{-1}\left(\frac{R_S}{R_C}\right)$. This leads to a relationship between source brightness and response of the interferometer,

$$V_\nu(\mathbf{b}) = R_C - iR_S = \int\int I_\nu(\mathbf{s}) e^{-2\pi i\nu \frac{\mathbf{b}\cdot\mathbf{s}}{c}} d\Omega \tag{2.7}$$

which is a unique function of source brightness. A key characteristic of Equation 2.7 is that it represents a 2-D Fourier transform, which in turn allows source brightness, $I(\mathbf{s})$, to be recovered from complex visibility, $V(\mathbf{b})$. The

[2]In a real interferometer containing a wide band system, an analog or digital device will perform the phase shift through a Hilbert Transform.

interferometer will make several measurements of the complex visibility (each measurement contains an amplitude and phase), leading to a reasonable estimate of source brightness.

A Real Interferometer: Now with the basic definition of complex visibilities, I will relax some of the idealistic assumptions made above. Real interferometers will accept a range of frequencies rather than simply a monochromatic (single frequency) signal, thus we have to consider the response of the interferometer to a finite bandwidth.

The finite bandwidth response is found by integrating the fundamental response from above over a frequency bandwidth, $\Delta\nu$, centred at ν_0 (Taylor et al., 1998),

$$V = \int \left(\frac{1}{\Delta\nu} \int_{\nu_0 - \frac{\Delta\nu}{2}}^{\nu_0 + \frac{\Delta\nu}{2}} I(\mathbf{s}, \nu) G_1(\nu) G_2^*(\nu) e^{-2\pi i \nu \tau_g} d\nu \right) d\Omega \tag{2.8}$$

Where $G(\nu)$ represents the signal response (i.e., amplitude and phase variation of the signal with respect to frequency). If the intensity of the source does not vary over the bandwidth, and the $G(\nu)$ functions for each antenna are square and identical, Equation 2.8 can be simplified to,

$$V = \int \int I_\nu(\mathbf{s}) sinc(\tau_g \Delta\nu) e^{-2\pi i \nu_0 \tau_g} d\Omega \tag{2.9}$$

Where the sinc function works to attenuate the fringe function from the correlator. Thus incorporating a finite bandwidth results in strong attenuation of the source visibilities. A solution to this problem is to shift the fringe-attenuation function to the centre of the source by adding a further time delay, τ_0, in the signals, as seen in Figure 2.2 below. Continuously adjusting this time delay can additionally correct for the motion of the source across the sky (real interferometers are built on the surface of the earth, which is essentially a rotating platform).

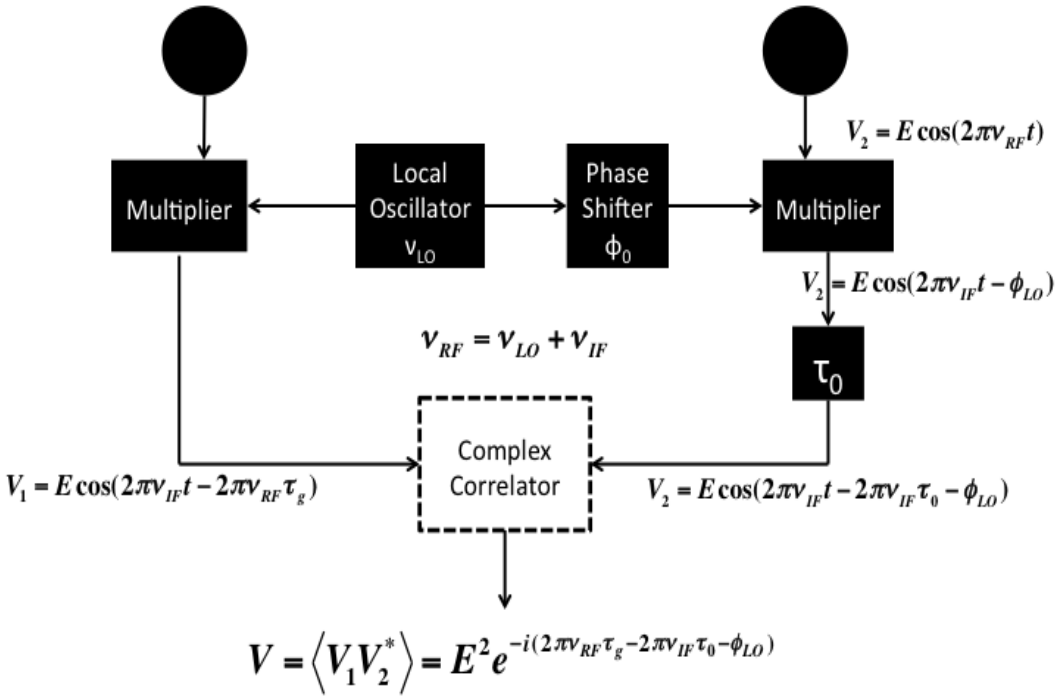

Figure 2.2: This schematic displays a simple two element RF interferometer incorporating time delay (Taylor et al., 1998).

Further, the internal electronics of the interferometer cannot work at the observing frequency as high frequency components are both expensive and perform more poorly than lower frequency components. Therefore, a process known as "down-conversion" is used to translate the radio frequency (RF) information from the source to a lower frequency band known as the intermediate frequency (IF). To do this the signal is multiplied in a given frequency range by an local oscillator signal (LO; a pure sinusoid at single frequency, $\nu_{\rm LO}$), which preserves the amplitude and phase of the signal (seen in Figure 2.3)[3].

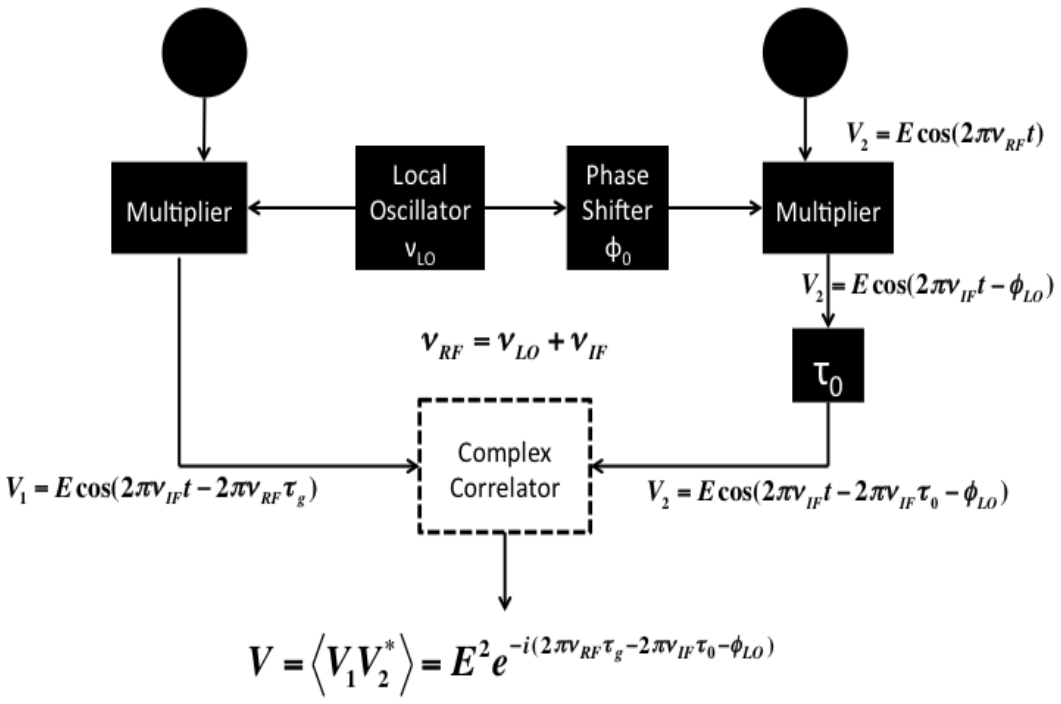

Figure 2.3: This schematic displays a simple two element interferometer incorporating time delay and frequency down-conversion (Taylor et al., 1998).

[3]Note that $\phi_{\rm LO} = 2\pi\nu_{\rm LO}\tau_0$ in order for the observed phase (after down-conversion) to match that seen in the RF interferometer. This must occur as the delay is added in the IF portion rather than at the RF as before in the simple interferometer).

There is a significant side effect of down-conversion. When the frequencies, ν_{RF} and ν_{LO} are combined in a mixer, combinations of the two frequencies are formed according to, $\nu_{\mathrm{RF}} = \nu_{\mathrm{LO}} \pm \nu_{\mathrm{IF}}$. Since the LO frequency is a single valued frequency and the RF and IF are ranges of frequencies (bands of width $\Delta\nu$), two frequency bands result from the down-conversion process (the upper and lower sidebands). The relationship between all noted frequencies is summarized in Figure 2.4 below.

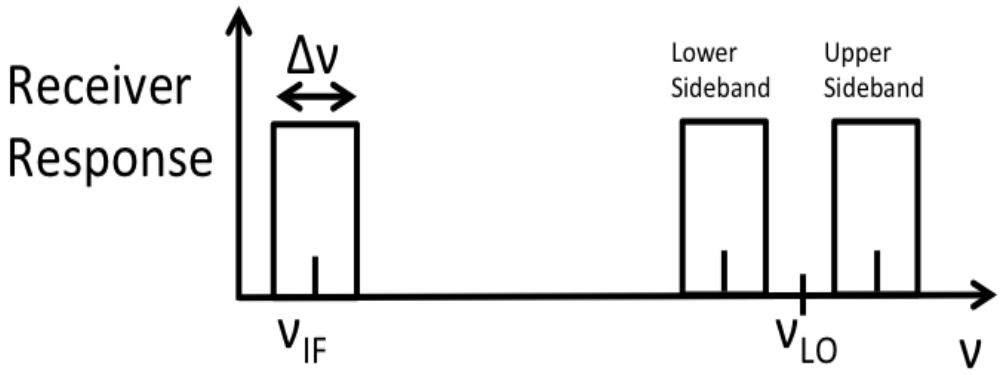

Figure 2.4: This schematic displays how RF (upper and lower sideband), IF and LO frequencies are related in a frequency down-conversion procedure (Taylor et al., 1998).

Above, the response and visibility functions were expressed in terms of two fundamental vectors, **b**, defining the separation between antennas (baseline) and **s**, defining direction to the source. We can now define a geometric coordinate system for our interferometer, as seen in Figure 2.5.

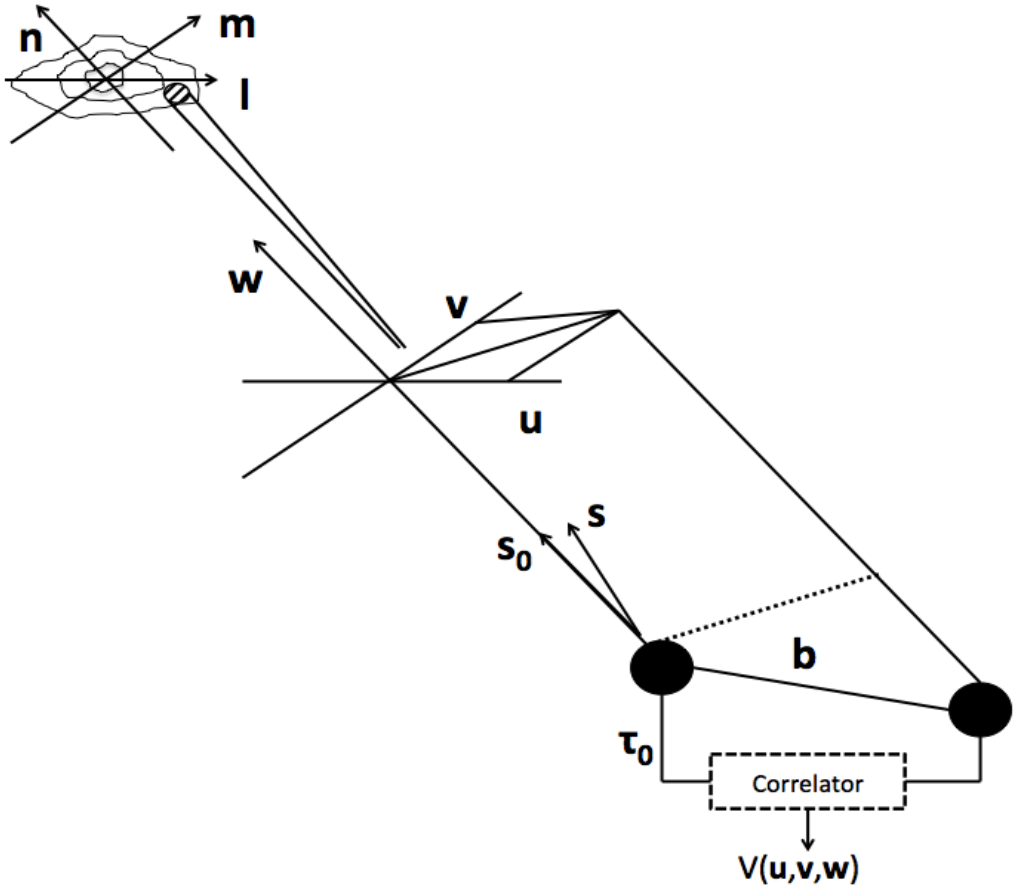

Figure 2.5: This schematic displays the coordinate system used to express interferometer baselines and source brightness distribution (Taylor et al., 1998).

The baseline vector, $\mathbf{b}$, has components, u, v and w (measured in wavelengths). Positions on the sky and thus the unit vector pointed towards the source, $\mathbf{s}$, are defined with components l, m and $n = \sqrt{1 - l^2 - m^2}$, which are direction cosines measured with respect to the u and v axes. In this coordinate system (Taylor et al., 1998),

$$\begin{aligned} \frac{\nu \mathbf{b} \cdot \mathbf{s}}{c} &= ul + vm + wn \qquad (2.10) \\ \frac{\nu \mathbf{b} \cdot \mathbf{s_0}}{c} &= w \\ d\Omega &= \frac{dldm}{n} = \frac{dldm}{\sqrt{1 - l^2 - m^2}} \qquad (2.11) \end{aligned}$$

and thus the visibility function in these coordinates becomes[4],

$$V(u, v) = \int \int I_\nu(l, m) e^{-2\pi i[ul+vm]} dldm \qquad (2.12)$$

One more addition is needed within this expression as the interferometer elements are not point probes but have a finite size. Thus, the elements have some sensitivity to the direction of arrival of the radiation. The primary beam, $A_\nu(l, m)$, describes this sensitivity as a function of direction and Equation 2.12 becomes,

$$V(u, v) = \int \int \mathcal{A}_\nu(l, m) I_\nu(l, m) e^{-2\pi i[ul+vm]} dldm \qquad (2.13)$$

Calibration: The observed visibilities sampled by the array (Equation 2.13) differ from the true visibilities due to instrumental (hardware and software, electronics, digital correlation) and environmental (atmospheric conditions, weather, RFI) properties. Calibration is the process used to recover the true

[4]The true 3-D expression is not a proper Fourier transform. However, if l and m are sufficiently small (i.e. small field imaging) the third term in the phase approaches zero, so the equation is now reduced to the 2D Fourier transform (as the dependence of the visibility on w is very small and can be omitted).

visibilities from the observed visibilities.

As the visibility is sampled at discrete times (t) for each antenna pair (i, j), it is helpful to write Equation 2.13 as (Taylor et al., 1998),

$$V_{i,j}(u,v) = \int\int \mathcal{A}_\nu(l,m) I_\nu(l,m) e^{-2\pi i[u_{i,j}(t)l + v_{i,j}(t)m]} dldm \tag{2.14}$$

Denoting the observed visibilities as $\widetilde{V}_{i,j}(t)$ and the true visibilities as $V_{i,j}(t)$, the basic calibration formula is as follows,

$$\widetilde{V}_{i,j}(t) = g_i(t) g_j^*(t) \mathcal{G}_{i,j}(t) V_{i,j}(t) + \varepsilon_{i,j}(t) + \epsilon_{i,j}(t) \tag{2.15}$$

where $g_i(t)$ represents factorable antenna based complex gains, $\mathcal{G}_{i,j}(t)$ represents baseline based non-factorable complex gain, $\varepsilon_{i,j}(t)$ represents baseline based additive complex offset and $\epsilon_{i,j}(t)$ represents stochastic complex (thermal) noise. The baseline based terms, $\varepsilon_{i,j}(t)$ and $\mathcal{G}_{i,j}(t)$, can generally be reduced with proper instrument design and can be considered negligible, reducing the equation to,

$$\widetilde{V}_{i,j}(t) = g_i(t) g_j^*(t) V_{i,j}(t) + \epsilon_{i,j}(t) \tag{2.16}$$

The antenna based complex gains can be separated into antenna based amplitude, $a_i(t)$, and phase, $\phi_i(t)$, corrections,

$$g_i(t) g_j^*(t) = a_i(t) a_j(t) e^{i(\phi_i(t) - \phi_j(t))} \tag{2.17}$$

To utilize this calibration equation, known calibrator sources are observed in the sky intermittently with the target source. These calibrators are ideally isolated, small diameter radio sources with high flux densities that are constant over the timescale of the observation. In addition, the calibrators should have accurate measured positions on the sky and simple spectra (i.e quasars, planets). Therefore, the true visibilities are known in these sources and by observing them (measuring observed visibilities) we can solve for the complex

gains, and then apply these solutions to correct our target source data.

Solving this calibration equation involves determining the gain corrections that minimizes $\mathcal{S}_K$ for each timestamp, t_k;

$$\mathcal{S}_k = \sum_k \sum_{i,j}^{i \neq j} w_{i,j} |g_i(t_k) g_j^*(t_k) \widetilde{V}_{i,j}(t_k) - M_{i,j}(t_k)|^2 \tag{2.18}$$

Where $w_{i,j}$ represents data weights, and $M_{i,j}(t_k)$ represents the calibrator model visibilities (or Fourier transform of model image).

Complex gains can also be a function of frequency in addition to a function of time. Compensating for a change of gain with frequency is known as bandpass calibration. Once again we must solve the calibration equation,

$$\widetilde{V}_{i,j}(\nu_k) = g_i(\nu_k) g_j^*(\nu_k) V_{i,j}(\nu_k) + \epsilon_{i,j}(\nu_k) \tag{2.19}$$

where k represents the individual frequency channels. The frequency dependent antenna based gains can be written in terms of amplitude and phase corrections similar to the time dependent gain solutions described above. To solve this equation we must once again observe a strong calibrator source, but this time it need not be a point source, only it must have a flat spectrum. As this bandpass gain function is not a strong function of time (just frequency) a bandpass calibrator can be observed less frequently than a gain calibrator.

Imaging and Deconvolution: The sky brightness can be calculated through taking the 2D Fourier transform[5] of the complex visibilities (Equation 2.13) (Taylor et al., 1998),

$$\mathcal{A}(l,m) I(l,m) = \int \int V(u,v) e^{2\pi i [ul + vm]} dl dm \tag{2.20}$$

[5] $V(u,v) \xrightarrow{\mathcal{F}} \mathcal{A}(l,m) I(l,m))$

where the modified sky brightness, $T(l,m) = \mathcal{A}(l,m)I(l,m)$ [6].

Each visibility, $V(u,v)$ [7] measured contains information about $T(l,m)$ everywhere. Thus, we want to sample $V(u,v)$ at enough (u,v) points to fill in the u-v plane as completely as possible[8]. Since the visibilities cannot be sampled everywhere in one observation, in practice we can introduce a sampling function, $S(u,v)$, that samples the Fourier domain at discrete points and is zero where no data has been taken. The Fourier transformed sampled visibility function[9] can be represented as[10],

$$T^D(l,m) = T(l,m) \star s(l,m) \tag{2.21}$$

where $s(l,m) \xrightarrow{\mathcal{F}} S(u,v)$ is the Fourier transform of the sampling pattern (i.e., point spread function). Therefore, the Fourier transform of the sampled visibilities (known as the dirty image) yields the true sky brightness (known as the true image) convolved with the point spread function (known as the dirty beam)[11].

However, it is difficult to work with the dirty image as it was formed from the observed sampled visibilities, which both incompletely sample the u-v plane

[6]The antenna beam, $\mathcal{A}(l,m)$ modifies the sky brightness distribution, and the true distribution, $I(l,m)$ can be recovered through division by $\mathcal{A}(l,m)$ in the image plane.

[7]Note that since sky brightness is a real function and $V(u,v)$ is Hermitian ($V(-u,-v) = V^*(u,v)$), one measurement actually results in two visibilities, $V(u,v)$ and $V(-u,-v)$.

[8]Since larger baselines sample smaller scale source structure and smaller baselines sample larger scale structure, missing u-v coverage can lead to missing information relating to the source.

[9]$V(u,v)S(u,v) \xrightarrow{\mathcal{F}} T^D(l,m)$

[10]The $\star$ represents the convolution operator. This relation is obtained through applying the convolution theorem of Fourier transforms.

[11]To use the Fast Fourier Transform (FFT) algorithm, which is much simpler and quicker than a simple Fourier summation you need data on a regularly spaced grid. Since we do not have this, the solution is to use a "gridding method" and resample $V(u,v)$ for the FFT according to, $V^G(u,v) = V(u,v)S(u,v) \star G(u,v) \xrightarrow{\mathcal{F}} T^D(l,m)g(l,m)$. In addition, depending on the science goal, a visibility weighting can be applied to the data when imaging to emphasize high sensitivity, high resolution or low side-lobes. Through introducing a weighing function we modify the sampling function $S'(u,v) \rightarrow S(u,v)W(u,v)$ and thus change the dirty beam $s(l,m)$ shape.

and are noisy. Therefore, we must deconvolve $s(l,m)$ from $T^D(l,m)$ to determine a model of the modified sky brightness, $T(l,m)$, in a process known as deconvolution.

The deconvolution process does not have a unique solution and as a consequence, there are an infinite number of $T(l,m)$ solutions that can be produced with the sampled visibilities (infinite number of images from the same visibilities). This occurs because we have incomplete (u,v) coverage, and to produce an estimate of $T(l,m)$, we need to fill in the unsampled parts of the u-v plane with "invisible distributions". Therefore making an image through deconvolution uses non-linear techniques to interpolate samples of $V(u,v)$ into un-sampled regions of the u-v plane. This process essentially chooses plausible invisible distributions to be merged with the "principal solution", resulting in a model $T(l,m)$ compatible with the data. To pick the "invisible distributions", *a priori* assumptions about the nature of $T(l,m)$ must be made.

The *clean* algorithm, originally developed by Hogbom (Hogbom, 1974)[12], is the predominant deconvolution algorithm in radio astronomy, in which the *a priori* assumption is that $T(l,m)$ is a collection of point sources. In this algorithm, an iterative approach is applied to find positions and strengths of these point sources,

1. The strength and position of the brightest (largest absolute intensity) peak in the image is found.

2. The peak strength multiplied by the dirty beam and a damping factor is subtracted from the dirty image.

3. The magnitude and position of the point component is recorded in a source model.

[12]The Clark Algorithm (Clark, 1980) is implemented in the *clean* task in CASA, which is the software used to reduce the SMA data in this thesis. This algorithm involves Fast Fourier Transforms (FFTs) and two cycles, major and minor. The Clark algorithm is used as it is more efficient then the Hogbom algorithm.

4. Repeat steps 1–3 until the largest remaining peak is below a user specified level.

5. The remainder of the dirty image after subtraction is known as the residuals.

6. The final deconvolved image (estimate of $T(l, m)$) consists of the source model of the accumulated point components convolved with the clean beam (an elliptical Gaussian fitted to central lobe of the dirty beam), and the residuals added back.

Self-Calibration: Calibration using external calibrators is imperfect and sometimes can not completely correct errors in the target source visablities, as calibrators can not be observed simultaneously with the target and they are not in the exact same position in the sky as the target. Self-calibration is an iterative process in which a target is essentially used to calibrate itself by producing a model (through *clean*) of the sky intensity distribution[13]. This model is used in the calibration equation (as $M_{i,j}(t_k)$) to determine gain corrections. Self-calibration is not just a circular trick but rather a method like *clean* in which we interpret visibility data by introducing plausible assumptions about source structure. Multiple rounds of self-calibration can be interspersed with imaging to calibrate the data. The main difference between self-calibration and normal calibration is the timescales over which the data is averaged before solving for a gain solution (Brogan, 2014).

2.1.2 Single Dish Telescopes

A single dish telescope operates on the same basic physics of an interferometer. Thus, a single dish can be visualized as a zero-spacing interferometer (base-

[13]The Fourier transform of this sky intensity distribution, when corrected with complex gain factors, reproduces the observed visibilities within the noise level.

line $\mathbf{b} = 0$), in which the response is equivalent to the total power received (Stanimirovic et al., 2002),

$$R \sim P_{\text{tot}}(\nu) = \frac{1}{2} A_e \int \int I_\nu(\mathbf{s}) P_n(\mathbf{s}) d\Omega \tag{2.22}$$

where $P_n(\mathbf{s})$ is the normalized response pattern of the antenna (sensitivity of antenna as a function of the direction of received radiation) and A_e is the effective collecting area of the antenna. Once again we observe at a range (bandwidth) of frequencies rather than at a single monochromatic frequency. Thus the total received power in a finite bandwidth, $\Delta\nu$, is represented by,

$$P_{\text{rec}} = \int_{-\frac{\Delta\nu}{2}}^{\frac{\Delta\nu}{2}} P_{\text{tot}}(\nu) d\nu \tag{2.23}$$

A single dish can detect a source signal by discerning small changes in this received power and separating the real astronomical signal from the noise.

The antenna temperature, T_A, is defined as the temperature at which a resistor (in place of the antenna) has the power, P_{rec} available at its terminals,

$$T_A = \frac{1}{\Omega_A} \int \int T(\mathbf{s}) P_n(\mathbf{s}) d\Omega \tag{2.24}$$

where $\Omega_A = \frac{\lambda^2}{A_e}$ represents the antenna beam solid angle and $T(\mathbf{s})$ represents the brightness temperature (or equivalent temperature of a blackbody for the given source brightness).

The presence of an astronomical source produces an antenna temperature, T_A, but additive noise power, which is dependent on the system noise temperature, T_{sys}, contaminates the signal.

$$T_{\text{sys}} = T_{\text{sky}} + T_{\text{atm}} + T_{\text{scat}} + T_{\text{rec}} \tag{2.25}$$

where T_{sky} is the background sky temperature, T_{atm} is the emission from earths

atmosphere, $T_{\rm scat}$ is the radiation scatter or spillover in different antenna elements and $T_{\rm rec}$ is the noise from the amplifier.

To find a source signal under the noise, instead of cross-correlating signals from many antennas like an interferometer, a single dish auto-correlates (correlate signal with itself) the signal received. Where the output voltage of the integrator (similar to the correlator in an interferometer but it averages signals only) in the antenna is proportional to the sum of the input powers of source signal, $\langle v_A(t)\rangle$, and noise, $\langle v_n(t)\rangle$. Thus the signal to noise ratio at the output of the integrator is,

$$\frac{S}{N} = \frac{\langle v_A(t)\rangle}{\langle v_n(t)\rangle} = \frac{T_A}{T_{\rm sys}} \tag{2.26}$$

However, the ability of the antenna to detect the average source signal in the presence of noise is not dependent on the mean of the noise but rather its rms fluctuation or standard deviation (σ_n). This leads to the signal to rms noise ratio, known as the Radiometer equation,

$$\frac{S}{N_{\rm rms}} = \frac{\langle v_A(t)\rangle}{\sigma_n} = \frac{T_A}{T_{\rm sys}}\Delta\tau\Delta\nu \tag{2.27}$$

where τ represents integration time and $\Delta\nu$ integrated bandwidth. A standard limit for detectability is $\frac{S}{N_{rms}} \geq 5$ (Stanimirovic et al., 2002).

The fundamental difference between single dish antennas and synthesis arrays is the range of spatial frequencies to which the instrument is sensitive. A single dish collects the flux within its response pattern and is able to probe emission on larger scales that will be resolved out by an interferometer. The range of spatial frequencies observed in a single dish is determined by the size of the antenna while for an interferometer the size of the baseline is the limiting parameter. Thus, many different observations[14], such as the observations in this thesis can be accomplished with both single dish and synthesis arrays.

[14]This statement only holds for point source type objects, not extended objects.

Receivers: Single dish telescopes operating at short mm/sub-mm wavelengths often use incoherent detectors[15], known as bolometers, as they have high continuum sensitivity and a flat spectral response over large bandwidths. A bolometer is simply a very sensitive thermometer or total power detector. This device essentially identifies changes in heat input from its surroundings and converts this to a measurable quantity such as voltage/current (Stanimirovic et al., 2002).

A bolometer has three main components; a thermometer, an absorber and a heat sink kept at a fixed temperature (see Figure 2.6). Incoming radiation energy is converted to heat in the absorber, which in turn causes a rise in temperature proportional to the incoming energy ($\Delta T = T - T_0 = \frac{E}{C}$). This temperature rise continues until the power flowing into the absorber is equal to power flowing into the heat sink (i.e., the heat sink acts to cool the device). The temperature change can be measured, and thus provides information about the source being observed. In a classical bolometer the detector is placed in a bias circuit (with resistance, R and voltage, V), which generates a constant current through the bolometer. If the bias power ($P_b = V_b I_b$) is constant, the incoming signal causes a rise in temperature, leading to a change in resistance and thus a change in voltage across the bolometer, which is measured. Materials are chosen so that a small change in temperature yields a large change in resistivity.

[15] An incoherent detector only measures intensity and does not preserve the phase information of the incoming radiation.

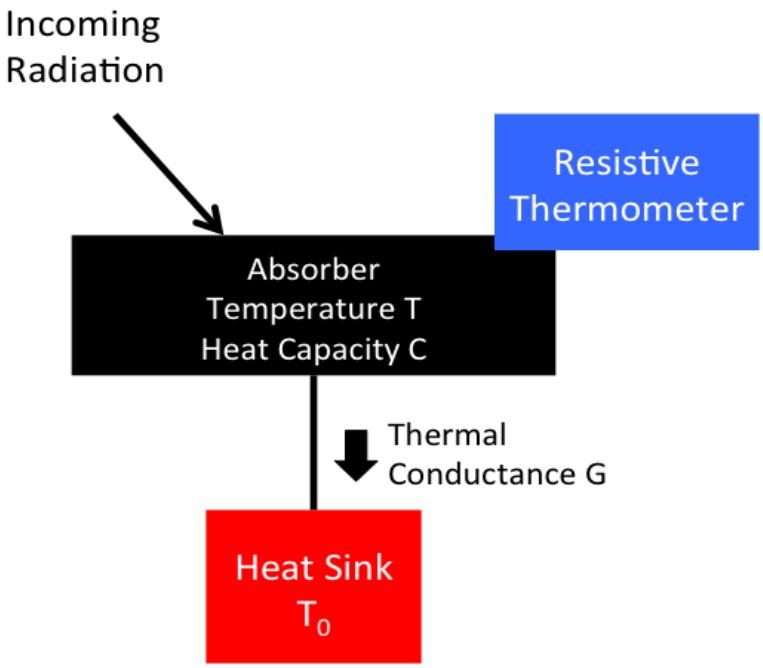

Figure 2.6: This schematic displays the main components of a simple bolometer. Figure adapted from Taylor et al. (1998).

Bolometers are useful for making maps of the sky, where a single pixel bolometer can accomplish this by scanning across the sky. However, as the sky can be quite variable at these frequencies, a better method is to use a bolometric array to image the sky, in which the array is shifted around between exposures to calibrate away non-uniformities in the efficiency of the bolometers. The JCMT uses a Superconducting Transition Edge Sensor (TES) bolometric array. Superconductors are beneficial as they have a strong dependence of resistivity with temperature in the transition region between superconducting and normal states. Thus in a TES, a small change in temperature yields a large change in resistivity. The superconducting film is held at a constant voltage so that a change in resistance results in a change in current through the film. This change in current is measured with a SQUID (superconducting quantum interference device). The SCUBA-2 detector on the JCMT consists of 2 separate focal planes (at 450μm and 850μm), each with 4 bolometric sub-arrays (*a*, *b*, *c*, and *d*), which operate simultaneously (Holland et al., 2013).

Single Dish Calibration: Similar to interferometry the goal of single dish calibration is to take the instrument response (power), and convert it to source flux. Single dish calibration typically involves two steps. As the background signal will dominate the weak source signal, it must be subtracted from the data. The background can have contributions from the sky, atmosphere, ground, instrument and electronics. Following this background subtraction, the data is still in raw voltage/current units, and thus a flux calibration must also be applied to yield a meaningful source flux. This flux calibration can be done by scaling against a source of known flux.

Calibration techniques used are dependent on the instrument and atmospheric conditions of the site. The SCUBA-2 detector on the JCMT operates in a scan observing mode, where the telescope continuously moves in a particular pattern. The scan pattern and speed is designed to best distinguish the fixed

source signal from the slowly varying signals due to extinction and atmospheric noise. The data analyzed in this thesis was obtained from observations in the DAISY scan mode (seen in Figure 2.7), which is ideal for point-like sources as it maximizes exposure time on the centre of the image (where the target is placed). The DAISY scan consists of a spiral type pattern at a constant velocity (Chapin et al., 2013; Dempsey et al., 2012; Holland et al., 2013).

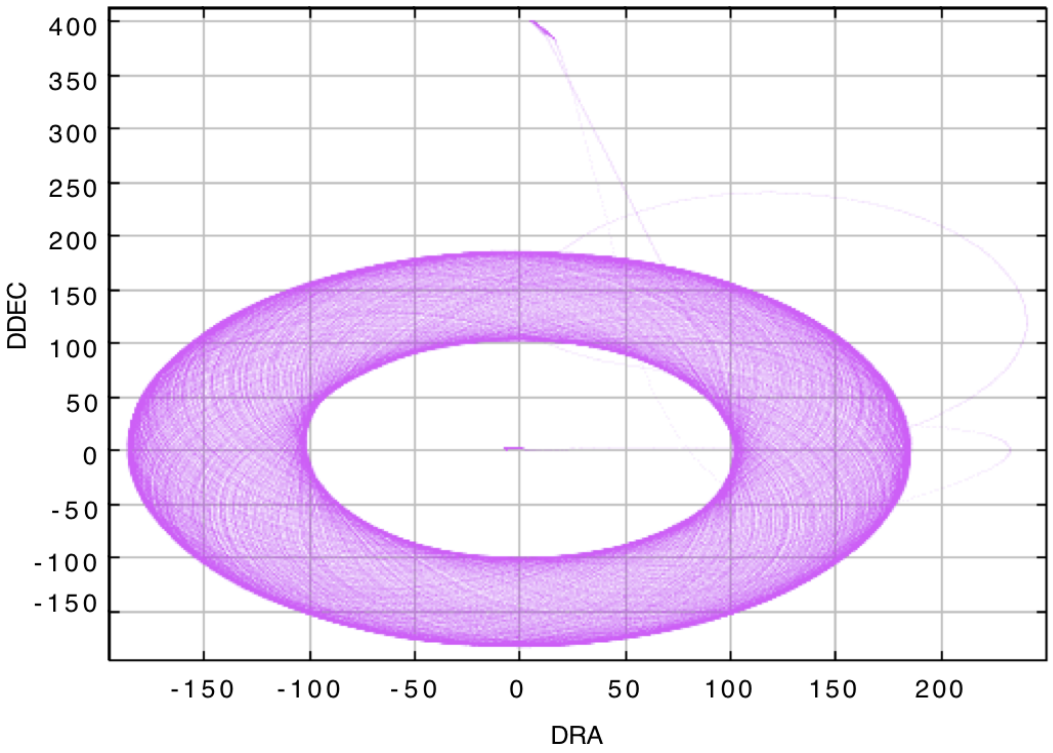

Figure 2.7: This plot displays multiple rotations of the DAISY scan pattern for the a sub-array during one of the observations of our science target, plotted in offsets of right ascension and declination coordinates in units of degrees.

To subtract the background signal in SCUBA-2 data, an iterative process is used in which individual contributions of the total bolometer signal are modelled and then subtracted in order of decreasing magnitude until the only signal left is the source and astronomical noise. The signal from each bolometer can be expressed as,

$$\mathbf{b}_i(t) = f_i[\mathbf{e}_i(t)\mathbf{a}_i(t) + \mathbf{n}_i(t)] \tag{2.28}$$

where, $\mathbf{a}_i$ represents the time-varying signal produced by scanning the telescope across the source, $\mathbf{e}_i$ represents time varying extinction[16], and noise $\mathbf{n}_i = \mathbf{n}_i^w(t) + g_i\mathbf{n}^c(t) + \mathbf{n}_i^f(t)$ which consists of uncorrelated white noise, a correlated signal common to all bolometers (g is scale factor for each bolometer) and (predominantly low frequency) noise that is in excess of the white noise level and is uncorrelated between bolometers, respectively.

This process works to isolate source signal plus white noise ($\mathbf{a}_i(t)+\mathbf{n}_i^w(t)$). A map is then produced by resampling this remaining time series bolometric data onto a predefined map grid. The brightness in each pixel is estimated by the weighted average of bolometer data samples that land within that pixel. This map is cleaned, similar to what is done in interferometry, in order to estimate a source model. This source model is projected back onto the time domain (essentially the signal that would be produced in each bolometer by the signal represented in the map) and subtracted leaving only white noise (residual). The individual models that are subtracted from the bolometer signal are outlined in the Table 2.1 below and examples of the signals from these models can be seen in Figure 2.8.

As this is an iterative process, there are different choices of convergence criteria. The parameters governing convergence can either work to access the noise level in the map (maptol, probes normalized change in map pixels) or in the time series (chitol, probes change in reduced chi-squared, essentially the rms of the residual or the time series data with model components removed).

The output data from this process is in current units of picowatts (pW), and thus needs to be converted to flux units of Janskys (Jy). Similar to flux calibration in an interferometer, calibrator sources with known flux properties are observed in order to find a flux conversion scale factor (FCF), which is applied to scale the source data to proper units.

[16]Extinction is a function of elevation and atmosphere conditions. This signal is calculated from the Water Vapour Monitor (WVM) on the JCMT, which monitors the sky opacity.

Table 2.1: Individual Model Components in a Bolometer Signal

Model	**Description**	**Parameter**
Common Mode Signal (COM)	The signal common to all bolometers, dominant contribution is sky/atmospheric noise	$\mathbf{n}^c(t)$
Gain (GAI)	Common mode signal scaled to each bolometer	g_i
Extinction (EXT)	Extinction correction determined from a time varying scale factor derived from the WVM	$\mathbf{e}_i(t)$
Fourier Transform Filter(FLT)	Applies a filter to remove low frequency noise that COM did not catch	$\mathbf{n}_i^f(t)$
Astronomical Signal (AST)	Estimate of source signal	$\mathbf{a}_i(t)$
Noise Estimate (NOI)	Only calculated in first iteration; used to weight bolometers in following iterations	$\mathbf{n}_i(t)$

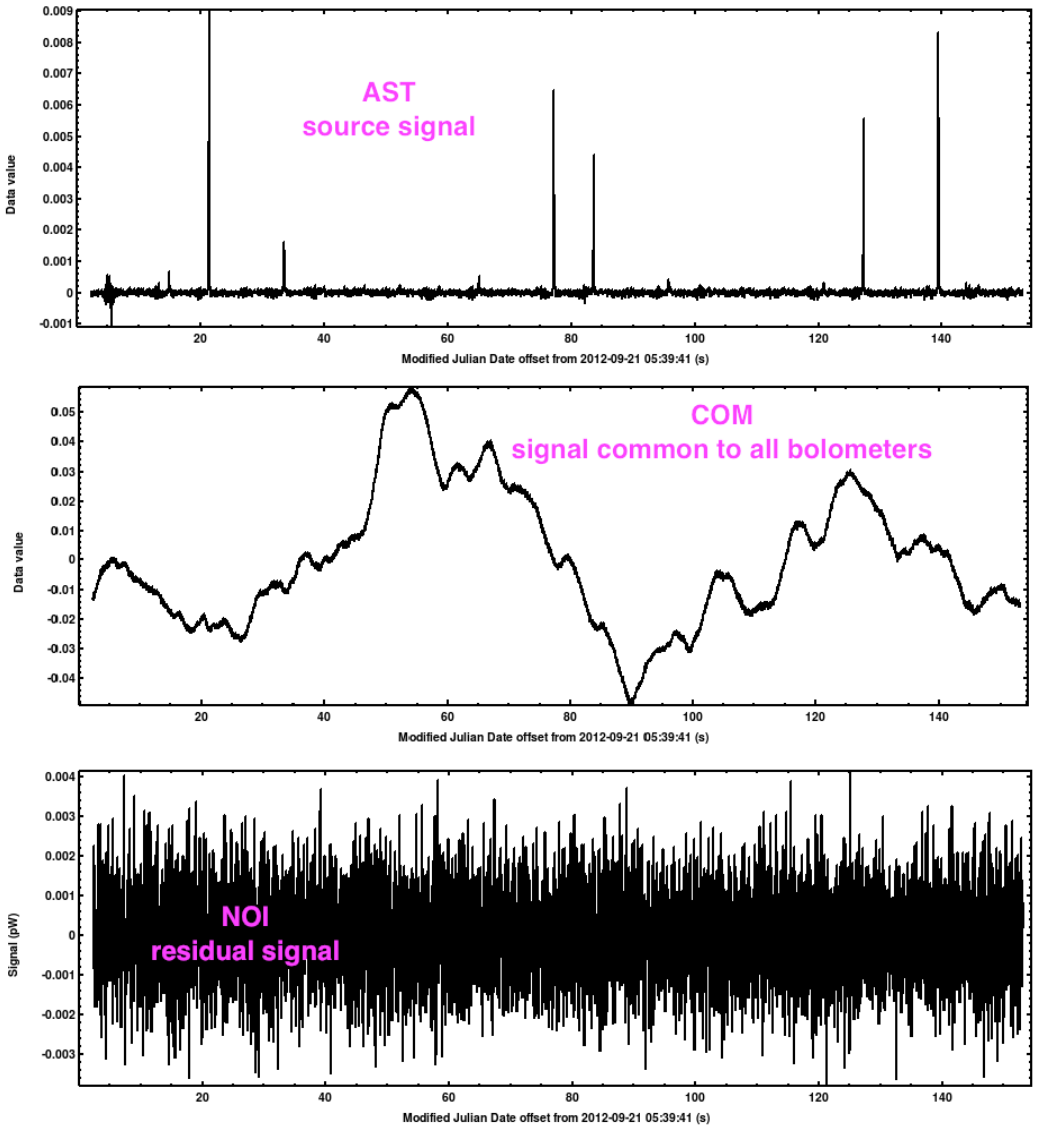

Figure 2.8: This schematic displays an example of the AST (top), COM (middle) and NOI (bottom) time series model component signals from the DIMM on one observation with the a sub-array of the calibrator CRL2688. The COM model is a signal common to all bolometers in the array. The NOI model represents the residual signal left over after all model components have been subtracted. Notice how NOI simply looks like white noise, as expected. The AST model represents the source signal, where spikes indicate when the array passed over the source.

2.1.3 Specifics of Observing at mm/sub-mm Frequencies

The main difference between observing at radio versus mm/sub-mm frequencies is that the mm/sub-mm suffers from more adverse effects of the troposphere on the observed visibilities (amplitudes and phases) and a more limited availability of absolute flux calibrators. Below I discuss the effects introduced due to the troposphere and methods available to correct them.

The Troposphere: The Troposphere is the lowest layer of the atmosphere extending up to elevations of ~ 17 km. In this atmospheric layer, temperature decreases with increasing altitude. Therefore convection will be significant and clouds will form. The composition of this layer consists of "dry" constituents (i.e. O_2, O_3, CO_2), H_2O (mostly in the form of water vapour), and "hydrosols" (water droplets in clouds and fog). While all of these components contribute to the optical depth in the troposphere, the water vapour (expressed in terms of precipitable water vapour, PWV, which is the depth of water vapour if it was converted to a liquid phase) most significantly affects the opacity (see Figure 2.9) of the troposphere at mm/sub-mm frequencies (Brogan, 2014; Taylor et al., 1998).

Snells's Law indicates that as the refractive index of the atmosphere does not equal unity, an electromagnetic wave propagating through it experiences a phase offset. This phase change can be expressed in terms of the refractive index of air (n), distance travelled (D), and PWV (w),

$$\phi_e = \frac{2\pi}{\lambda} nD \approx \frac{2\pi}{\lambda} \frac{w}{T_{\rm atm}} \tag{2.29}$$

This refractive effect will in turn effectively change the expected position of the source and thus require adjustments to antenna pointing. In addition, time of arrival delays due to the troposphere (additions to a simple vacuum assumed in geometric delay calculations for an interferometer) must also be corrected. These mean phase errors are usually corrected in the online system

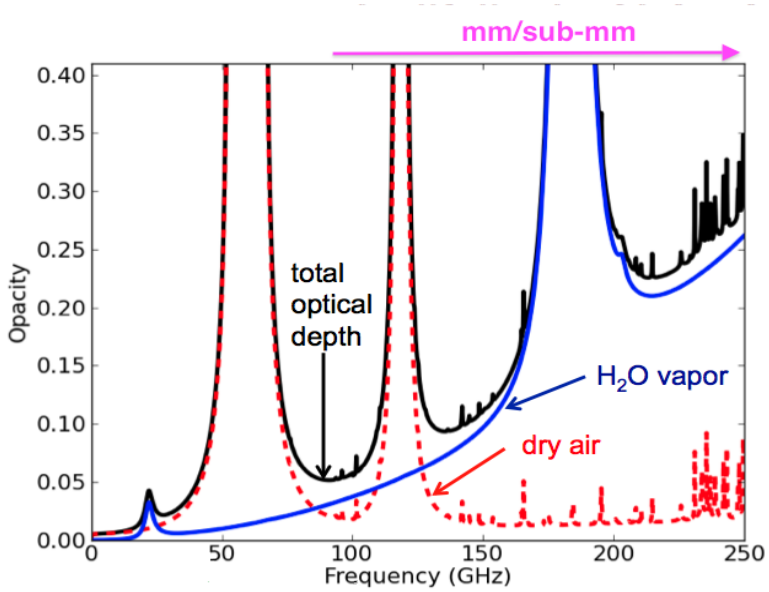

Figure 2.9: The optical depth as a function of frequency is shown for the VLA site and a PWV of 4 mm. It is clear that at mm/sub-mm frequencies (~ 90 GHz and above as indicated by magenta arrow on plot) water vapour is the key contributor to opacity. Figure adapted from Taylor et al. (1998) and Brogan (2014).

of the instrument. This is done by measuring atmospheric parameters (such as temperature and pressure) and modelling their profiles and relation to the refractive index throughout the atmosphere.

At mm/sub-mm frequencies, the atmosphere will emit thermally (under certain conditions and at certain frequencies when the atmosphere becomes optically thick it will emit like a blackbody) and can have a significant brightness temperature ($T_{\rm sky} = T_{\rm atm}(1 - e^{-\tau})$) due to increased opacity. This will contribute to the system noise temperature as follows,

$$T_{\rm noise} \approx T_{\rm rx} + T_{\rm atm}(1 - e^{-\tau}) \tag{2.30}$$

As the source signal is attenuated by the atmosphere ($S = T_{\rm source}e^{-\tau}$) the signal to noise ratio becomes,

$$\frac{S}{N} = \frac{T_{\rm source}}{T_{\rm noise}e^{\tau}} = \frac{T_{\rm source}}{T_{\rm sys}} \tag{2.31}$$

Therefore, it is clear that the sensitivity of the system will drop exponentially as opacity increases. This means that changes in atmospheric absorption can be corrected if $T_{\rm sys}$ is measured often[17].

In the troposphere, patches of air with different water vapour content (i.e. different refractive index) will affect the incoming electromagnetic wave differently. Variations in the amount of PWV lead to variations in path length and thus can cause phase fluctuations (see Figure 2.10), which progressively get worse at higher frequencies. The fluctuations grow as a function of increasing baseline according to,

$$\phi_{\rm rms} = \frac{Kb^{\alpha}}{\lambda} \tag{2.32}$$

where b is baseline length in km, α ranges from $\frac{1}{3}$ (thickness of the turbulent layer is small compared to maximum baseline) to $\frac{5}{6}$ (thickness of turbulent layer is large compared to maximum baseline), λ is wavelength in mm, and K is a constant specific to the site. These fluctuations can cause de-correlation (loss of sensitivity where observed visibility amplitude is reduced from the true value), poor "seeing" (poor phase stability limits spatial resolution analogous to how thermal fluctuations effect optical seeing), and anomalous refraction (phase gradients across the antenna can change the apparent position of source). To correct these effects, specialized methods are used, such as, fast switching (normal phase calibration but with cycle times short enough to reduce fluctuations[18]), radiometry (monitoring of phase by measuring fluctuations in $T_{\rm atm}$ and deriving PWV fluctuations, followed by conversion to phase corrections), self-calibration (using the source to calibrate itself), phase transfer (observing simultaneously at low/high frequencies and transferring scaled phase solutions from low to high frequencies) or paired array calibration (dividing the array into two separate arrays, while one observes the target and the other observes the calibrator).

[17] A "chopper wheel" method is typically invoked to measure system temperature. This process involves placing an ambient temperature load in front of the receiver, measuring resulting power, and comparing to the power when observing the sky alone.

[18] Cycle times on the order of seconds rather then minutes.

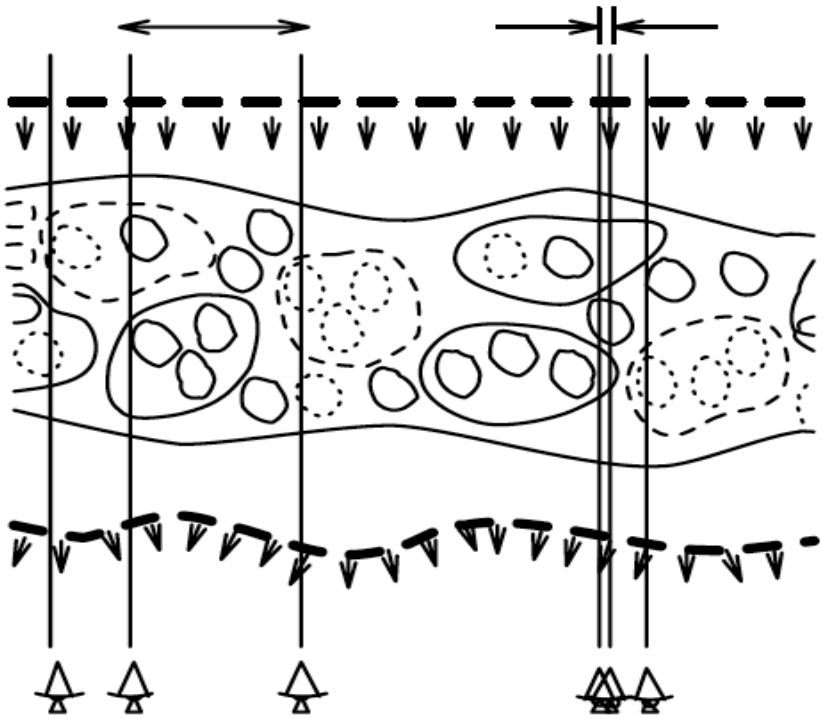

Figure 2.10: This schematic displays fluctuations in water vapour content in the troposphere at different scales. Solid lines indicate excesses and dotted lines indicate deficits. Arrows indicate the phases of the incoming electromagnetic wave before and after passing through the troposphere. For closely spaced antennas, larger scale fluctuations can be correlated, but small scale fluctuations are not correlated between antennas (Taylor et al., 1998).

Calibrator Sources: Flux calibrators used at radio frequencies are typically non-variable point sources such as quasars. However, no such sources are currently known at mm/sub-mm frequencies[19]. Therefore, planets are typically used as they are roughly blackbodies of known size and temperature. But as many planets are highly resolved with mm interferometers, an accurate model of the source is needed to calibrate with them accurately.

2.1.4 Instruments Used in this Thesis

The telescopes/instruments used to obtain the data being reduced and interpreted in this thesis and their key properties are outlined in Table 2.2 below.

Table 2.2: Telescope Properties

Telescope/ Instrument	**Location (Elevation)**	**Antenna Diameter**	**Number of Antenna(s)**	**Min–Max Baselines**
VLA	Socorro, NM (2124 m)	25 m	27	35 m − 36 km
SMA	Mauna Kea, HI (4092 m)	6 m	8	8 − 509 m
JCMT/SCUBA-2 Bolometer Array	Mauna Kea, HI (4092 m)	15 m	1	n/a

2.2 Reduction Processes

In the following Sections, I will outline the processes used to reduce the data analyzed in this thesis, including any problems encountered and how they were resolved.

[19]Quasars have an optically thin spectrum (steep or negative spectral index) and in turn are bright at radio frequencies but very faint at mm/sub-mm frequencies. Thus quasars cannot be used as flux calibrators at mm/sub-mm frequencies but are routinely used at radio frequencies.

2.2.1 SMA

SMA data were reduced using the Common Astronomy Software Applications (CASA) package. All observing runs with the SMA are summarized below in Table 2.3[20], while the calibrators[21] used in each run are summarized in Table 2.4.

Table 2.3: Observing Runs with SMA

Date	**Array Config.**	**ν (GHz)**	**$\Delta\nu$ (GHz)**	**Time on Source (hrs)**	**Pred. rms (mJy/beam)**	**PWV (τ)**
2012 Sep 20	Very Extended	230	4	~ 4.95	0.67	4mm (0.21)
2012 Sep 22	Very Extended	230	4	~ 4.62	0.67	4mm (0.21)
2012 Sep 25	Very Extended	230	4	~ 4.40	0.67	4mm (0.21)

Table 2.4: Calibrators for SMA

Telescope	**Date**	**Flux Calibrator**	**Bandpass Calibrator**	**Gain Calibrator**
SMA	2012 Sep 20	Neptune,3c84	1924–292	nrao530,1924–292
SMA	2012 Sep 22	Neptune	1924–292	nrao530,1924–292
SMA	2012 Sep 25	Neptune	1924–292	nrao530,1924–292

Currently, CASA is unable to handle SMA data in its original format. Therefore, the data must be converted into CASA MS format before it can be analyzed. In addition, CASA is unable to perform the $T_{\rm sys}$ correction (correcting for attenuation of the atmosphere) on SMA data. To remedy these problems, the SMA has created two scripts, *sma2casa.py* and *smaImportFix.py*, which perform the $T_{\rm sys}$ correction, ensure the data is properly weighted, convert each spectral chunk (spw) in each sideband to a FITS file, read each FITS file

[20]Integration times for all observations were 30 sec.

[21]The calibrators, nrao 530, 1924-292 and 3c84 are all quasars.

into a CASA measurement set (MS) and concatenate the individual MSs into a single MS per sideband.

Once the data were in CASA MS format, I inspected the visibility data using the *plotms* tool to look for major outliers and locate bad data that could be flagged with the *flagdata* tool. Plotting amplitude/phase vs. uv-distance, amplitude/phase vs. time, amplitude/phase vs. spw/frequency/channel while parsing through antennas/fields allowed me to examine the visibilities in detail and locate poor quality data for flagging. To determine a reference antenna for calibration, I plotted antenna positions with *plotxy*, looking for an antenna near the centre of the array. Further, plotting phase vs. time for all antennas paired with my choice of reference antenna was used to check the continuity of phase over time. Following inspection, I corrected for common problems in SMA data. Most notably, as SMA spw chunks overlap, I flagged 4 channels on each end of the spw chunks to aid in calibration. I then flagged the first integrations in each scan due to their propensity for low amplitudes (quack mode in *flagdata*), and removed a spike in amplitude seen in the scans of the calibrator, 1924-292, due to the pointing solution (ipointing data). In addition, a few low amplitude spw chunks on antenna 7, a spike in the $T_{\rm sys}$ correction of the target at elevations below 20 degrees, and a few high baselines on the flux calibrator, Neptune, were also flagged.

The data was collected in double bandwidth mode (single receiver, 4GHz bandwidth), where the 4GHz IF is sent to the correlator through 2 independent IF pathways. Therefore, the upper 2 GHz (spw s25-s48) can drift and show an offset in phase relative to the lower 2 GHz (spw s01-s24). When I checked for phase offsets between IFs I only saw these offsets in the 2012 Sep 25 data, on Antenna 8 in the middle of the observation and thus I calibrated IFs separately on this day. In addition, as SMA data contains a pseudo-continuum chunk with one channel (s00), I excluded that chunk when calibrating.

After flagging was complete, I performed bandpass calibration to remove

frequency-dependent amplitude and phase effects. However, before I began the bandpass calibration I removed major phase variations with time by carrying out a short-timescale phase solution (solution interval equivalent to the integration time) on the bandpass calibrator using the *gaincal* tool, and made sure to average spw together to achieve maximum sensitivity (increase S/N). I then performed the bandpass calibration solving for the amplitude and phase corrections needed for each channel, for each antenna using the *bandpass* tool. I further applied bandpass and initial phase calibration on the fly while solving for an initial amplitude solution over a longer solution interval to increase S/N. Now as SMA data often show residual baseline-based problems as a function of spw after bandpass calibration (high or low spw on certain baselines), I used *plotms* to look for such a problem. Fortunately, I did not see such problems in our data so no correction was needed. When I was confident with the solutions I applied the phase, amplitude, and bandpass solution to the bandpass calibrator using the *applycal* tool, as well as to all other calibrators.

Now that I have corrected frequency-dependent effects, I performed final gain and flux calibrations for all calibrators to correct time-dependent effects and set the absolute flux scale. I solved for two gain phase solutions. A shorter interval solution (integration time) which will be fed to the amplitude calibration later to avoid de-correlation of the amplitude, and a longer interval solution (scan time) which will be applied to the target (the scan time is a proper cadence to apply to the target as the target is visited every other scan). Unfortunately, I saw a clear phase offset between calibrators (nrao530 and 1924-292), therefore, I solved for an initial phase solution with nrao 530 first, then used 1924-292 to correct further problems using the *gaincal* tools ability to apply calibrations on the fly while solving for a further solution. Once I was confident with the phase solutions, I applied the short interval solution and bandpass on the fly while solving for amplitude solutions. I then proceeded to set the flux scale with *setjy* using Neptune as a reference, then bootstrapped

to set the absolute flux scale of other calibrators using the *fluxscale* tool. I double checked the bootstrap output with measured flux values for calibrators on the SMA website (they are consistent taking into account the variation that occurs). Finally, I applied bandpass, phase, and amplitude gain solutions to all calibrators and the target (*applycal*), then split off the target for further inspection (*split*), imaging (*clean*) and self-calibration (*gaincal*).

The *clean* task is used for imaging and deconvolution. Imaging parameters are summarized in Table 2.5 below[22].

Table 2.5: Imaging Parameters for SMA Data

Date	**Image Size (pixels)**	**Cell Size (arcsec)**	**Loop gain**	**Threshold (mJy)**	**Weighting**
2012 Sep 20	512	0.1	0.01	0	natural
2012 Sep 22	512	0.1	0.01	0	natural
2012 Sep 25	512	0.1	0.01	0	natural

As described above imaging and self-calibration can be performed in tandem. The standard procedure I used to perform these tasks is outlined below,

1. Run the *clean* task to make a dirty image and check that the target source is clearly detected.

2. Perform a conservative clean (number of iterations, $niter = 100 - 200$) to build an initial source model, with a clean box placed only around the source emission I trust is real.

3. Checked for sufficient S/N in the cleaned image (signal is peak value, noise is rms away from negative bowls and emission) to do a self-calibration[23].

[22]Natural weighting is used to maximize sensitivity. This increased sensitivity is at the expense of resolution, but since we are dealing with a point source resolution is not an issue.

[23]Sufficient S/N is achieved when the target can be detected in a solution interval (solint) less than the time for significant phase variations with only the baselines to a single antenna with a $\frac{S}{N_{\rm self}} > 3$; $\frac{S}{N_{\rm self}} = \frac{\rm peak}{\rm rms \times \sqrt{N-3} \times \sqrt{\frac{totaltime}{solint}}} > 3$. This works out to a $\frac{S}{N} \sim 15$ in a cleaned image with the SMA.

4. Determine a solution interval for a phase only self-calibration and calculated phase self-calibration solutions. The scan length can typically be used initially, but as the SMA has a small number of antennas and thus lower S/N, I needed a longer interval. Further, I made sure the solutions were only slowly varying with time (not noisy and you can reasonably track the phase) and that there were minimal failed solutions on each antenna.

5. Apply the phase self-calibration solutions and re-clean until the residuals become noise like. Although more emission can be incorporated into the clean box if it looks real, I saw no such extra emission in my images.

6. Compare the original cleaned image with the first phase self-calibration image to see if the S/N improves. If the S/N improved then I tried a shorter solution interval. I made sure not to apply previous phase solutions before solving for current solutions as this can build in errors.

7. Repeat steps 4–6 until I found the shortest interval where S/N is no longer increasing.

8. Apply the best phase solution and re-clean until the residuals became noise like.

9. Try an amplitude self-calibration. To do this I followed the same procedure as for phase self-calibration (steps 4–6) to find the best solution interval. However, as amplitude tends to vary more slowly than phase and is less constrained, the amplitude solution intervals need to be longer than those for phase self-calibration. I set mode=ap rather than just mode=a so I could test if the residual phase solutions were close to zero.

10. Apply the best phase and amplitude self-calibration solutions to the data. I then used *plotms* to check the corrected data for any outliers and to make certain the model matches the original data (flux has not decreased

significantly post self-calibration). If this was not the case I returned to the phase only solution.

11. Re-clean until the residuals became noise like and compared the final phase self-calibration and phase & amplitude self-calibration images to see if S/N improved. If the S/N did improve I finished with this solution, if it did not I returned to the phase only solution.

12. Fit an elliptical Gaussian using the *imfit* task to obtain total flux density of the source. (Note that difmap was also used to model fit the visibilities in the u-v plane rather than the image plane. All flux density values obtained from fitting in the u-v plane were consistent with those found from fitting in the image plane.)

The source was clearly detected on 2012 Sep 22 and 2012 Sep 25, but not on 2012 Sep 20 (see Figure 2.15 for images of the non-detections in this epoch), where only 5 antennas were present. Following the process above, a phase only self-calibration with a solution interval of 30 min was used to correct the data. There was not enough S/N to perform an accurate amplitude self-calibration. The final flux density values of the target source are seen in Table 2.6 below. The pre and post phase self-calibration images for all epochs and sidebands are seen in Figures 2.11, 2.12, 2.13, and 2.14.

Table 2.6: Flux Densities for SMA Data

Date	**Sideband**	**Flux Density (mJy)**
2012 Sep 20	LSB	...
2012 Sep 20	USB	...
2012 Sep 22	LSB	32.10±1.30
2012 Sep 22	USB	35.32±1.71
2012 Sep 25	LSB	35.11±1.11
2012 Sep 25	USB	37.83±1.52

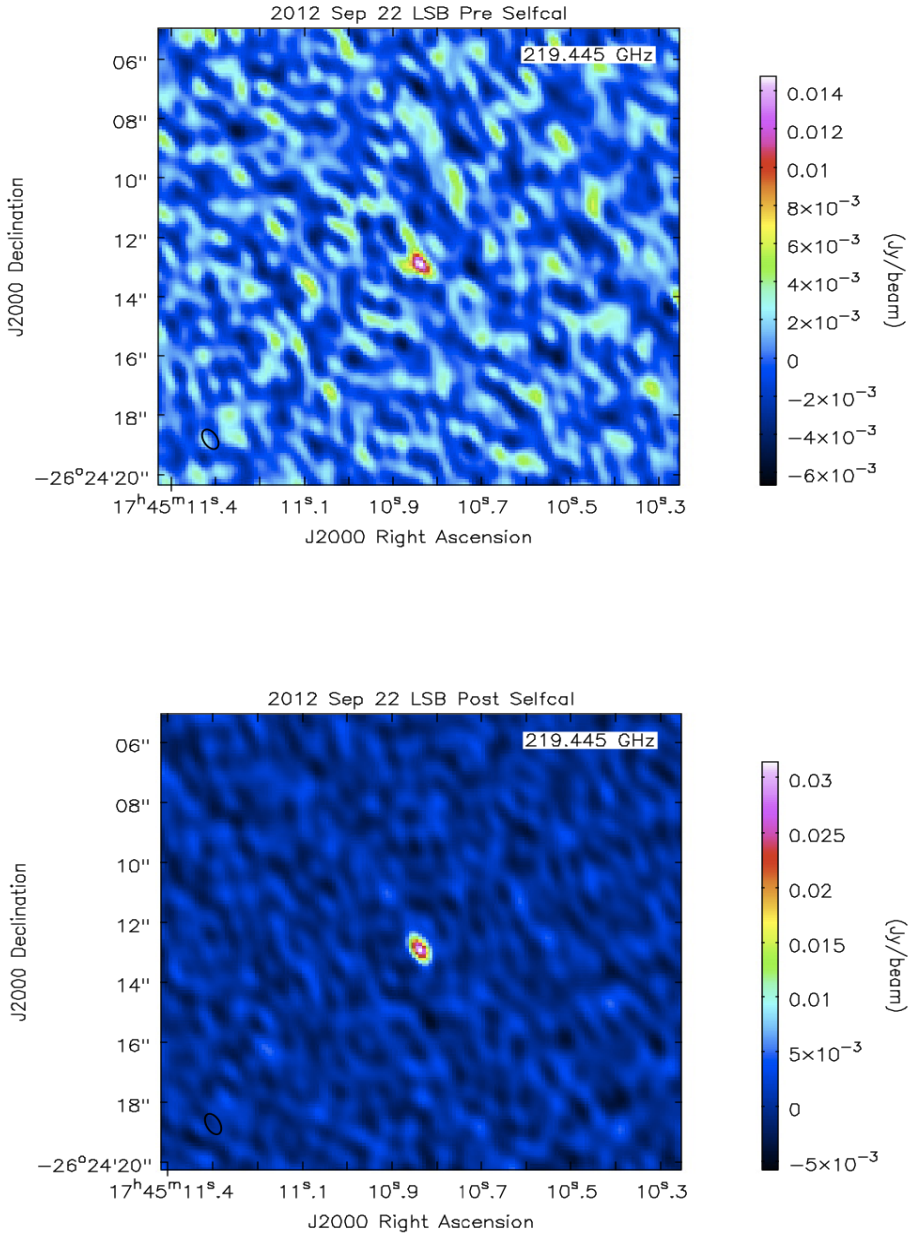

Figure 2.11: Images of Swift J1745–26 on 2012 Sep 22 in the lower sideband (219.445 GHz), both pre (top panel) and post (bottom panel) phase self-calibration. Colours correspond to the intensity scale seen on the right given in units of Jy/beam. The ellipse in the bottom left represents the FWHM of the clean beam. Residual phase calibration errors are evident in the pre self-calibration image. There is clearly a significant increase in S/N post self-calibration, as we have corrected for phase decorrelation that spread source flux throughout the image.

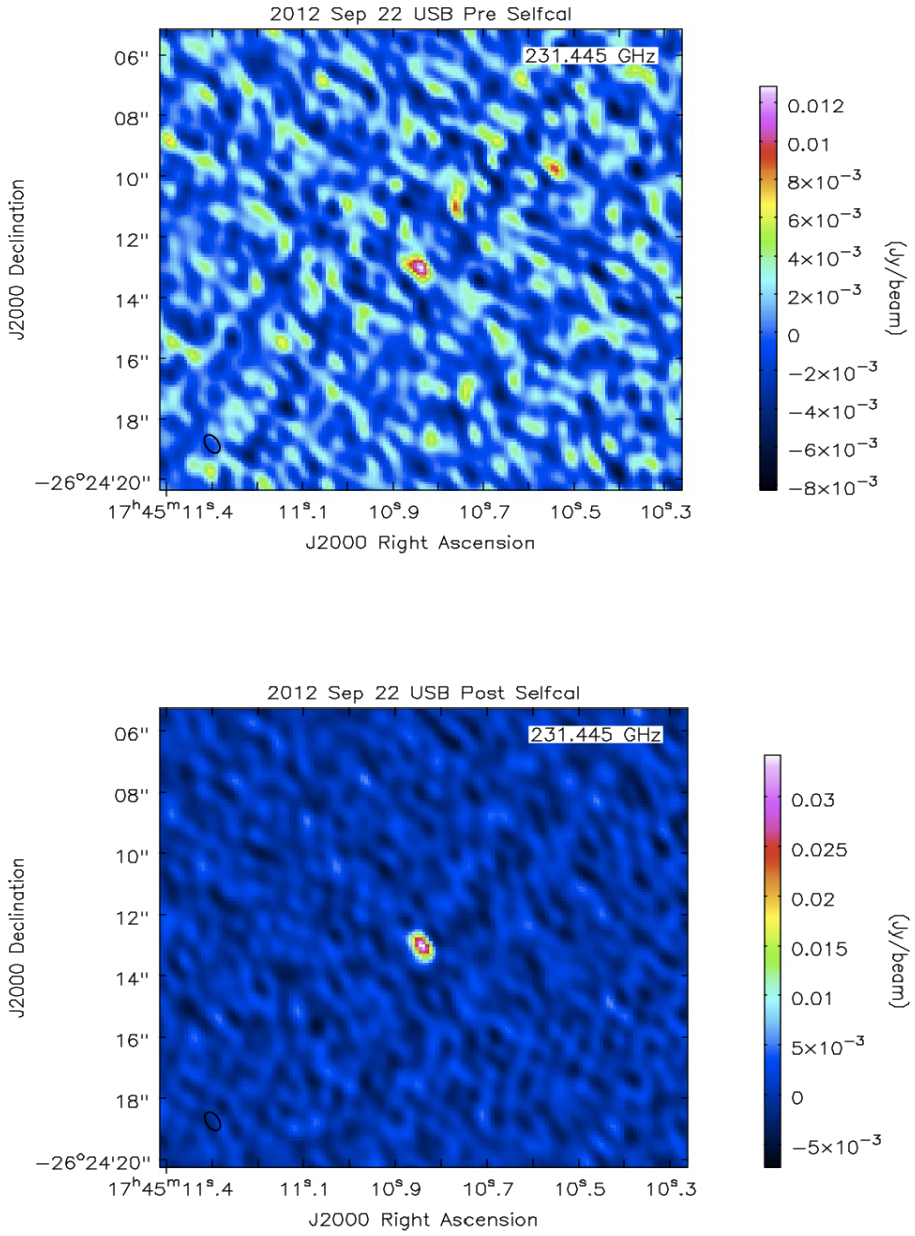

Figure 2.12: Images of Swift J1745–26 on 2012 Sep 22 in the upper sideband (231.445 GHz), both pre (top panel) and post (bottom panel) phase self-calibration. Colours correspond to the intensity scale seen on the right given in units of Jy/beam. The ellipse in the bottom left represents the FWHM of the clean beam. Residual phase calibration errors are evident in the pre self-calibration image. There is clearly a significant increase in S/N post self-calibration, as we have corrected for phase decorrelation that spread source flux throughout the image.

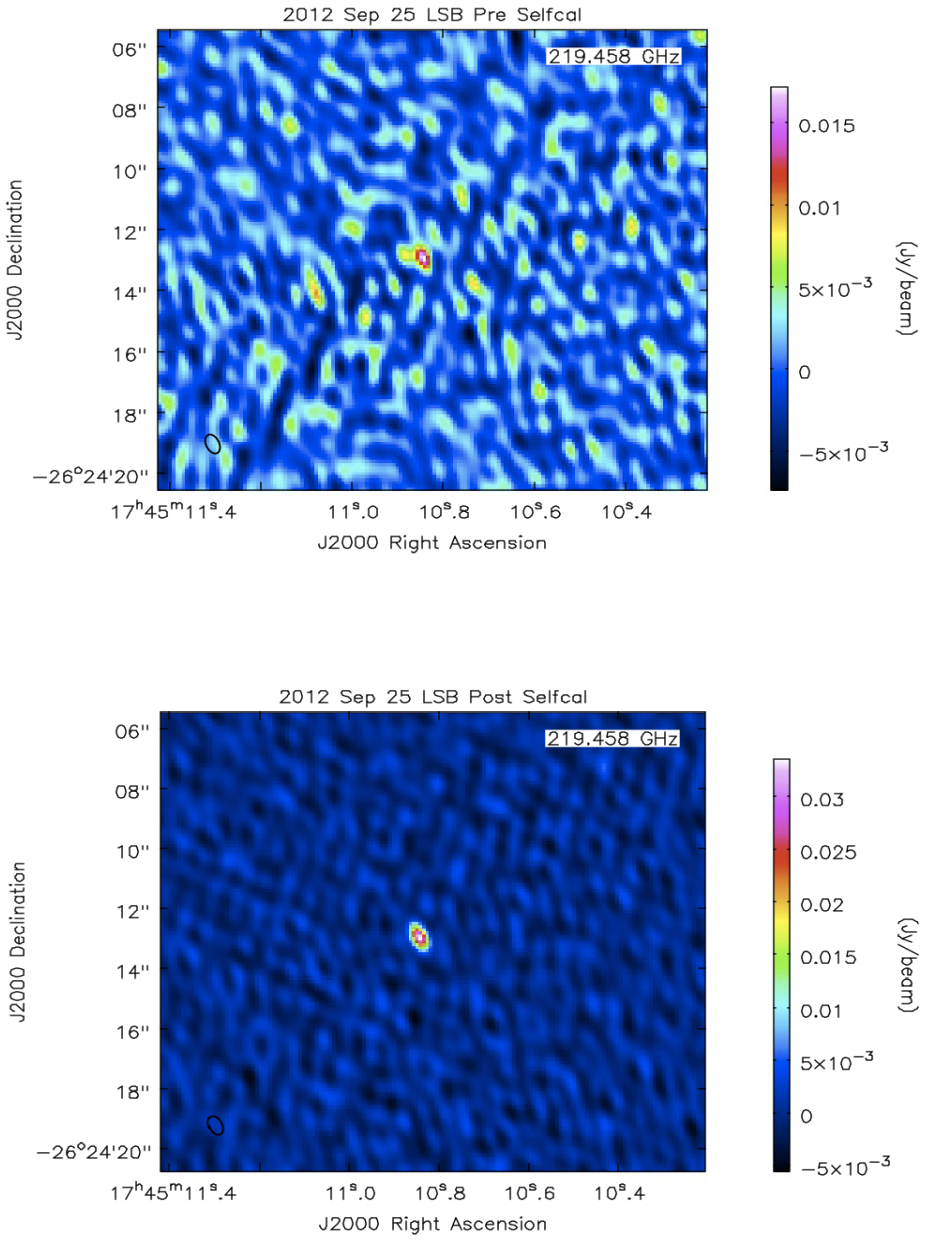

Figure 2.13: Images of Swift J1745–26 on 2012 Sep 25 in the lower sideband (219.445 GHz), both pre (top panel) and post (bottom panel) phase self-calibration. Colours correspond to the intensity scale seen on the right given in units of Jy/beam. The ellipse in the bottom left represents the FWHM of the clean beam. Residual phase calibration errors are evident in the pre self-calibration image. There is clearly a significant increase in S/N post self-calibration, as we have corrected for phase decorrelation that spread source flux throughout the image.

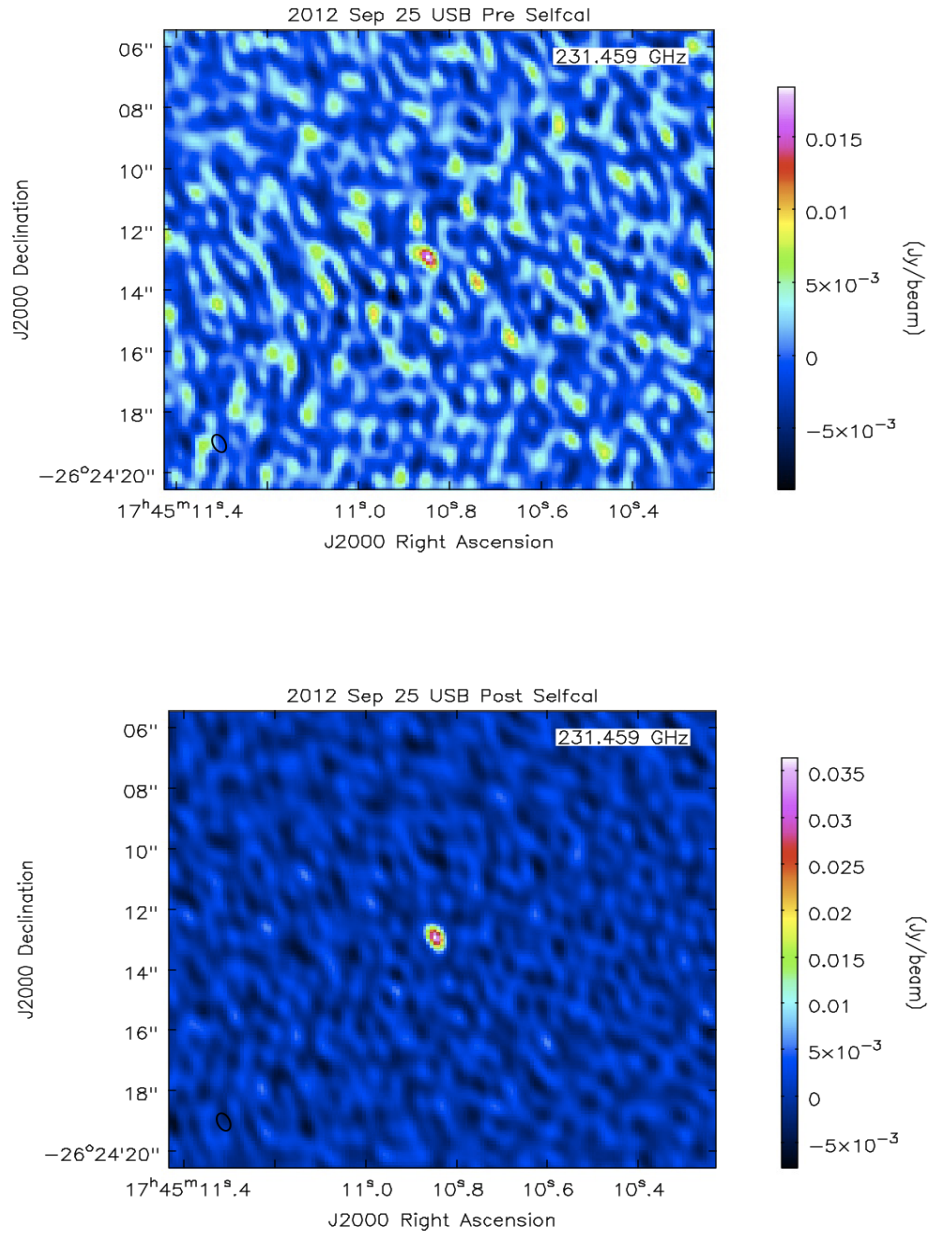

Figure 2.14: Images of Swift J1745–26 on 2012 Sep 25 in the upper sideband (231.445 GHz), both pre (top panel) and post (bottom panel) phase self-calibration. Colours correspond to the intensity scale seen on the right given in units of Jy/beam. The ellipse in the bottom left represents the FWHM of the clean beam. Residual phase calibration errors are evident in the pre self-calibration image. There is clearly a significant increase in S/N post self-calibration, as we have corrected for phase decorrelation that spread source flux throughout the image.

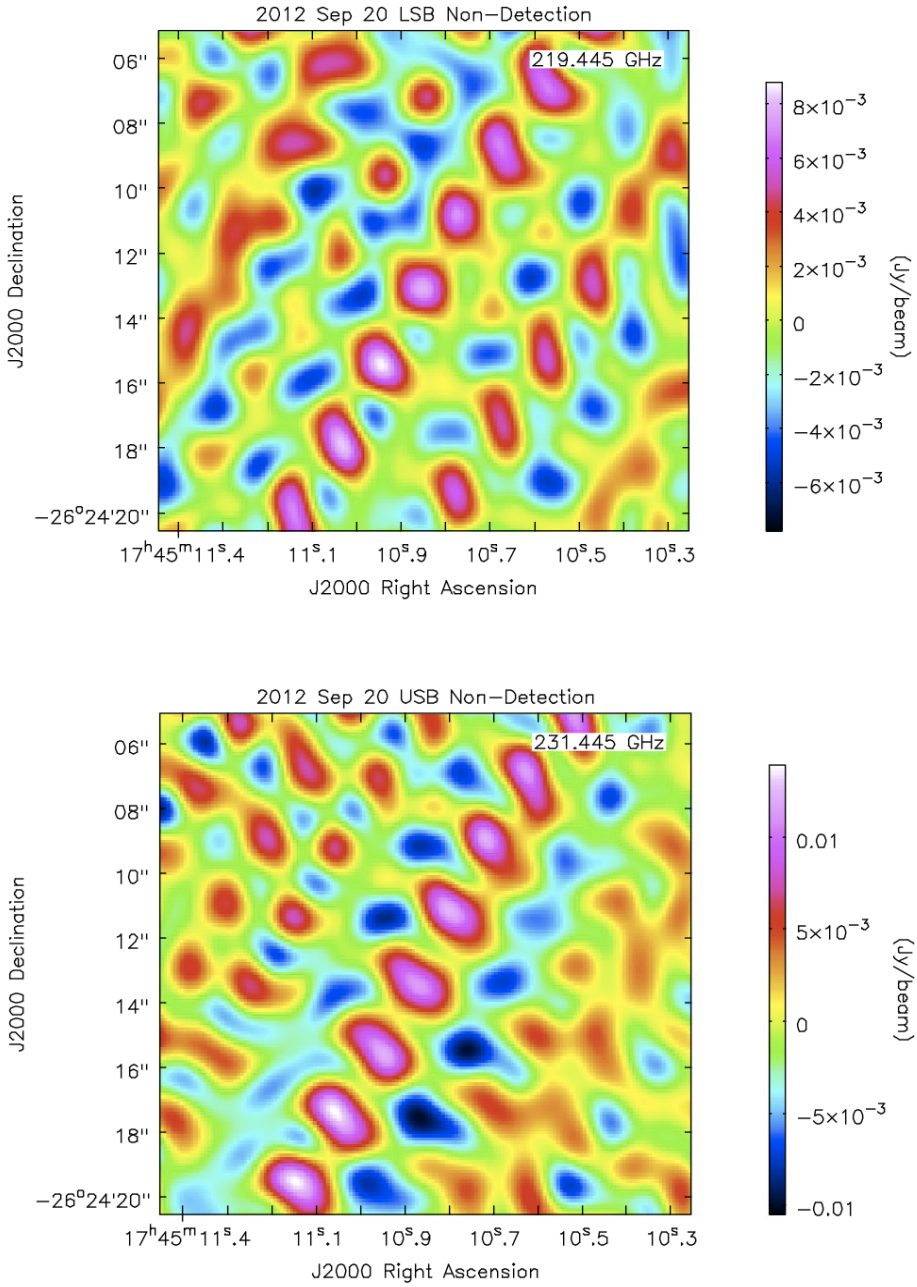

Figure 2.15: Images of Swift J1745–26 on 2012 Sep 20 in the lower sideband (219.445 GHz; top panel) and upper sideband (231.445 GHz; bottom panel). Colours correspond to the intensity scale seen on the right given in units of Jy/beam. The source is clearly not detected in the images. This non-detection is likely a result of the combination of poor quality data and the use of a limited number of antennas during the observations (only 5 antennas creating 10 baselines as opposed to 7 antennas creating 21 baselines in the other two epochs of SMA data).

2.2.2 JCMT

JCMT data was reduced using the Starlink software package, which includes the SMURF, KAPPA, GAIA, and PICARD packages. The observing run with the JCMT is summarized below in Table 2.7, while the calibrators observed in the run are summarized in Table 2.8.

Table 2.7: Observing Run with JCMT

Date	**ν (GHz/μm)**	**Number of Observations**	**Time on Source (hrs)**	**Predicted σ (mJy/beam)**	**PWV (τ)**
2012 Sep 21	352/850	2 (#15, #17)	~ 1.0 (2×30min)	3.0	2mm (0.12)

Table 2.8: Calibrators for JCMT

Telescope	**Date**	**Flux Calibrator**
JCMT	2012 Sep 21	Uranus,CRL2688

The raw SCUBA-2 data consists of two sets of science target observations (Swift J1745-26) as well as two sets of calibrator observations (Uranus and CRL2688[24]). Each observation consists of a number of sub-scans (containing 30 seconds of data each). The first sub-scan is always a noise observation with the shutter closed, the second and last sub-scans are flat-fields (used to convert uncalibrated raw data to units of pW) and the remaining sub-scans are science observations of the target/calibrator (this data is written out 8 times, once for each sub-array in each filter). The data is in the form of a data cube; the first two dimensions denote array dimensions, rows and columns, while the third dimension is a time slice. There are two steps to reduce the data:

1. Run an iterative tool known as the Dynamic Iterative Map Maker (DIMM). This tool down-samples the data to save time and memory, applies the

[24]CRL2688 is a proto-planetary nebula, which consists of a star in the late stages of its evolution between the asymptotic giant branch and the planetary nebula phase. This source is a well known sub-mm source that is compact at 850μm (Dempsey et al., 2012).

flat field solution to calibrate bolometers, cleans data (subtracts a polynomial baseline from each bolometer, removes spikes in data, and fills in gaps in time series data), converts data from uncalibrated form into units of pW, extracts the source signal out of a noise dominated background, and regrids the data to make a map in the sky plane.

2. Calculate a flux conversion factor (FCF) from calibrator observations. This scale factor is used to convert source data from units of pW to Jy.

The DIMM requires a configuration file that instructs the tool on pre-processing steps, the components to iteratively model, and their respective parameters and convergence criteria. The Starlink package provides a default configuration file that needs to be modified to produce optimal results. Table 2.9 outlines the modifications I made to the default parameters. The goal was to produce the flattest map with the lowest noise to achieve the most accurate measurement of source brightness, especially when considering the limited time on source. Modifications were made in accordance with suggestions in Chapin et al. (2013), and parameters from the SMURF package recipe used to reduce bright, compact sources (indicated by a * in Table 2.9).

Table 2.9: DIMM Configuration File Parameters

Parameter	**Default Value**	**My Value**
numiter	-5	-40*
maptol	0.05	0.01*
itermap	0	1
flagfast	1000	500
com.perarray	0	1
noi.box_size	0	-15
850.flt.filt_edge_largescale	300	200*
flt.zero_circle	undef	0.01666° (60 arcsec)*
ast.zero_circle	undef	0.01666° (60 arcsec)*

The DIMM parameter definitions are as follows,

- numiter: this parameter indicates the number of iterations to be performed by DIMM. The negative indicates that this number is an upper limit, the DIMM can finish before this number is reached if the map reaches convergence criteria. I adopt a larger value than the default in accordance with the recipe used to reduce calibrator observations for bright, compact sources.

- maptol: this parameter indicates the value for the normalized change in map pixels. Once again I adopt a value used in the bright, compact source recipe.

- itermap: a value of 1 indicates that the DIMM will make a map every iteration. This is very useful when determining the best value for the numiter and convergence criteria parameters as well as probing changes made in the map by tweaking certain configuration file parameters.

- flagfast: this parameter governs when to flag data if the telescope is moving too fast. I reduced the flagfast parameter from the default as too large a value causes noise to correlate over long length scales and results in smearing out the point source science target in the map.

- com.perarray: this parameter tells DIMM to fit the COM model to each sub-array independently. This is particularly useful if one sub-array is noisier than the other and is a valid choice when you are only mapping one source.

- noi.box_size: this parameter determines the number of time slices used in DIMM to access the noise level in a bolometer time-stream. The default 0 indicates that the whole time stream is used and one variance value is calculated for each bolometer. A non-zero value indicates the time stream is divided into boxes with the specified number of time slices contained

in it, each of which can have an individual variance. This can flatten out the map and reduce smearing within it.

- 850.flt.filt_edge_largescale: this parameters applies a frequency filter when solving for the FLT model. The value given is in arcsec from which the map maker converts to frequency[25]. The value of this parameter is adopted from the bright, compact recipe as it is valid to use harsher filtering when dealing with the tight boundaries of a point source.

- flt.zero_circle: this parameter masks data to exclude the source when solving for the FLT model. Setting this parameter speeds up convergence and reduces noise & negative bowls around sources in the final map. This parameter is adopted from the bright, compact recipe.

- ast.zero_circle: this parameter defines a circle where everything outside the circle is set to zero in solving for the AST model. Using this parameter is a valid choice as we are dealing with an isolated source. This parameter is adopted from the bright, compact recipe.

I produced a map for the two observations of the science target. To convert the map from pW to units of Jy, I calculated an FCF scale factor and applied it to the data. While FCF factors are published online, a precise FCF value will depend on the time of the observation. Thus it is beneficial to calculate your own using calibrator observations. To calculate the FCF, I used the following process:

1. Determine the calibrator closest to the science target (i.e., CRL2688);

2. Reduce the calibrator observations with the DIMM using the compact, bright source recipe;

[25] $\max \text{spatial scale} = \frac{\text{slew speed (”/sec)}}{\text{freq.cut (Hz)}} = \frac{155 \text{ arcsec/s}}{X \text{ Hz}}$

3. Run the PICARD recipe CALC_SCUBA2_FCF, and compare the result to standard values online[26];

4. If FCF values were found to be consistent[27], reduce the calibrator observations with DIMM using the same configuration file used on the science target;

5. Solve for the FCF scale factor using CALC_SCUBA2_FCF; and

6. Apply the FCF using the SMURF task *cmult*.

After applying the FCF, I co-added the maps of the two observations together using the PICARD task MOSAIC_JCMT_IMAGES, and cropped the co-added map using CROP_JCMT_IMAGES task to eliminate the noisy edges (this is a consequence of the telescope moving slowly as it reverses direction paired with reduced integration time). To calculate an rms noise level, I used the KAPPA task *stats*. I used the GAIA image tool to view the final map and the EXTRACTOR task within GAIA to find source flux. The source was clearly detected on 2012 Sep 21 at 850μm, but was not detected at 450μm. I attempted to place an upper limit at 450μm, but the result was not strongly constraining ($\sim$ 250 mJy). The final flux density values of the target source from the individual observations and the co-added observation are seen in Table 2.10 below. The large uncertainty in the flux density measurements is dominated by uncertainty in the FCF. Some variation between the flux density of the two observations is seen, but the two observations are consistent within error (1σ). The target source maps paired with their rms noise maps are seen in Figures 2.16, 2.17, 2.18, 2.19, 2.20 and 2.21.

[26]The FCF calculated with the CRL2688 observation was 5.2% higher than the standard value, which is well within the accepted 10% range.

[27]If the FCF values are inconsistent, it is best that the standard values published online are used.

Table 2.10: Flux Densities for JCMT Data

Date	**Observation**	**Flux Density (mJy)**
2012 Sep 21	15	45.27±7.16
2012 Sep 21	17	37.23±7.12
2012 Sep 21	co-added	39.85±5.04

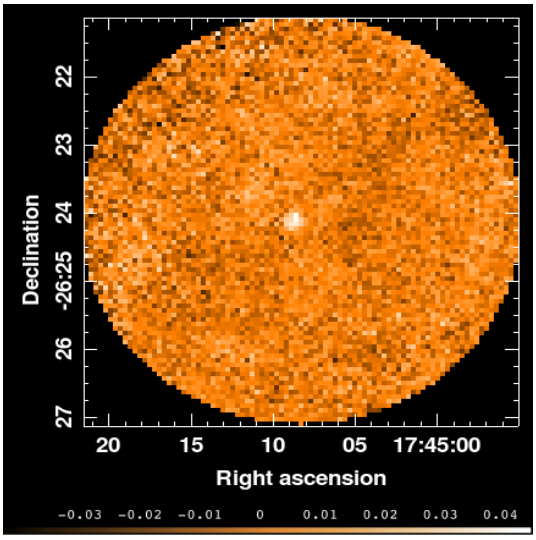

Figure 2.16: Map of Swift J1745–26 on 2012 Sep 21 at 850μm/352.69 GHz produced with observation #15 data. Colours correspond to the intensity scale seen on the bottom given in units of Jy/beam. The source is clearly detected in the image.

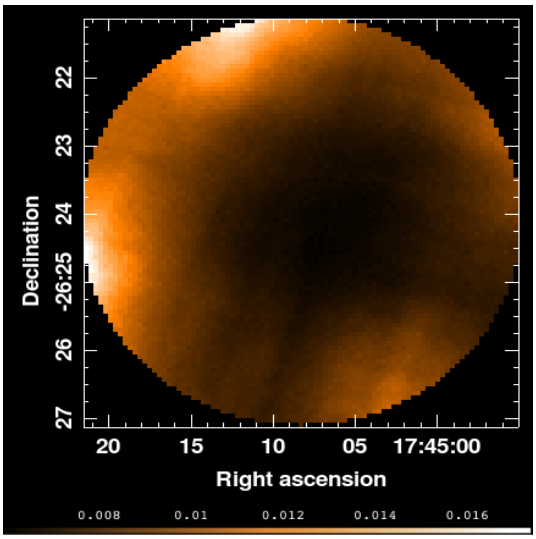

Figure 2.17: RMS noise map of the field of view seen in Figure 2.16. Colours correspond to the intensity scale seen on the bottom given in units of Jy/beam. The rms noise map is fairly uniform, especially in the region where the source is located.

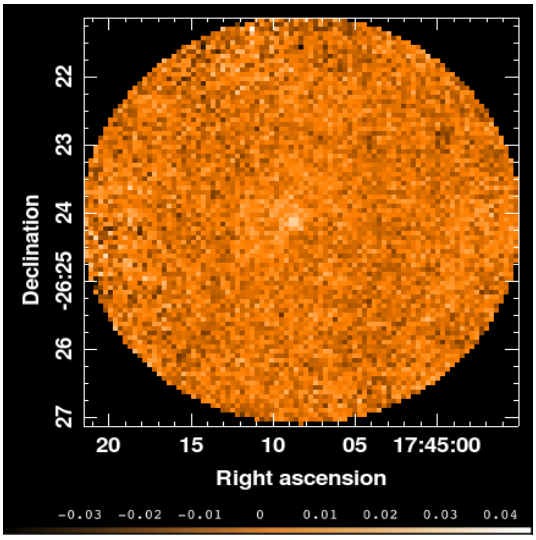

Figure 2.18: Map of Swift J1745–26 on 2012 Sep 21 at 850μm/352.69 GHz produced with observation #17data. Colours correspond to the intensity scale seen on the bottom given in units of Jy/beam. The source is clearly detected in the image.

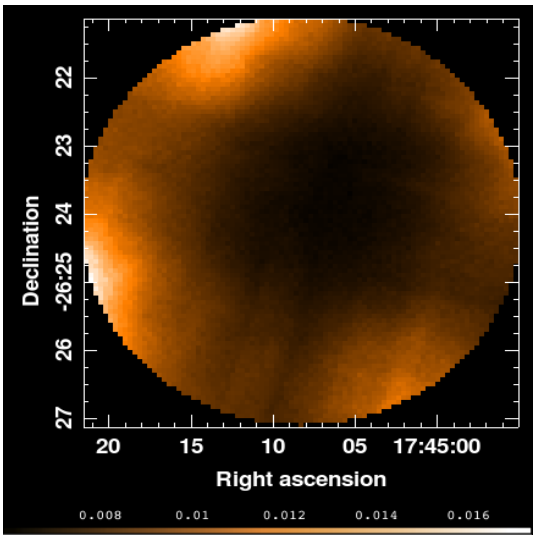

Figure 2.19: RMS noise map of the field of view seen in Figure 2.18. Colours correspond to the intensity scale seen on the bottom given in units of Jy/beam. The rms noise map is fairly uniform, especially in the region where the source is located..

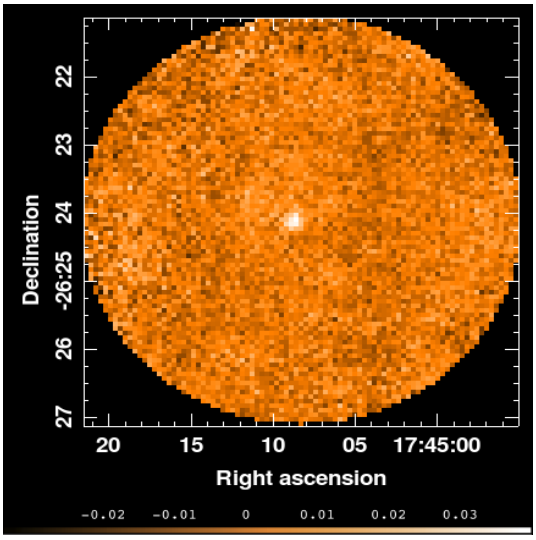

Figure 2.20: Map of Swift J1745–26 on 2012 Sep 21 at 850μm/352.69 GHz produced with the co-added observations. Colours correspond to the intensity scale seen on the bottom given in units of Jy/beam. The source is clearly detected in the image.

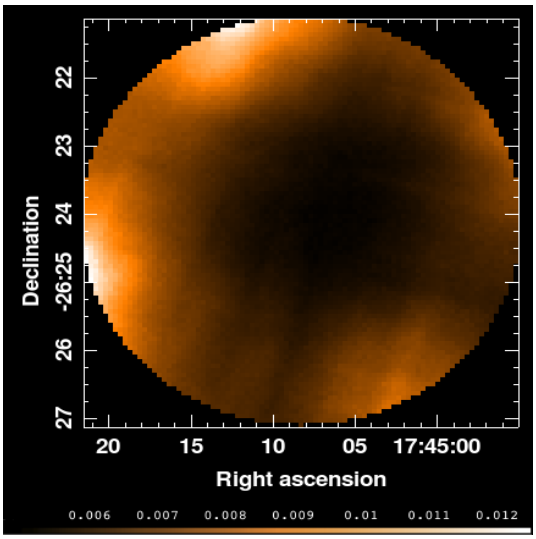

Figure 2.21: RMS noise map of the field of view seen in Figure 2.20. Colours correspond to the intensity scale seen on the bottom given in units of Jy/beam. The rms noise map is fairly uniform, especially in the region where the source is located.

2.2.3 VLA

VLA data were reduced using the CASA package. All observing runs[28] with the VLA are summarized below in Table 2.11[29], while the calibrators[30] used in each run are summarized in Table 2.12. Curran et al. (2014) contains

Table 2.11: Observing Runs with VLA

Date	**Array Config.**	**ν (GHz)**	**$\Delta\nu$ (GHz)**	**Time on Source (min)**	**Predicted rms (mJy/beam)**
2012 Sep 20	A	5.0,7.5	1.024	~ 12	0.18,0.18
2012 Sep 23	A	5.0,7.5, 20.8,25.9	1.024	~ 5	0.26,0.28 0.80,0.82
2012 Sep 25	A	5,7.5 20.8,25.9	1.024	~ 6	0.27,0.27, 0.86,0.88
2012 Sep 26	A	1.5,31.5, 37.5,41.5, 47.5	1.024	~ 10	0.94,1.11, 2.03,2.19

Table 2.12: Calibrators for VLA

Telescope	**Date**	**Flux Calibrator**	**Bandpass Calibrator**	**Gain Calibrator**
VLA	2012 Sep 20	3c286	3c286	J1751–2524
VLA	2012 Sep 23	3c286	3c286	J1751–2524,J1744–3116, J1745–2100
VLA	2012 Sep 25	3c286	3c286	J1751–2524,J1744–3116, J1745–2100
VLA	2012 Sep 26	3c286	3c286	J1751–2524,J1745–2100

more details on the VLA data and the original reduction process. However, during the analysis of the data I noticed several inconsistencies in the data that suggested the presence of errors in the reduction process. As such, James

[28]There was a total of 16 epochs of VLA data taken for this source (Curran et al., 2014), but only the observing runs for the four epochs used in this thesis are shown.

[29]Integration times for all observations were 3 sec.

[30]The calibrators, 3c286, J1751–2524, J1744–3116, and J1745–2100 are all quasars.

Miller-Jones and Peter Curran re-reduced the data after identifying the source of the inconsistencies. Below I outline these problems and explain how they were corrected to yield the final corrected flux density values of the target source used in this thesis (seen in Table 2.13[31]).

While acquiring the data in the C bands (5–7.5 GHz), the array was being moved from the A configuration to the B configuration. The data were reduced immediately after acquisition to rapidly determine how the source was behaving and to guide further observations of the outburst. As a result, the correct antenna positions had not yet been determined. Since we were observing at cm wavelengths, small offsets in position can make a large difference during reduction. In fact, this antenna offset caused flux densities at 7.5 GHz to show a systematically lower flux densities when compared to 5 GHz measurements across all epochs. The reduction was redone with correct positions and the flux density measurements were corrected to those seen in Table 2.13.

Unfortunately, the weather conditions on 2012 Sep 25/26 were very poor; rms phase of 10 degrees, 8m/s wind, and 60% cumuliform cloud cover[32]. The VLA's observing preparation tool indicates that this wind speed is not suitable for observations above Ku band (18 GHz) and the rms phase is not suitable for observations above K band (26 GHz). Further, the images made at Ka and Q bands (30–50GHz) suffer from complete phase de-correlation (the source appeared smeared out and the shape needed to be reconstructed with a source model). Thus when trying to self-calibrate we derived phase solutions that are relatively smoothly varying at 32 GHz, but at 37 GHz and above the

[31]Standard procedure with VLA data is to add systematic errors dependent upon frequency band. Errors of 1% (< 10GHz), 3% ($10 - 40$GHz), or 5% (> 40GHz) were added to the data to yield the uncertainty values in Table 2.13.

[32]For comparison purposes the weather conditions during the other two VLA observations are as follows:

- 2012 Sep 20 had rms phase of 4.1 degrees, wind speed of 3.1 m/s and a clear sky;
- 2012 Sep 23 had rms phase of 1.6 degrees, wind speed of 5.7 m/s and 20 % cumuliform cloud cover.

solutions look like pure noise. Therefore, we conclude that we cannot fully trust any of the measurements from frequencies above 32 GHz (indicated by a * in Table 2.13).

Additionally, following the initial reduction of data in L band (1–2 GHz), we noticed a significant amount of scatter across the band when examining flux density measurements on a per spectral window basis rather than per band basis. After further analysis, we realized that there were a couple of other bright sources in the field whose sidelobes[33] were not de-convolved in the original imaging run as the sources were out of the immediate field of view in the images. However, these sources are bright enough that their un-deconvolved sidelobes spread at least as far as the target source. Since the point spread function varies as a function of frequency, then this could be responsible for some of the scatter that we saw in the measured L band flux densities. The reduction of this L band data was redone with a wider field of view to remedy this issue, and while the quality of the data was improved, scatter is still apparent. This is likely due to radio frequency interference (RFI), a common problem at these low frequencies. The values indicated by a ˆ were chosen as the best compromise of the two frequencies in this band.

[33]In a real interferometer, the wavefront coming from the source can be off-axis, meaning that the path length to the focus can differ across the antenna, which in turn causes a phase differential. When this phase differential is $\sim 1.5, 2.5...$ wavelengths, diffraction causes another maximum in the total received power. These additional maxima are known as sidelobes in the antenna response, where each successive maximum is weaker than the last. As a result, all of the received power from the source does not go into the main beam, rather some goes into sidelobes.

Table 2.13: Flux Densities for VLA Data

Date	**Frequency (GHz)**	**Flux Density (mJy)**
2012 Sep 20	5.0	17.72±0.25
2012 Sep 20	7.5	17.97±0.22
2012 Sep 23	5.0	25.83±0.35
2012 Sep 23	7.5	26.19±0.36
2012 Sep 23	20.8	26.78±1.68
2012 Sep 23	25.9	26.73±1.67
2012 Sep 25	5.0	25.82±0.35
2012 Sep 25	7.5	25.26±0.41
2012 Sep 25	20.8	28.35±1.11
2012 Sep 25	25.9	27.9±1.11
2012 Sep 26	1.4	21.83±0.62ˆ
2012 Sep 26	1.8	23.58±0.57ˆ
2012 Sep 26	31.5	31.31±1.03
2012 Sep 26	37.5	36.46±1.67*
2012 Sep 26	41.5	38.86±3.33*
2012 Sep 26	47.5	40.98±3.52*

Chapter 3

Analyzing the Jet in Swift J1745–26

To extract information about jet structure and behaviour from our flux density measurements presented in the previous Chapter, we analyze how these measurements behave as a function of both time (light curves) and frequency (SED). In this Chapter, I present this analysis with particular emphasis on identifying and characterizing differences seen between the radio and mm/sub-mm regimes. A discussion and interpretation of the results presented in this Chapter appears in Chapter 4.

3.1 Light Curves and SED

Figure 3.1 shows the radio and mm/sub-mm light curves of Swift J1745–26 throughout a 6-day period during the beginning of the 2012 outburst. I do not show measurements at the radio frequencies 1.5, 31.5, 37.5, 41.5, 47.5 GHz, as data from these bands was only obtained in one epoch (2012 Sep 26).

The source evolved somewhat differently between the radio and mm/sub-mm frequency bands during the epochs for which we have data. At radio frequencies (diamonds) we see a rise in source brightness (also see Figure 3.2),

culminating in a brightness peak on 2012 Sep 26 (actually this represents the peak measured radio brightness seen over the entire outburst of this source; Curran et al. 2014). Whereas, at mm/sub-mm frequencies (stars), the source brightness stays relatively constant over the period for which we have data. Unfortunately, as our spare mm/sub-mm data only spans a short period of the outburst in this source, we are not able to draw any further conclusions on differences in temporal behaviour between the radio and mm/sub-mm regimes. Additional mm/sub-mm data of an outbursting source over a much longer time range is needed to make an accurate comparison.

Figure 3.3 shows the radio through sub-mm SED of Swift J1745–26 through different epochs (indicated by different colours) during its 2012 outburst. All of the radio and mm/sub-mm flux measurements were made within a few days (i.e., near-simultaneous) of each other in an attempt to best constrain the jet spectrum.

Again, note the clear flux variability between epochs at radio frequencies[1]. Additionally, an increasing inversion of the spectrum is seen at higher radio frequencies in the 2012 Sep 26 epoch, where we see a flux increase of ~ 15 mJy between $\sim 30-50$ GHz (transparent green points). This upward trend occurs in only one epoch of our data, suggesting the possibility that this peculiar spectral feature is the result of a transient phenomenon in the jet. However, these flux measurements from the 2012 Sep 26 epoch are not very reliable due to poor weather conditions (see the VLA section in Chapter 2). Therefore, while the upward trend in the highest frequency data from 2012 Sep 26 is intriguing, it is possibly (and perhaps most likely) a creation of the self-calibration process in the presence of unstable atmospheric conditions. We thus must not over-interpret this feature.

The source brightness at mm/sub-mm frequencies remains clearly above

[1]Variability is seen at radio frequencies over the entire outburst of Swift J1745–26, with timescales longer than those seen in X-ray variability (Curran et al., 2014).

all trusted measurements at radio frequencies over the entire span of our data (mm/sub-mm frequency measurements are up to a factor of 2 higher then radio frequency measurements), similar to what is seen in a few other BHXRB sources with mm/sub-mm detections (Fender et al., 2001; Russell et al., 2013b; Van der Horst et al., 2013). Possible reasons for increased brightness at mm/sub-mm frequencies over radio frequencies is explored in the analysis of the SED below and in Chapter 4. Further, this source displayed uncharacteristically high brightness at radio frequencies ($\sim 15 - 30\,\mathrm{mJy}$) when compared to other BHXRB outbursts[2] ($\sim 5 - 10\,\mathrm{mJy}$).

[2]Ideally we would wish to compare luminosities rather then fluxes between different BHXRB sources so that differences in source distance can be taken into account. However, of the three mm/sub-mm detected BHXRB sources only one, XTE J1118+480, has a trusted distance measurement (Gelino et al., 2006).

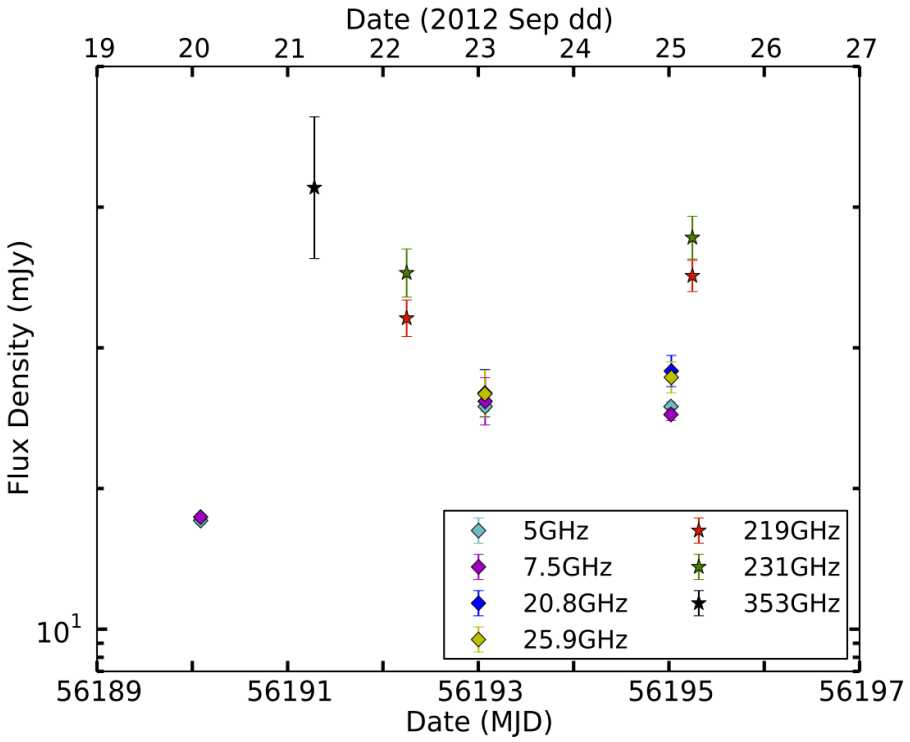

Figure 3.1: Radio (VLA) and mm/sub-mm (SMA/JCMT) light curves of Swift J1745–26 during the hard state of the 2012 outburst. Flux densities in the 1.5, 31.5, 37.5, 41.5, 47.5 GHz bands are not shown, while flux densities at all mm/sub-mm frequencies observed are shown. Measurements made at radio frequencies with the VLA are represented by diamonds and those made at mm/sub-mm frequencies with the SMA/JCMT are represented by stars. Different colours distinguish between measurements at different frequencies, shown in the legend on the bottom right. When error bars are not visible, they are smaller than the symbols.

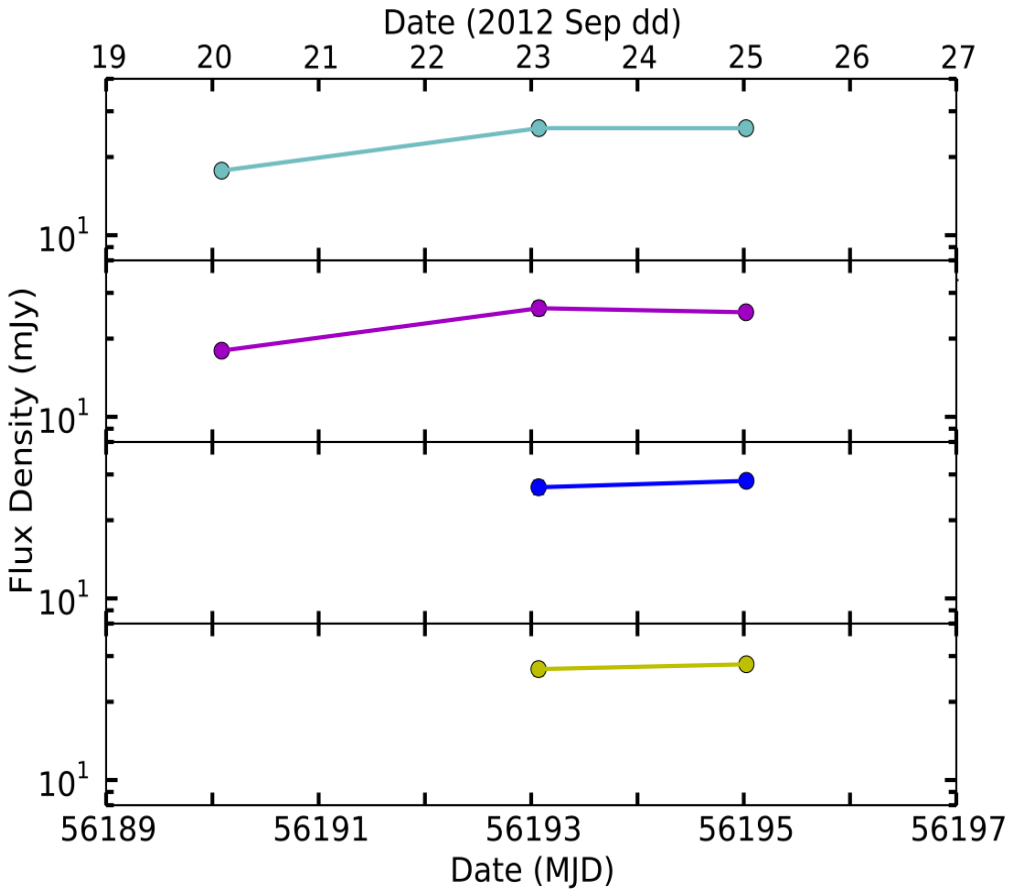

Figure 3.2: Radio (VLA) light curves of Swift J1745–26 during the hard state of the 2012 outburst for frequency bands measured in more than one epoch. The 5 GHz (cyan), 7.5 GHz (magenta), 21.8 GHz (blue), and 25.9 GHz (yellow) frequencies are shown separately to more clearly (compared to Figure 3.1) demonstrate how flux densities evolve in these bands over time. Lines connecting the data points are intended only to guide the eye and are not fits to the data. When error bars are not visible, they are smaller than the symbols.

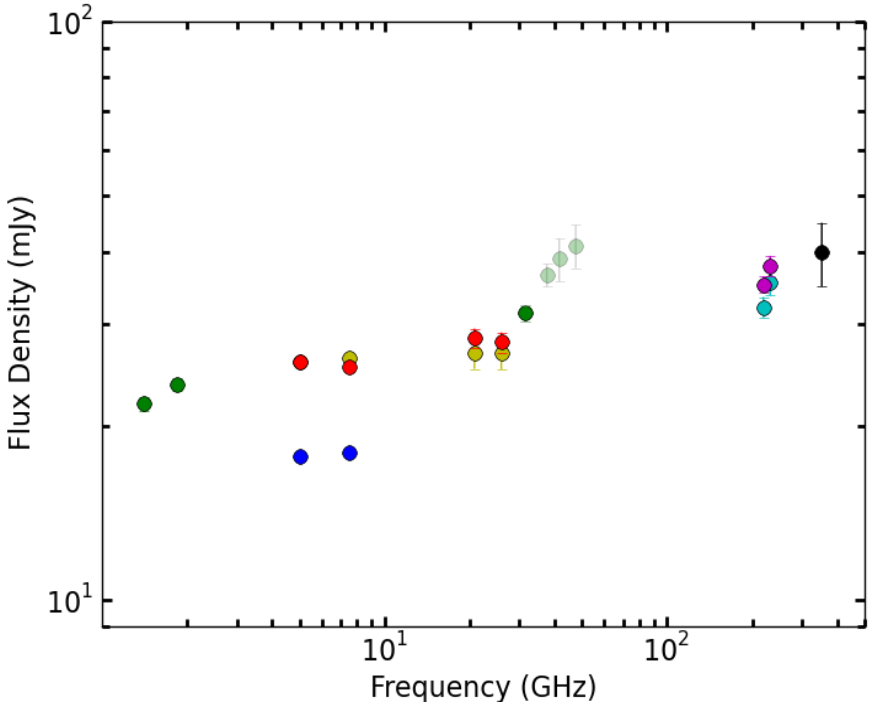

Figure 3.3: Radio through sub-mm SED of Swift J1745–26 during the hard state of the 2012 outburst. Different epochs correspond to different colours, VLA Sep 20 (blue), JCMT Sep 21 (black), SMA Sep 22 (cyan), VLA Sep 23 (yellow), VLA Sep 25 (red), SMA Sep 25 (magenta), and VLA Sep 26 (green). The transparent green points indicate measurements above 32 GHz that are not fully trusted (see the VLA section in Chapter 2). All flux densities shown are on a per frequency band rather than per spectral window basis. Where error bars are not visible, they are smaller than the symbols.

3.2 Spectral Fitting Process

To implement and test standard jet models (i.e., Blandford and Königl's jet spectral model) in the mm/sub-mm regime, we chose to fit a power-law to our SED. This power-law fit was performed using a least squares algorithm[3] implemented in logarithmic space to determine a spectral index (α) and normalization (A) along with their respective uncertainties for each spectral fit.

Linear Space $\rightarrow$ Logarithmic Space

$$f_\nu = A\left(\frac{\nu}{\nu_0}\right)^\alpha \qquad \ln(f_\nu) = \ln(A) + \alpha \ln\left(\frac{\nu}{\nu_0}\right) \tag{3.1}$$

We chose to use $\frac{\nu}{\nu_0}$ in place of simply ν in our fit[4]. If we consider the case where $\nu = \nu_0$, then the normalization parameter (A) we are fitting for represents the normalization at ν_0; $\ln(f_{\nu=\nu_0}) = \ln(A) + \alpha\ln(1) = \ln(A)$. On the other hand, only fitting with ν is equivalent to setting $\nu_0 = 1\,\mathrm{GHz}$, and in turn fitting for the normalization at 1 GHz. Including $\frac{\nu}{\nu_0}$ ensures that the normalization parameter found represents the normalization in the middle of the frequency range we are

[3]We expect the variables in our data set, $(x_i, y_i) = (\nu/\nu_0, f_\nu)$, to follow a linear relationship in logarithmic space. Thus we want to essentially fit a straight line model to our data ($\ln(y_i) = a\ln(x_i) + b$). If we assume our data consists of a sample of observations drawn from a parent distribution which is Gaussian, the probability of obtaining the observed set of measurements can be represented by,

$$P(a,b) = \prod\left(\frac{1}{\sigma_i\sqrt{2\pi}}\right) exp\left(-\frac{1}{2}\sum\left[\frac{y_i - y(x_i)}{\sigma_i}\right]^2\right)$$

The optimum fit to the data will be obtained by finding the maximum likelihood estimates of the values of the parameters, a and b, by maximizing the above probability. As the first factor is a constant, independent of a and b, maximizing the probability is equivalent to minimizing the sum in the exponential (the weighted sum of the squares of the deviations between data and model or chi-squared) (Bevington and Robinson, 2003; Hogg et al., 2010),

$$\chi^2 = \sum\left[\frac{y_i - y}{\sigma_i}\right]^2 = \sum\left[\frac{1}{\sigma_i}(y_i - a - bx_i)\right]^2$$

.

[4]The value ν_0 represents the geometric mean of the collection of input ν measurements.

fitting, as opposed to the normalization (well) outside the frequencies where measurements were made.

The least squares method was implemented using the minimize function in Python's LMFIT package, which uses the Levenberg-Marquardt algorithm as an optimization method. LMFIT extends SCIPY's optimize package capabilities by replacing floating point variables with Parameter objects for the fitted parameters. Parameter objects can be fixed or varied, can have upper and lower bounds, and can be written as an algebraic expression of other parameters, which is much more efficient than changing the objective function to be minimized. In both these packages, the uncertainties[5] in fitted parameters are estimated using the covariance matrix[6], which is not always an accurate way to estimate fitted parameter uncertainties. For instance, in the case where we have transformed the function we are fitting to simplify the least squares process (i.e., transform a power-law into logarithmic space to simply fit a straight line to the data), this can result in improper weighting of the data, which in turn can bias the uncertainties in fitted parameters (Bevington and Robinson, 2003; Hogg et al., 2010).

As such, we performed a Markov-Chain Monte-Carlo (MCMC) method[7] using the EMCEE Python package to check the uncertainties produced from the

[5]Note that since we are in logarithmic space we must consider log uncertainties, $\sigma_{\ln A} = \frac{\partial(\ln f_\nu)}{\partial A}\sigma_A = \frac{\sigma_A}{A}$. Therefore, to retrieve the uncertainty in the normalization parameter, σ_A, we must multiply the uncertainty obtained from the fitting process, $\sigma_{\ln A}$, by the fitted normalization parameter, A. The uncertainty in the spectral index, α, remains the same in linear and logarithmic space.

[6]The elements of the covariance matrix consist of variances and covariances of the fitted parameters. See Bevington and Robinson (2003) and Hogg et al. (2010) for details.

[7]MCMC works not only to maximize the objective function (i.e., probability function; equivalent to minimizing χ^2 in LS) to find the optimum fitted parameters, but also to construct the probability distribution around that optimum fit from which uncertainties in fitted parameters can be computed. The objective function used in the MCMC process is the log probability function (Hogg et al., 2010),

$$\ln\left(\frac{1}{\sqrt{2\pi\sigma_i^2}}\exp\left[-\frac{(y_i - ax_i - b)^2}{2\sigma_i^2}\right]\right)$$

covariance matrix. All uncertainties from the covariance matrix and MCMC method were consistent with each other, indicating that in this case improper weighting of the data is minimal and there is little bias in our calculated uncertainties of the fitted parameters.

3.3 Spectral Fitting in the Individual (radio & mm/sub-mm) Regimes

Standard jet models predict that a self-absorbed compact jet would produce emission that follows a single power-law from radio through sub-mm frequencies, and as such we would expect $\alpha_{\rm radio} \sim \alpha_{\rm mm/sub\text{-}mm}$. On the other hand, while this simple jet model has been proven to match observations at radio frequencies in multiple sources, it may not be a good match to the data at higher mm/sub-mm frequencies. If this is the case, we may see differences in spectral behaviour between the radio and mm/sub-mm regimes, i.e., $\alpha_{\rm radio} > \alpha_{\rm mm/sub\text{-}mm}$ or $\alpha_{\rm radio} < \alpha_{\rm mm/sub\text{-}mm}$.

Figure 3.4 and Table 3.1 display the results of fitting a power-law to the individual radio and mm/sub-mm regimes in the different epochs for which we have data.

Table 3.1: Spectral Indices for Individual Epochs During the 2012 Outburst of Swift J1745–26

Frequency Band(s)	**Fig. 3.4 Color Code**	**Data Sets Fitted (2012 Sep dd)**	**Power-Law Spectral Index (α)**	χ^2	**dof**[a]	$P_{\rm null}$[b]
radio	blue	20	0.035 ± 0.048[c]	0	0	1.00
radio	magenta	23	0.025 ± 0.028	0.06	2	0.97
radio	yellow	25	0.050 ± 0.020	4.98	2	0.08
radio	green	26	0.109 ± 0.013	1.68	1	0.19
mm+sub-mm	cyan	22+21	0.470 ± 0.279	1.30	1	0.25

[a]Degrees of freedom
[b]Null hypothesis probability
[c]Note the spectral index calculated with 2012 Sep 20 radio data has a higher level of uncertainty than the other indices as it is calculated across only 2 bands (using only two flux density/frequency measurements)

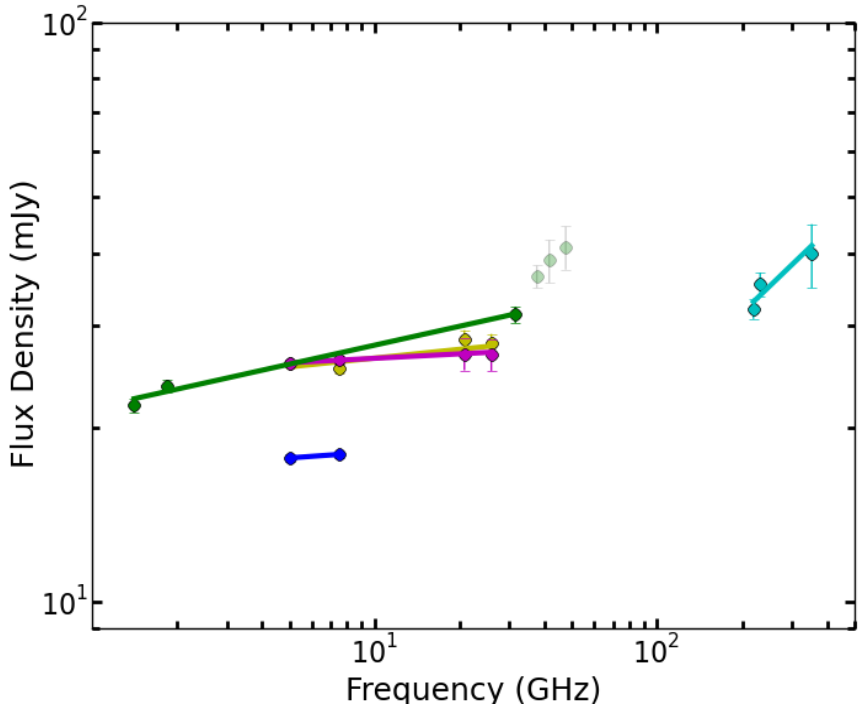

Figure 3.4: Radio and mm/sub-mm SEDs for various epochs during the hard state of the 2012 outburst of the BHXRB Swift J1745–26. Different colours indicate different epochs. The solid lines indicate the power-law fits to the data. Blue represents radio data from the VLA obtained on Sep 20, magenta represents radio data from the VLA obtained on Sep 23, yellow represents radio data from the VLA obtained on Sep 25, green represents radio data from the VLA obtained on Sep 26, and cyan represents mm/sub-mm data obtained from the SMA, on Sep 22 & the JCMT on Sep 21. The faded green points represent the data on 2012 Sep 26 from the VLA which is not fully trusted, and thus not included in the fit. This data is included in the SED for comparison purposes. Where error bars are not visible, they are smaller than the symbols. All spectral indices complete with uncertainties are present in Table 3.1.

Both the radio and mm/sub-mm regimes are fit reasonably well with a single power-law. It is important to note that on 2012 Sep 25/26 we see some deviations (up to the $\sim 2\sigma$ level) from the single power-law at lower frequencies and in turn poorer quality fits when compared to other epochs. However, the observing conditions were less than ideal during these observations, and it is reasonable to assume these deviations are likely the result of such conditions degrading the data quality and making accurate calibration difficult.

In all of the epochs of radio data we see a relatively flat spectral index as expected from a simple self-absorbed jet. If we consider the data points at higher frequencies that contribute to the increasing inversion of the spectrum on 2012 Sep 26 (transparent green points), then this epoch is not well represented by a near flat power-law. However, once again we can not put too much weight on these less trustworthy data points.

In the mm/sub-mm regime, we see a more inverted spectrum compared to that of the radio data in all epochs, albeit this is only a 1.5σ result. The high level of uncertainty in this index is mainly due to the poorly constrained 350 GHz data point, in which limited time on source ($\sim$ 1 hr) led to weak limits on flux. As a result, all spectral indices (radio and mm/sub-mm in all epochs) are consistent with each other at the 3σ confidence level, given the large error bars on the highest frequency measurement.

Given that the uncertainty in our measured mm/sub-mm index is dominated by a poorly constrained flux measurement at 350 GHz, we can estimate the precision we would be able to achieve in our mm/sub-mm index given a 350 GHz measurement with the same rms noise level as our SMA 230 GHz measurements (i.e., $\sim 1.5\,\mathrm{mJy}$). The JCMT SCUBA-2 sensitivity calculator estimates that in order to reach a rms noise level of $\sim 1.5\,\mathrm{mJy}$ we must observe the target source for $\sim$ 5 hrs, which is a reasonable amount of time to request for an observation. To estimate the precision we performed extensive simulations in which we assumed the mm/sub-mm flux is given by the radio

to mm/sub-mm spectral index[8] ($f_{\rm mm} = f_{\rm 6GHz} \left(\frac{\nu_{\rm mm}}{\rm 6GHz}\right)^{\alpha}$, where $\alpha = \alpha_{6-350\,\rm GHz}$), the radio flux at the time of our observations is $f_{6\,\rm GHz} \sim 20\,$mJy (according to our actual VLA measurements), and observations in all mm/sub-mm bands are made with 1.5 mJy rms noise. Figure 3.5 displays this result, with the radio through mm/sub-mm index, $\alpha_{6-350\,\rm GHz}$, on the horizontal axis and the uncertainty in the measured mm/sub-mm index, $\delta\alpha_{219-350\,\rm GHz}$, on the vertical axis. For a radio through sub-mm spectral index similar to our global fits ($\alpha_{6-350\,\rm GHz} \sim 0.1 - 0.2$), we would measure $\alpha_{219-350\,\rm GHz}$ to precisions of < 0.10 (a significant improvement from the ~ 0.30 in our original measurements). With this level of precision, our measurement of a more inverted mm/sub-mm spectrum would become a much more significant ($> 3\sigma$) result, if there was no change in the JCMT flux. Note that with larger $\alpha_{6-350\,\rm GHz}$ we are able to achieve a much higher precision measurement on $\alpha_{219-350\,\rm GHz}$ regardless of rms noise level simply because this more inverted global index corresponds to much higher mm/sub-mm fluxes.

[8] We follow this assumption in our simulations as it corresponds to the procedure we use to trigger mm/sub-mm observations. This triggering procedure is predicated on how the source behaves at radio frequencies and requires that the source reach a specified brightness level in the radio. This threshold brightness level, assuming a typical radio through mm/sub-mm spectral index and a predicted rms noise for current instrumental and observing conditions, gives sufficient S/N in our mm/sub-mm measurements to achieve our science goals.

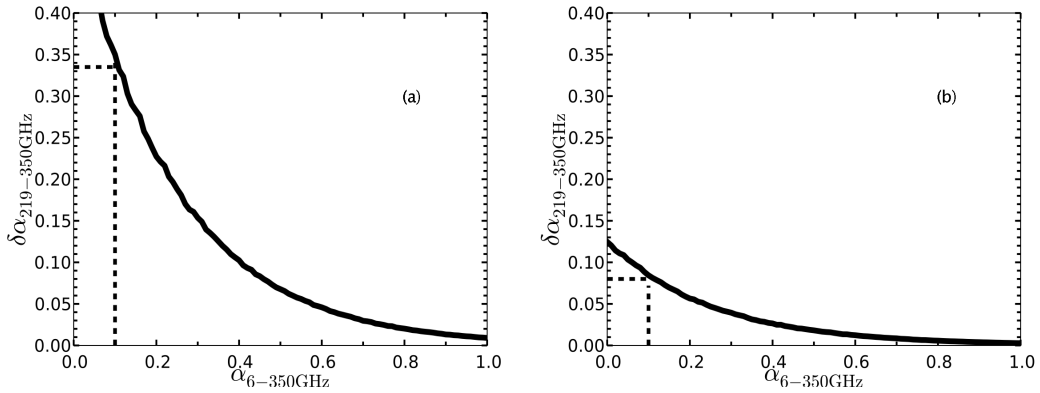

Figure 3.5: . This plot displays an estimate of the precision of the mm/sub-mm spectral index that we can achieve with a specified rms noise level. (a) The simulations were performed with an rms noise at 350 GHz of $\sim 5\,\mathrm{mJy}$ from our observations. (b) The simulations were performed with an rms noise at 350 GHz comparable to those achieved at 230 GHz with the SMA of $\sim 1.5\,\mathrm{mJy}$. The precision with which we can measure the mm/sub-mm spectral index is very sensitive to the rms noise of our flux measurements.

3.4 Spectral Fitting in the Global (radio through sub-mm) Regime

Following the spectral fitting in the individual radio and mm/sub-mm regimes, we fit to the global (radio through sub-mm) regime. Here a constant slope power-law extending from radio through sub-mm frequencies was fit to the SED for different epochs. Figure 3.6 and Table 3.2 display the results of these fits.

Table 3.2: Spectral Indices for Global Epochs During the 2012 Outburst of Swift J1745–26

Frequency Band(s)	**Fig. Panel**	**Data Sets Fitted (2012 Sep dd)**	**Power-Law Spectral Index (α)**	χ^2	**dof**[a]	$P_{\rm null}$[b]
radio+mm+sub-mm	3.6(a)	20+22+21	0.172 ± 0.009	11.56	3	0.01
radio+mm+sub-mm	3.6(b)	23+22+21	0.068 ± 0.008	6.06	5	0.30
radio+mm	3.6(c)	23+25	0.088 ± 0.007	7.39	4	0.12
radio+mm	3.6(d)	25+25	0.090 ± 0.007	11.37	4	0.02
radio+mm	3.6(e)	26+25	0.095 ± 0.007	4.97	3	0.17
radio+mm	3.6(f)	25/26+25	0.092 ± 0.006	15.57	7	0.03
radio+mm+sub-mm	3.7	interp. to 22	0.101 ± 0.009	3.14	2	0.21

[a]Degrees of freedom
[b]Null hypothesis probability

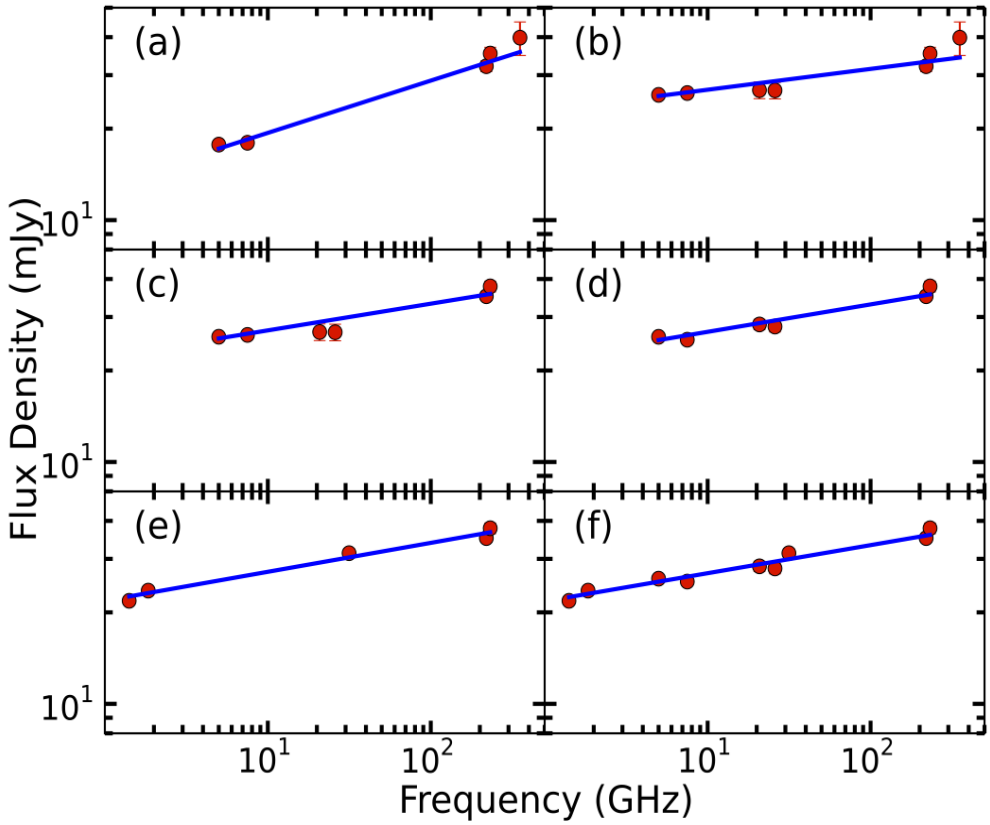

Figure 3.6: Radio through sub-mm SEDs for various epochs during the hard state of the 2012 outburst of Swift J1745–26. Different panels indicate different epochs, (a) radio data from VLA, Sep 20; mm data from SMA, Sep 22; sub-mm data from JCMT, Sep 21, (b) radio data from VLA, Sep 23; mm data from SMA, Sep 22; sub-mm data from JCMT, Sep 21, (c) radio data from VLA, Sep 23; mm data from SMA, Sep 25, (d) radio data from VLA, Sep 25; mm data from SMA, Sep 25 (e) radio data from VLA, Sep 26; mm data from SMA, Sep 25, (f) radio data from VLA, Sep 25/26; mm data from SMA, Sep 25 . The solid blue lines indicate the power-law fits to the data. Where error bars are not visible, they are smaller than the symbols. All spectral indices complete with uncertainties can be seen in Table 3.2.

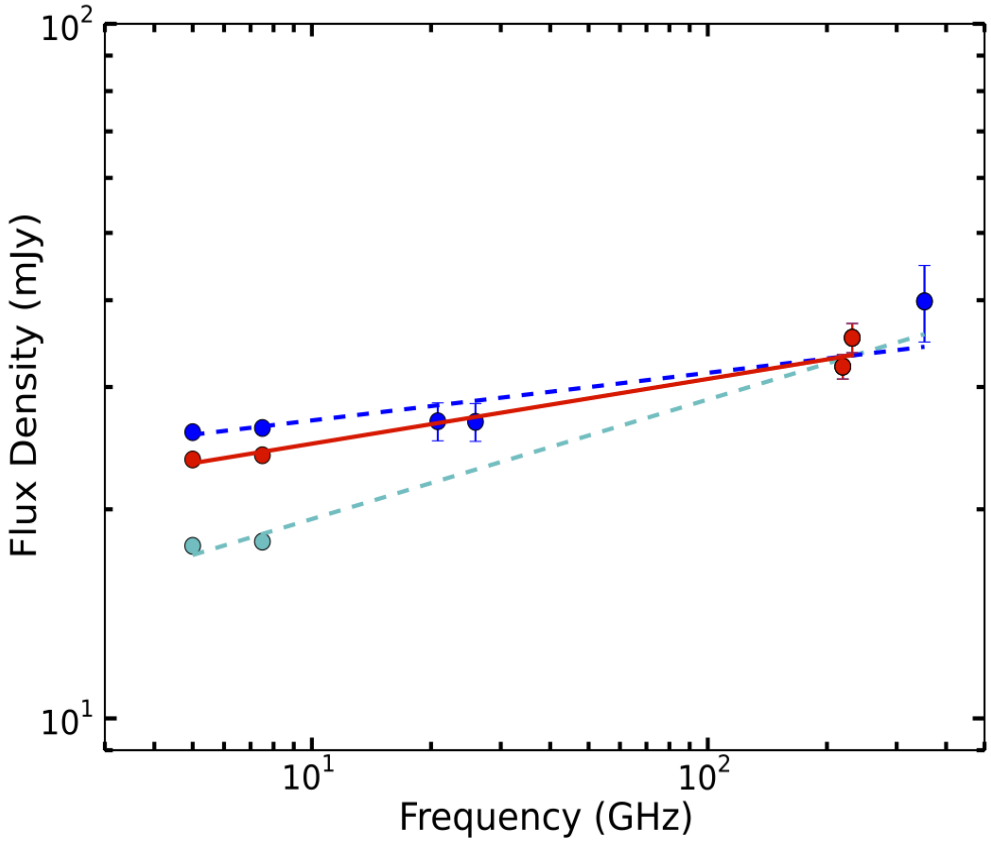

Figure 3.7: Radio through sub-mm SED for various epochs during the hard state of the 2012 outburst of Swift J1745–26. The solid and dashed lines indicate the power-law fits to the spectra. The cyan and blue colours indicate fits to data taken within days of the SMA observation, while the red colour indicates the effect of interpolating the data to the day on which the SMA mm data was taken (Sep 22). Cyan (VLA, Sep 20; SMA, Sep 22; JCMT, Sep 21), blue (VLA, Sep 23; SMA, Sep 22; JCMT, Sep 21). All spectral indices complete with errors can be seen in Table 3.2. Note that when performing the interpolation exact times of the observations in each band are used rather then integer numbers. Where error bars are not visible, they are smaller than the symbols.

It is clear that some epochs are fit better with a power-law than others. In particular, epochs that contain the poorer quality 2012 Sep 25/26 data and those that contain data sets that are separated by up to 2 days tend to show poorer quality fits, indicating that a single power-law is not very well representative of the data in those particular epochs. We believe that these poorer quality fits mainly result from flux variability at radio frequencies occurring between the days on which we have data. For instance, notice that the data sets containing the Sep 20 radio data (Figure 3.6(a)) show a much poorer fit then those containing the Sep 23 radio data (Figure 3.6(b)), even when both data sets are paired with the same mm/sub-mm data. This difference might be the result of the observed flux variability between these two radio epochs.

In an effort to mitigate this effect, we interpolated[9] the radio frequency data to the days on which the SMA mm data was taken (see Fig. 3.7 and Table 3.2). The quality of the fit improves following interpolation. However, some epochs with radio and mm data sets separated by only hours show poorer quality fits then those epochs with radio and mm data separated by days (for instance, consider the data sets fit in Figure 3.6(d) vs. Figure 3.6(c)). As such we opted to take a closer look at the individual radio bands by examining data on a per spectral window basis rather than per band basis.

We fit a power-law within the individual lower frequency radio bands (using

[9]Note that with the data we have it is unclear whether it is correct to interpolate (assume variability) or not (assume constant flux), where these two options likely represent the two extreme positions one could take. In the individual light curves of the radio bands that we are interpolating between (5 and 7.5 GHz; Figure 3.2), source brightness appears to rise rapidly within the time period we are interpolating before plateauing days later. Thus we recognize that the estimate of our interpolated flux in these bands may not be entirely accurate as we do not know exactly how the source is behaving between these days in these bands. Initially we believed that we could obtain some constraints on source behaviour in these bands at the times we are interested in from the L_R/L_X correlation compiled for this source in Curran et al. (2014). However, this source did not display a well defined L_R/L_X relationship. This is most likely due in part to the variability at radio frequencies not corresponding to variability at X-ray frequencies and the source spending more time in intermediate states rather then the HS. Thus we were unable to place any further constraints on the source flux during the time period in question.

per spectral window based data)[10]. While all the bands follow a single power-law quite accurately as expected, surprisingly the indices within the bands do not always match the global power-law indices across the bands (with deviations between $2-3\sigma$). As VLA data is taken sequentially (not simultaneously) in some frequency bands, this result could be suggestive of rapid variability occurring on even shorter timescales, perhaps less than our observational cadence (minutes rather than days). This rapid variability could either be the result of a real physical effect in the jet, or uncertainty in our measurements. There are arguments for both options, and we discuss each possibility further in Chapter 4 below.

Either way, the above analysis demonstrates the need for truly simultaneous data as close together as possible to probe this jet spectral phenomenon accurately and reduce uncertainties introduced through the limit of our instrument capabilities and observing conditions.

[10]In higher frequency radio bands ($> 26\,\mathrm{GHz}$) the fractional bandwidth ($\frac{\Delta\lambda}{\lambda}$) is so narrow that it is not particularly useful to measure flux densities on a per spectral window basis.

Chapter 4

Interpretation of Jet Spectral Behaviour

4.1 Variability & Complex Spectral Features

Through analyzing the jet spectrum above we noticed some unexpected features, most notably significant flux variability (both on timescales of days as well as possibly on much shorter minute timescales) and increasing spectral inversion (both the appearance of an increasingly inverted spectrum at higher radio frequencies in one of the epochs as well as more inverted mm/sub-mm and global indices compared to radio indices). Both of these features can be explained in one of two avenues, either through instrumental uncertainties (calibration, interpolation, systematic errors) or changing physical conditions in the jet. Conclusively distinguishing between the two is difficult with the data we have at this time, but we present the case for each.

It is entirely possible that the flux variability we see in the spectrum is a result of the uncertainty introduced either in calibrating the data, interpolating the data, systematic errors introduced from combining data from different telescopes, or a combination of the three. The complications encountered when reducing this data, notably the confusing bright sources in the field, poor

weather conditions, and changing array configuration during data acquisition all resulted in the need for repeated re-reductions to correct for the presence of scatter within a few individual frequency bands, differing spectral indices between individual bands and global fits, and a pattern of negative slopes between neighbouring bands (between C5 and C7, between K21 and K26). Therefore, it is reasonable to suggest that the presence of unexpected very short timescale variability (less than observational cadence) is the effect of calibration errors introduced from working with less than ideal quality data. In addition, the combination of variability occurring on timescales less than our observational cadence and the fact that the spectral index over the time we have data was only relatively stable, both make accurate interpolation more difficult. Similarly, it is difficult to fully trust the apparent increasing inversion of the spectrum at higher radio frequencies on 2012 Sep 26, when considering the unstable atmospheric conditions and how sensitive and unreliable the use of self-calibration can be in these situations.

While there is a plausible case for the rapid variability we see at radio frequencies being a result of instrumental calibration or interpolation uncertainties, there have been multiple observing campaigns of BHXRBs in which the jet emission displayed a fair bit of intrinsic variability. For instance, rapid variability associated with jet emission that occurs on timescales of $< 1\,\mathrm{sec}$ has been observed at optical and IR frequencies in the BHXRB sources, XTE J1118+480 (Spruit and Kanbach, 2002), Swift J1753.5–0127 (Durant et al., 2008), and GX 339–4 (Gandhi et al., 2008; Casella et al., 2010). Further, in GX 339–4, a high level of variability has been observed at radio through X-ray frequencies (Coriat et al., 2009; Corbel et al., 2000). Detecting such variability in jet emission can provide information about the timescales of physical processes occurring in the jet, jet size scales, and estimates of jet properties such as bulk Lorentz factors and magnetic field strength. In addition, correlating such variability with the well studied X-ray variability, seen during BHXRB

outbursts, could serve as a probe of disc-jet coupling. Further, jet models created by Malzac (2013) and Jamil et al. (2010) suggest a possible mechanism that could produce such rapid variability in the jet. In these models, the jet consists of many discrete shells of plasma that are injected at the base of the jet with variable bulk Lorentz factors[1] and propagate down the jet axis. When a faster moving shell catches up to a slower moving shell a collision occurs. This results in the production of internal shocks within the jet, where a fraction of the bulk kinetic energy of the colliding shells is converted to internal energy that is used to accelerate the particles, in turn producing synchrotron radiation. While these internal shocks work to replenish energy losses of the electrons within the jet (i.e., can produce a flat spectrum), they also naturally produce multi-wavelength variability, which can occur on timescales of minutes at radio frequencies. Such variation is smeared out in longer integrations but could cause the scatter we see here at radio frequencies.

Additionally, there is also work suggesting that adiabatic expansion losses, high magnetic fields ($> 10^5$ G) at the base of the jet or narrow type (i.e., more confined) jet geometry[2] can result in increasing inversion in the jet spectrum (Pe'er and Casella, 2009).

Further, as the increasing inversion seen at higher radio frequencies is only identified in one epoch (2012 Sep 26), this could suggest that the mechanism producing this possible inversion may be a transient phenomena. Conservation of particle number density is one of the main assumptions in Blandford

[1]The energy dissipation profile of these fluctuations and the accompanying jet SED produced are highly dependent on the power spectrum of the fluctuations, $P(f) \propto f^{-\alpha}$. Jamil et al. (2010) inject a white noise power spectrum ($\alpha = 0$), while Malzac (2013) explore a wide range of α. Malzac (2013) find that a "flicker noise" power spectrum ($\alpha = 1$) can produce a flat type SED, while white noise fluctuations can only lead to a more inverted SED. The use of a "flicker noise" type power spectrum is also physically motivated by the fact that the jet is most likely launched from the accretion disc and variability seen in X-ray emission from density fluctuations in the accretion disc displays such a power spectrum. Although, a physical mechanism that can connect density fluctuations in the accretion disc with velocity fluctuations in the jet is still unknown.

[2]Jet geometry is defined in terms of the jet radius (r) as a function of position along the jet axis (x) according to, $r(x) \propto x^{a_{\rm jet}}$. Narrow jets occur when $a_{\rm jet} < \frac{1}{2}$.

and Königl's jet emission model that leads to a flat (rather then more inverted) spectrum, where all synchrotron components (across many orders of magnitude in frequency) peak at the same brightness level. Therefore, one can imagine that a sudden injection of additional material into the jet (violating the conservation assumption) could result in the synchrotron component from the base of the jet displaying a brighter peak flux, and thus appearing to shift upwards in relation to the other components in the SED. The rapid appearance of increasing inversion (like that seen on Sep 26) could be the result of this new brighter component propagating down the jet (i.e., the brighter component shifts towards lower frequencies with time).

4.2 Spectral Indices

The results of our spectral fitting show that the radio spectral indices are all nearly flat ($\alpha \sim 0-0.1$) as expected for a typical self-absorbed synchrotron jet, and similar to what has been seen recently in other BHXRB sources, MAXI J1836–194 ($\alpha \sim 0.2$; Russell et al. 2013b) and MAXI J1659–152 ($\alpha \sim 0-0.2$; Van der Horst et al. 2013). Conversely, the mm/sub-mm index appears more inverted when compared to all the radio indices.

We have to be cautious when taking this result at face value as the highly inverted mm/sub-mm index is poorly constrained due to weaker limits on the flux measurement at 350 GHz. Therefore, while the data does suggest conflicting spectral behaviour between radio and mm/sub-mm regimes, the plausibility of systematic problems with the relative flux measurements (i.e., spectral indices), combined with the fact that all indices are consistent within 3σ, suggests that the discrepancy between regimes could be entirely due to systematic uncertainties. This is further supported by the simulations we performed, which showed that the precision to which we can measure the mm/sub-mm index is degraded in the presence of poorly constrained flux measurements ($\delta\alpha \sim 0.3$

with a ~ 5 mJy rms noise in the 350 GHz point vs. $\delta\alpha \sim 0.07$ with a ~ 1.3 mJy rms noise).

If we treat the more inverted spectral index at mm/sub-mm frequencies as a robust result, it is unclear at this time what could be causing the excess emission at these frequencies, as it is very difficult to definitively test the consistency of such a result in the traditional framework of jet models. However, an increasingly inverted index could contribute to the surprisingly bright fluxes seen in mm/sub-mm detected BHXRBs in outburst. Additionally, there is work that suggests (under the right conditions) the SED can become more inverted in the region leading up to the spectral break (Pe'er and Casella, 2009). Thus there is the distinct possibility that our mm/sub-mm measurements are located close to the break, which is in agreement with standard jet models that predict the spectral break will occur at sub-mm to mid-infared frequencies.

Through examining our global spectral fits, it is evident that a single power-law is reasonably well representative of the data between up to mm/sub-mm frequencies. However, if we compare the indices calculated with only radio measurements to the global indices containing the same radio measurements paired with the mm/sub-mm measurements, the global indices are noticeably more inverted (driven higher by the bright mm/sub-mm measurements). For instance, there is a $\sim 2.5\sigma$ difference between the 2012 Sep 23 radio spectral index (Figure 3.4 magenta) and the radio through sub-mm index from data interpolated to 2012 Sep 22 (Figure 3.7). Therefore, it is clear that radio data alone does not capture the complexities of the full jet spectrum. Further, when comparing absolute fluxes between the radio and mm/sub-mm regimes we find much stronger evidence for spectral inversion driving high mm/sub-mm fluxes in BHXRBs than when we compare relative fluxes (compare radio only and mm/sub-mm only indices).

4.3 High mm/sub-mm Fluxes

The few BHXRBs observed in the mm/sub-mm regime have been surprisingly bright ($f_{350\,\mathrm{GHz}} \sim 40\,\mathrm{mJy}$ for XTE J1118+480, $f_{260\,\mathrm{GHz}} \sim 70\,\mathrm{mJy}$ for MAXI J1836−194, $f_{230\,\mathrm{GHz}} \sim 30\,\mathrm{mJy}$ for Swift J1745−26). Historically, astronomers have been accustomed to finding flat type spectra in jetted sources and it has only been recently that more inverted spectra have been observed in some sources ($\alpha > 0.2$; Russell et al. 2013b). As such, it has been suggested that these high fluxes could in fact be an anomalous spectral feature, as they do not fit in with the standard flat spectral picture. For example, Markoff et al. (2001) found an alternative model-fit (as opposed to Fender et al. 2001 who fit the SED with a simple broken power-law) for the broadband SED obtained from the 2000 outburst of the BHXRB source, XTE J1118+480, where the sub-mm (350GHz) flux is considered anomalous. This JDAF model consists of a relativistic, adiabatically expanding jet that is produced by plasma from a hot ADAF type inner flow. Neglecting the mm/sub-mm data point, the radio through X-ray emission can be almost entirely fit by synchrotron emission. As a result, Markoff et al. (2001) find a flatter radio to IR spectral index then Fender et al. (2001). This in turn results in a significant change in the location of the spectral break (from $\sim 40\,\mu$m to $\sim 1\,\mu$m). As significant changes in the location of the spectral break imply different physical conditions in the jet, understanding whether mm/sub-mm fluxes are anomalously high in BHXRBs is crucial.

With recent evidence suggesting an evolving jet spectral break, we have to be careful when labelling high mm/sub-mm fluxes as anomalous if they are not compared to contemporaneous radio measurements. In XTE J1118+480, the sub-mm measurement was not simultaneous with the radio measurements (Fender et al., 2001), thus it is difficult to determine whether this measurement is in fact anomalous or not. In MAXI J1836–194 (Russell et al., 2013b), the

mm measurement is clearly consistent with the contemporaneous radio measurements, as the radio through mm spectrum is quite accurately represented by a single power-law through multiple epochs.

Similarly, in our global (radio through sub-mm) spectral fits, both the SMA (230GHz) mm and JCMT (350GHz) sub-mm measurements are consistent with contemporaneous radio measurements (with deviations $< 1\sigma$). Therefore, we now have evidence in two sources that challenge the theory that high mm/sub-mm fluxes are anomalous. This evidence further supports our suggestion presented in the last section that the same mechanism driving spectral inversion, albeit inversion for the entire low wavelength spectrum in this case, could be driving high mm/sub-mm fluxes (rather then anomalous excess emission) and justifies the need to continue to sample this mm/sub-mm regime more completely in multiple sources.

We can perform similar simulations to those described in Section 3.1.1 to estimate the precision needed to accurately test anomalous mm/sub-mm fluxes. To do this we can estimate the precision with which we can extrapolate our measured mm/sub-mm normalization and spectral index towards radio frequencies. While this may seem counterintuitive, it represents our ability to recognize deviations from a single power-law spanning across these two regimes in terms of our spectral measurements (i.e., given our measured mm/sub-mm index) and in turn conclusively test for anomalous behaviour[3].

Figure 4.1 displays this result, with the measured mm/sub-mm index, $\alpha_{219-350\,\mathrm{GHz}}$, on the horizontal axis and the uncertainty in the extrapolated radio flux on the vertical axis. For our measured mm/sub-mm index, $\alpha_{219-350\,\mathrm{GHz}} \sim 0.45$, at current rms noise levels we would only be able to recognize a difference between the extrapolated and measured radio flux if the measured flux was $> 30\%$ of the extrapolated radio flux (i.e., $> 30\%$ anomalous flux). While with

[3]Note that one could turn this argument around and estimate the precision with which you could extrapolate measured radio normalization and spectral indices towards mm/sub-mm frequencies as well.

more sensitive mm/sub-mm measurements (i.e. equivalent rms noise of 1.5 mJy in all mm/sub-mm bands) we are able to recognize differences if the measured flux was as small as 8% of the extrapolated radio flux (i.e., 8% anomalous flux). Thus with well constrained mm/sub-mm flux measurements, the uncertainty in the extrapolated radio flux is smaller, we are able to compare this extrapolated radio flux to the measured radio flux at a much higher precision, and in turn be able to recognize even minor anomalous behaviour. Once again note that with larger $\alpha_{219-350\,\mathrm{GHz}}$ we are able to achieve a much higher precision measurement regardless of rms noise level simply because this more inverted index corresponds to much higher mm/sub-mm fluxes.

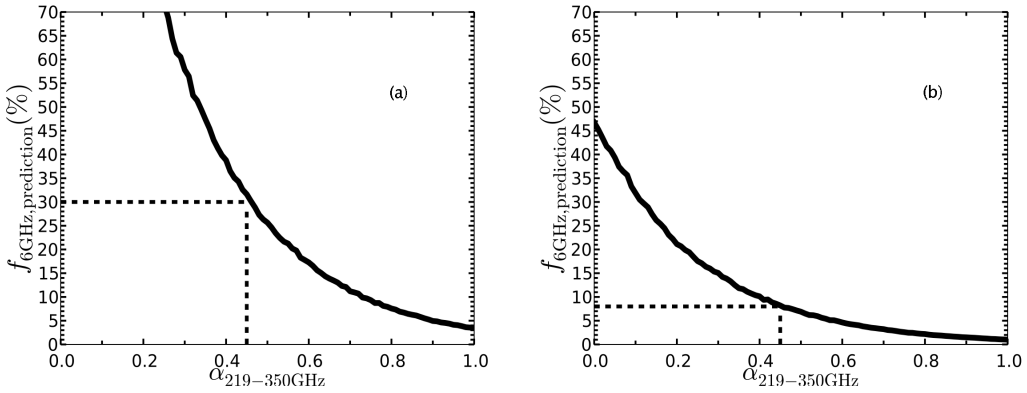

Figure 4.1: This plot displays the precision with which we can extrapolate the mm/sub-mm normalization and spectral index towards radio frequencies and in turn represents our ability to conclusively test whether the mm/sub-mm behaviour of the jet is anomalous. (a) The simulations were performed with an rms noise of at 350 GHz of ~ 5 mJy from our observations. (b) The simulations were performed with an rms noise at 350 GHz comparable to those achieved at 230 GHz with the SMA of ~ 1.5 mJy. Our ability to conclusively test whether the mm/sub-mm behaviour of the jet is anomalous is highly dependent on the rms noise of our flux measurements.

4.4 Validity of Blandford & Königl's Jet Spectral Model at mm/sub-mm Frequencies

Blandford and Königl's spectral model represents the canonical model of emission from compact jets. While this simple model can not completely describe jet behaviour (especially with recent evidence of an evolving SED), its ability to consistently match observations at radio frequencies have made it a standard and still widely used model for interpreting observations from jetted sources. In particular, this model is often used to estimate the location of the spectral break in the jet spectrum. However, in the absence of mm/sub-mm measurements, this process amounts to extrapolating over many orders of magnitude in frequency. Since, the mm/sub-mm regime probes the base of the jet in the region near the BH, where the jet is launched and particle acceleration is expected to occur, it is dangerous to believe an extrapolated spectral model extending through this region without having direct mm/sub-mm measurements. The simultaneous radio and multiple band mm/sub-mm data obtained for this thesis allow us the unique opportunity to test how well this simple power-law model can describe the jet spectrum in the mm/sub-mm regime.

In the previous Sections, we have seen that our data produce somewhat conflicting results on this matter. While a simple power-law seems to reasonably represent the SED up to sub-mm frequencies (350 GHz), a more inverted mm/sub-mm index is potentially indicated by our data and can not be explained with this model. Possible complex spectral features and rapid variability also challenge the use of this simple model. Therefore, while our data presents the intriguing possibility that spectral behaviour in the mm/sub-mm regime can not be fully predicted by this model, the level of uncertainty in our measurements require further observations in multiple sources to confirm such a result.

Nevertheless, even with these uncertainties, our data reveals that the shape

of the jet spectrum (i.e. spectral indices) is highly dependent on mm/sub-mm measurements. Thus, while this model may be able to accurately estimate the spectrum (at least up to sub-mm frequencies), using this model to calculate spectral indices or constrain the location of the break could lead to erroneous results in the absence of mm/sub-mm data.

Chapter 5

Conclusion

5.1 Summary of Results

In this thesis, I have presented the results of our observing campaign of the new transient BHXRB source, Swift J1745–26 during its 2012 outburst at radio and mm/sub-mm frequencies with the VLA, SMA and JCMT. This campaign marked both the first time that simultaneous radio and multiple band mm/sub-mm observations of a BHXRB have been obtained and the first time that the mm/sub-mm spectral index of a BHXRB jet has been measured. The combination of radio and mm/sub-mm measurements allowed us to compare the spectral behaviour between the two regimes and directly probe a part of the jet spectrum that has never been thoroughly sampled before. Through this work we aimed to test whether the jet emission we see was consistent with standard (power-law) jet models, as well as constrain the origin of the large mm/sub-mm fluxes we see in outbursting BHXRBs.

To analyze the jet spectrum in terms of standard jet models we fit a power-law model to the radio, mm/sub-mm, and global ($f_\nu \propto \nu^\alpha$, where α is constant through the regimes) regimes for the different epochs when we had data. The results of this spectral fitting are as follows:

- The mm and sub-mm data are completely consistent with contemporane-

ous radio data (with deviations $< 1\sigma$). This indicates that the mm and sub-mm fluxes are not anomalously high when compared to extrapolations from the radio data. Regardless of their origin, such high mm/sub-mm fluxes bring these BHXRB systems in reach of current mm/sub-mm arrays.

- We found a more inverted spectral index in the mm/sub-mm regime when compared to the radio regime across multiple epochs, but this result is only true at the 1.5σ level. If the mm/sub-mm spectral indices are more inverted than simultaneous radio indices, then the mechanism behind the inversion may have also contributed to the few other high mm/sub-mm fluxes seen in outbursting BHXRBs.

- Global (radio through sub-mm) spectral indices are more inverted than radio only indices (differences up to 2.5σ). Thus, once again our measurements suggest a more inverted spectral index, even if it extends from radio through to sub-mm, could be contributing to the high mm/sub-mm fluxes seen in BHXRBs.

- Extensive simulations indicate that both the precision with which we can measure the mm/sub-mm spectral index and our ability to conclusively test whether the mm/sub-mm behaviour of the jet is anomalous are highly dependent on the rms noise of our flux density measurements. This indicates the need for high quality measurements at mm/sub-mm frequencies.

- Complex spectral features (i.e., increasing inversion of the spectrum) and rapid flux variability challenge the use of standard, canonical jet models such as Blandford & Königl's model, where jet emission before the spectral break can be fitted with a single power-law. However, these deviations from a single power-law could be explained by poor quality data and problematic data calibration.

- Given the day to day variability we measured at radio frequencies, obtaining truly simultaneous multi-wavelength measurements as close together as possible (< 1 day apart) across multiple epochs is necessary to accurately probe the jet spectrum.

While our results contain a relatively high level of uncertainty, they clearly point out the vital importance of the mm/sub-mm regime in understanding the jet spectrum and justify the need to explore this regime further. More high-quality, well-sampled SEDs of BHXRBs in outburst, including the mm/sub-mm regime, will help further constrain the jet spectrum, aid in developing more accurate jet models, and ultimately help understand the underlying physics of relativistic jets in BHXRBs.

5.2 Future Work

This thesis has opened up a new window with which to study BHXRB jets, in the mm/sub-mm regime, and there are many different projects that can be pursued as future work in this field.

To further understand the behaviour of these jets in the mm/sub-mm regime, we require measurements of outbursting BHXRBs in multiple sources. I am currently leading several programs with different instruments to obtain this data. We have continuing programs with the SMA and JCMT, as well as newly accepted programs with the Combined Array for Research in Millimetre-wave Astronomy (CARMA) and the Plateau de Bure Interferometer (PdBI). CARMA and the PdBI provide the advantage of being able to observe in multiple bands with a single instrument. This ability allows us to avoid scheduling conflicts between instruments (an issue we faced in obtaining the data for this thesis), provides a broader wavelength coverage, and eliminates any systematic error introduced in our spectral measurements by combining data from different instruments (another limitation we faced with the data in this thesis). In

addition, CARMA has the ability to respond rapidly to Target of Opportunity (ToO) observations, enabling us to be observing a source in a matter of hours following a trigger of our observation, where this timescale can be on the order of days (SMA) or weeks (ALMA) for other instruments. This is extremely useful when considering the rapid timescales (hrs to days) with which a BHXRB can progress through an outburst. Further, the PdBI offers a very high level of sensitivity (ability to detect faint objects), second only to ALMA. This allows us to observe a larger set of fainter outbursts at a higher signal to noise (PdBI: $> 3\,\mathrm{mJy}$ source at SNR > 20; SMA/CARMA: $> 5\,\mathrm{mJy}$ source at SNR > 5) compared to other instruments.

Through further multi-wavelength monitoring campaigns of BHXRBs (including the mm/sub-mm regime) we will be able to obtain high quality, well sampled SEDs for comparison to more complex jet models.

In this thesis I only analyzed continuum mm/sub-mm data. Considering that BHXRB jets can carry a significant portion of liberated accretion power away from the system, we might expect the jets to stimulate lines prevalent at mm/sub-mm frequencies in the surrounding ISM. As such with the extreme sensitivity of ALMA we would be able to search for such signs of interaction and possibly measure the efficiency with which these jets transport power and energy into the surrounding medium.

Further, in this thesis our spectral measurements suggested the possibility of rapid timescale variability at radio frequencies (discussed in Sections 3.4 & 4.1). With the new capabilities of the recently upgraded VLA, we can search for direct evidence of such rapid variability within data from outbursting BHXRBs using high time resolution analysis.

Observing a BHXRB with a very high resolution instrument, such as a global Very Long Baseline Interferometry (VLBI) network, may allow us to observe structure at the base of the jet, essentially directly resolving the region where the jet spectral break occurs. There is a recent proposal to include

ALMA in the global mm-VLBI network through beam-forming, which takes the entire collecting area of the array and synthesizes it into a very large single aperture. Including ALMA would significantly increase the sensitivity of the mm-VLBI, allowing detection of sources with fluxes on the order of a mJy (rather then hundreds of mJy currently) such as those observed in BHXRB jets. This improved mm-VLBI could probe the region close to the BH (scales of 10^{9-10} m) at a resolution of < 1 mas in BHXRB systems (Tilanus et al., 2014; Fish and et al., 2013).

Bibliography

M.A. Abramowicz and I.V. Igumenshchev. *ApJ*, 554:L53–L54, 2001.

S.A. Balbus. *ARA&A*, 41:555–597, 2003.

S.A. Balbus and J.F. Hawley. *ApJ*, 376:214–233, 1991.

T.M. Belloni. *The Jet Paradigm - From Microquasars to Quasars*, ed. Belloni, T.M., Lecture Notes in Physics 794, Springer, 2009.

P.R. Bevington and D.K. Robinson. *Data Reduction and Error Analysis for the Physical Sciences*, McGraw Hill, New York, 2003.

R.D. Blandford. *MNRAS*, 176:465–481, 1976.

R.D. Blandford and M.C. Begelman. *MNRAS*, 303:L1–L5, 1999.

R.D. Blandford and A. Konigl. *ApJ*, 232:34–38, 1979.

R.D. Blandford and D.G. Payne. *MNRAS*, 199:883–903, 1982.

R.D. Blandford and R.L. Znajek. *MNRAS*, 179:433–456, 1977.

H. Bradt. *Astrophysical Processes- The Physics of Astronomical Phenomena*, Cambridge University Press, 2008.

C. Brogan. *Advanced Calibration Techniques*, NRAO Fourteenth Synthesis Imaging Workshop, 2014.

P. Casella and A. Pe'er. *ApJ*, 703:L63–L66, 2009.

P. Casella, T.J. Maccarone, K. O'Brien, R. P. Fender, D.M. Russell, M. van der Klis, A. Pe'er, D. Maitra, D. Altamirano, T.M. Belloni, G. Kanbach, Klein-Woltm M., E. Mason, P. Soleri, A. Stefanescu, K. Wiersema, and R. Wijnands. *MNRAS*, 404:L21–L25, 2010.

E.L. Chapin, D.S. Berry, A.g. Gibb, T. Jenness, D. Scott, R.P.J. Tilanus, F. Economou, and W.S. Holland. *MNRAS*, 430:2545–2573, 2013.

S. Chaty, G. Dubus, and A. Raichoor. *A&A*, 529:A3, 2011.

B.G. Clark. *A&A*, 89:377–378, 1980.

S. Corbel and R.P. Fender. *ApJ*, 573:L35–L39, 2002.

S. Corbel, R.P. Fender, M. Tzioumis, A.K. amd Nowak, V. McIntyre, P. Durouchoux, and P. Sood. *A&A*, 359:251–268, 2000.

S. Corbel, P. Kaaret, R. K. Jain, C. D. Bailyn, R. P. Fender, J. A. Tomsick, E. Kalemci, V. McIntyre, D. Campbell-Wilson, J. M. Miller, and M. L. McCollough. *ApJ*, 554:43–48, 2001.

S. Corbel, R.P. Fender, A.K. Tzioumis, J.A. Tomsick, J.A. Orosz, J.M. Miller, R. Wijnands, and P. Kaaret. *Science*, 298:196–199, 2002.

S. Corbel, M.A. Nowak, R.P. Fender, T. Tzioumis, and S. Markoff. *A&A*, 400: 1007–1012, 2003.

S. Corbel, R. P. Fender, J. A. Tomsick, A. K. Tzioumis, and S. Tingay. *ApJ*, 617:1272–1283, 2004.

S. Corbel, P. Edwards, T. Tzioumis, M. Coriat, R.P. Fender, and C. Brocksopp. *ATel*, 4410:1, 2012.

S. Corbel, M. Coriat, C. Brocksopp, T. Tzioumis, R.P. Fender, J.A. Tomsick, Buxton M.M., and C.D. Bailyn. *MNRAS*, 428:2500–2515, 2013.

M. Coriat, S. Corbel, Buxton M.M., C.D. Bailyn, J.A. Tomsick, E.G. Kording, and E. Kalemci. *MNRAS*, 400:123–133, 2009.

J.R. Cummings, C. Gronwall, D. Grupe, Krimm H.A., Markwardt C.B., Palmer D.M., B. Sbarufatti, and Stamatikos M. *GCN Circular*, 13774:1, 2012a.

J.R. Cummings, Barthelmy S.D., Baumgartner W.H., Fenimore E.E., Gehrels N., Krimm H.A., Markwardt C.B., Palmer D.M., Sakamoto T., Sato G., Stamatikos M., Tueller J., and Ukwatta T.N. *GCN Circular*, 13775:1, 2012b.

P.A. Curran, M. Coriat, J.C.A. Miller-Jones, R.P. Armstrong, P.G. Edwards, G.R. Sivakoff, P. Woudt, D. Altamirano, T.M. Belloni, S. Corbel, R.P. Fender, E.G. Kording, H.A. Krimm, S. Markoff, S. Migliari, D.M. Russell, J. Stevens, and T. Tzioumis. *MNRAS*, 437:3265–3273, 2014.

J.T. Dempsey, P. Friberg, T. Jeness, R.P.J. Tilanus, H.S. Thomas, W.S. Holland, D. Bintley, D.S. Berry, E.L. Chapin, A. Chrysostomou, G.R. Davis, A.G. Gibb, H. Parsons, and E.I. Robson. *MNRAS*, 430:2534–2544, 2012.

M. Diaz Trigo, J.C.A. Miller-Jones, S. Migliari, J.W. Broderick, and T. Tzioumis. *Nature*, 504:260–262, 2013.

C. Done. *Accretion Processes in Astrophysics (Chapter 6)*, XXI Canary Islands Winter School of Astrophysics ed. Shabhaz, T., Cambridge University Press, 2014.

C. Done, M. Gierllinski, and A. Kubota. *ARA&A*, 15:1–66, 2007.

M. Durant, P. Gandhi, T. Shahbaz, A.P. Fabian, J. Miller, V.S. Dhillon, and T.R. Marsh. *ApJ*, 682:L45–L48, 2008.

A.C. Fabian. *ARA&A*, 50:455–489, 2012.

H. Falcke and P.L. Biermann. *A&A*, 293:665–682, 1995.

H. Falcke and S. Markoff. *A&A*, 362:113–118, 2000.

H. Falcke, E. Kording, and S. Markoff. *A&A*, 414:895–903, 2004.

R.P. Fender. *AIP Conference Proceedings*, 599:101–110, 1999.

R.P. Fender. *Black Holes in Binaries and Galactic Nuclei*, Proceedings of the ESO Workshop ed. Kaper, L., van den heuvel, E.P.J., Woudt, P.A., Springer: 193–199, 2001.

R.P. Fender. *MNRAS*, 322:31–42, 2003.

R.P. Fender. *Compact Stellar X-ray Sources (Chapter 9)*, ed. Lewin W.H.G., van der Klis M., Cambridge Astrophysics Series, No. 39:381–419, 2006.

R.P. Fender. *Accretion Processes in Astrophysics (Chapter 7)*, XXI Canary Islands Winter School of Astrophysics ed. Shabhaz, T., Cambridge University Press, 2014.

R.P. Fender and T.M. Belloni. *ARA&A*, 42:317–364, 2004.

R.P. Fender and T.M. Belloni. *Science*, 337:540–544, 2012.

R.P. Fender and E. Gallo. *High Energy Astrophysical Phenomena (astro-ph.HE)*, 1407.3674, 2014.

R.P. Fender, S.T. Garrington, and D.J. McKay. *MNRAS*, 304:865–876, 1999.

R.P. Fender, R.M. Hjellming, R.P.J. Tilanus, G.G. Pooley, J.R. Deane, R.N. Ogley, and R.E. Spencer. *MNRAS*, 322:L23–L27, 2001.

R.P. Fender, T.M. Belloni, and E. Gallo. *MNRAS*, 355:1105–1118, 2004.

R.P. Fender, J. Homan, and T.M. Belloni. *MNRAS*, 396:1370–1382, 2009.

R.P. Fender, E. Gallo, and D.M. Russell. *MNRAS*, 406:1425–1434, 2010.

V. Fish and et al. *Instramentation and Methods for Astrophysics (arXiv:astro-ph.IM)*, 1309.3519, 2013.

J. Frank, A. King, and D. Raine. *Accretion Power in Astrophysics*, Cambridge University Press, 2002.

E. Gallo, R. P. Fender, and G.G. Pooley. *MNRAS*, 344:60–72, 2003.

E. Gallo, S. Corbel, R.P. Fender, T.J. Maccarone, and A.K Tzioumis. *MNRAS*, 347:L52–L56, 2004.

E. Gallo, R.P. Fender, C.R. Kaiser, D.M. Russell, R. Morganti, T. Oosterloo, and S. Heinz. *Nature*, 436:819–821, 2005.

E. Gallo, J.C.A. Miller-Jones, D.M. Russell, P.G. Jonker, J. Homan, R.M. Plotkin, S. Markoff, B.P. Miller, S. Corbel, and R.P. Fender. *High Energy Astrophysical Phenomena (astro-ph.HE)*, 1408.3130, 2014.

P. Gandhi, K. Makishima, M. Durant, A.C. Fabian, V.S. Dhillon, T.R. Marsh, J.M. Miller, T. Shahbaz, and H.C. Spruit. *MNRAS*, 390:L29–L33, 2008.

P. Gandhi, A.W. Blain, D.M. Russell, P. Casella, J. Malzac, S. Corbel, P. D'Avanzo, F.W. Lewis, S. Markoff, M. Cadolle Bel, P. Goldoni, S. Wachter, D. Khangulyn, and A. Mainzer. *ApJ*, 740:L13–L20, 2011.

D.M. Gelino, S. Balman, U. Kizilouglu, A. Yilmaz, E. Kalemci, and J.A. Tomsick. *ApJ*, 642:438–442, 2006.

M. Georganopoulos and A. P Marscher. *ApJ*, 506:621–636, 1998.

S. Heinz and H.J. Grimm. *ApJ*, 633:384–391, 2005.

S. Heinz and R. Sunyaev. *MNRAS*, 343:L59–L64, 2003.

R.M. Hjellming and K.J. Johnson. *ApJ*, 328:600–609, 1988.

J. Hogbom. *ApJS*, 15:417–426, 1974.

D.W. Hogg, J. Bovy, and D. Lang. *Instramentation and Methods for Astrophysics (arXiv:astro-ph.IM)*, 1008.4686, 2010.

W.S. Holland et al. *MNRAS*, 430:2513–2533, 2013.

J. Homan and T.M. Belloni. *Ap&SS*, 300:107–117, 2005.

S. Ichimaru. *ApJ*, 214:840–855, 1977.

O. Jamil, R.P. Fender, and C.R. Kaiser. *MNRAS*, 401:394–404, 2010.

C.R. Kaiser. *MNRAS*, 367:1083–1094, 2006.

H. Karttunen, P. Kroger, H. Oja, M. Poutanen, and K.J. Donner. *Fundamental Astronomy*, Springer, 2003.

J.P. Lasota. *NewAR*, 45:449–508, 2001.

K.R. Lind and R.D. Blandford. *ApJ*, 295:358–367, 1985.

M.S. Longair. *High Energy Astrophysics, Third Edition*, Cambridge University Press, 2011.

J. Malzac. *The Innermost Regions of Relativistic Jets and Their Magnetic Fields*, EPJ Web of Conferences, Volume 61 ed. J.L. Gómez, 2013.

S. Markoff, H. Falcke, and R.P. Fender. *A&A*, 372:L25–L28, 2001.

S. Markoff, M.A. Nowak, S. Corbel, R.P. Fender, and H. Falcke. *A&A*, 397 (645-658), 2003.

S. Markoff, M.A. Nowak, and J. Wilms. *ApJ*, 635:1203–1216, 2005.

J.E. McClintock and R.M. Remillard. *Compact Stellar X-ray Sources (Chapter 4)*, ed. Lewin W.H.G., van der Klis M., Cambridge Astrophysics Series, No. 39:157–213, 2006.

D.L. Meier. *Ap&SS*, 300:55–65, 2005.

D.L. Meier, S. Koide, and Y. Uchida. *Science*, 291:84–92, 2001.

A. Merloni, S. Heinz, and T. Di Matteo. *MNRAS*, 345:1057–1076, 2003.

M.J. Middleton, J.C.A. Miller-Jones, and R.P. Fender. *MNRAS*, 439:1740–1748, 2014.

J.C.A. Miller-Jones, G.R. Sivakoff, and on behalf of the larger JACPOT XRB collaboration. *ATel*, 4394:1, 2012.

I.F. Mirabel and L.F. Rodriguez. *ARA&A*, 37:409–443, 1999.

I.F. Mirabel, L.F. Rodriguez, B. Cordier, J. Paul, and F. LeBrun. *Nature*, 358: 215–217, 1992.

R. Narayan and J.E. McClintock. *MNRAS*, 419:L69–L73, 2012.

R. Narayan and I. Yi. *ApJ*, 452:710–735, 1995.

A. Pe'er and P. Casella. *ApJ*, 699:1919–1937, 2009.

A. Pe'er and S. Markoff. *ApJ*, 753:177–183, 2012.

P. Polko, D.L. Meier, and S. Markoff. *ApJ*, 723:1343–1350, 2010.

P. Polko, D.L. Meier, and S. Markoff. *MNRAS*, 428:587–593, 2013.

P. Polko, D.L. Meier, and S. Markoff. *MNRAS*, 438:559–570, 2014.

G. Ponti, R.P. Fender, M.C. Begelman, R.J.H. Dunn, J. Neilsen, and M. Coriat. *MNRAS*, 422:11–15, 2012.

F. Rahoui, J.C. Lee, S. Heinz, D.C. Hines, K. Pottschmidt, J. Wilms, and V. Grinberg. *ApJ*, 736:63–77, 2011.

M.J. Rees, E.S. Phinney, M.C. Begelman, and R.D. Blandford. *Nature*, 295: 17–21, 1982.

R.M. Remillard and J.E. McClintock. *ARA&A*, 44:49–92, 2006.

S.P. Reynolds. *ApJ*, 256:13–37, 1982.

K. Rohlfs and T.L. Wilson. *Tools of Radio Astronomy*, Springer, 2000.

S. Rosswog and M. Bruggen. *Introduction to High Energy Astrophysics*, Cambridge University Press, 2007.

D.M. Russell, R.P. Fender, R.I. Hynes, C. Brocksopp, J. Homan, P.G. Jonker, and M.M. Buxton. *MNRAS*, 371:1334–1350, 2006.

D.M. Russell, D. Maitra, R.J.H. Dunn, and S. Markoff. *MNRAS*, 405:1759–1769, 2010.

D.M. Russell, S. Markoff, P. Casella, A.G. Cantrell, R. Chatterjee, R.P. Fender, E. Gallo, P. Gandhi, J. Homan, D. Maitra, J.C.A. Miller-Jones, K. O'Brien, and T. Shahbaz. *MNRAS*, 426:815–832, 2012.

D.M. Russell, E. Gallo, and R.P. Fender. *MNRAS*, 431:405–414, 2013a.

D.M. Russell, T.D. Russell, J.C.A. Miller-Jones, K. O'Brien, R. Soria, G.R. Sivakoff, T. Slaven-Blair, F. Lewis, S. Markoff, J. Homan, D. Altamirano, P.A. Curran, M.P. Rupen, T.M. Belloni, M. Cadolle Bel, P. Casella, S. Corbel, V. Dhawan, R.P. Fender, E. Gallo, P. Gandhi, S. Heinz, E.G. Kording, H.A. Krimm, D. Maitra, S. Migliari, R.A. Remillard, C.L. Sarazin, T. Shahbaz, and V. Tudose. *ApJ*, 768:L35–L41, 2013b.

T.D. Russell, R. Soria, J.C.A. Miller-Jones, P.A. Curran, S. Markoff, D.M. Russell, and G.R. Sivakoff. *MNRAS*, 439:1390–1402, 2014.

G.B. Rybicki and A.P. Lightman. *Radiative Processes in Astrophysics*, Wiley Interscience Publication, 1979.

N.I. Shakura and R.A Sunyaev. *A&A*, 24:337–355, 1973.

S.L. Shapiro, A.P. Lightman, and D.M. Eardly. *ApJ*, 204:187–199, 1976.

B. Sharufatti, J. Kennea, D.N. Burrows, S. Campana, N. Gehrels, C.B. Markwardt, J.R. Cummings, M. Siegel, H.A. Krimm, and F.E. Marshall. *ATel*, 4383:1, 2012.

H. Spruit. *Accretion Processes in Astrophysics (Chapter 1)*, XXI Canary Islands Winter School of Astrophysics ed. Shabhaz, T., Cambridge University Press, 2014.

H.C. Spruit and G. Kanbach. *A&A*, 391:225–233, 2002.

S. Stanimirovic, D.R. Altschuler, P.F. Goldsmith, and C.J. Salter. *Single-Dish Radio Astronomy: Techniques and Applications*, Astronomical Society of the Pacific Conference Series, Volume 278, 2002.

J.F. Steiner, J.E. McClintock, and R. Narayan. *ApJ*, 762:104–114, 2013.

A.M. Stirling, R.E. Spencer, C.J. de la Force, M.A. Garrett, R.P. Fender, and R.N. Ogley. *MNRAS*, 327:1273–1278, 2001.

Y. Tanaka and W.H.G Lewin. *X-ray Binaries (Chapter 3)*, ed. Lewin, W.H.G., van Paradijs, J., van den Heuvel, E.P.J., Cambridge Astrophysics Series, No. 26:126–174, 1995.

G.B. Taylor, C.L. Carilli, and R.A. Perley. *Synthesis Imaging in Radio Astronomy II*, Astronomical Society of the Pacific Conference Series, Volume 180, 1998.

R.P.J. Tilanus, T.P. Krichbaum, J.A. Zenus, A. Baudry, M. Bremer, H. Falcke, G. Giovannini, R. Laing, H.J. van Langevelde, and W. Vlemmings. *Instramentation and Methods for Astrophysics (arXiv:astro-ph.IM)*, 1406.4650, 2014.

J.A. Tomsick, M. Del Santo, and T. Belloni. *ATel*, 4393:1, 2012.

A.J. Van der Horst, P.A. Curran, J.C.A. Miller-Jones, J.D. Linford, J. Gorosabel, D.M. Russell, A. de Ugarte Postigo, A.A. Lundgren, G.B. Taylor, D. Maitra, S. Guziy, T.M. Belloni, C. Kouveliotou, P.G. Jonker, A. Kamble, Z. Paragi, J. Homan, E. Kuulkers, J. Granot, D. Altamirano, Buxton, M.M., A. Castro-Tirado, R.P. Fender, M.A. Garrett, N. Gehrels, D.H. Hartmann, J.A. Kennea, H.A. Krimm, V. Mangano, E. Ramirez-Ruiz, P. Romano, Wijers, R.A.M.J., and Y.J. Wijnands, R. andYang. *MNRAS*, 436:2625–2638, 2013.

I. Vovk, C. Ferrigno, E. Bozzo, S.P. Drave, C. Sanchez, E. Kuulkers, A. Bazzano, M. Del Santo, M. Fiocchi, L. Natalucci, A. Tarana, I. Caballero, D. Goetz, J. Chenevez, P. den Hartog, L. Kuiper, and K. Watanabe. *ATel*, 4381:1, 2012.

I. Yi. *ASP Conference Series Volume 160*, ed. Sellwood, J.A. and Goodman, J.:279–296, 1999.

F. Yuan. *MNRAS*, 324:119–127, 2001.

F. Yuan, S. Markoff, H. Falcke, and P.L. Biermann. *A&A*, 391:139–148, 2002.

A.A. Zdziarski and M. Gierlinski. *Prog. of Theor. Phys. Supp.*, 155:99–119, 2004.